

Ferromagnetic nanostructures by laser manipulation

Citation for published version (APA):

Bosch, R. C. M. (2002). *Ferromagnetic nanostructures by laser manipulation*. [Phd Thesis 1 (Research TU/e / Graduation TU/e), Applied Physics and Science Education]. Technische Universiteit Eindhoven.
<https://doi.org/10.6100/IR552779>

DOI:

[10.6100/IR552779](https://doi.org/10.6100/IR552779)

Document status and date:

Published: 01/01/2002

Document Version:

Publisher's PDF, also known as Version of Record (includes final page, issue and volume numbers)

Please check the document version of this publication:

- A submitted manuscript is the version of the article upon submission and before peer-review. There can be important differences between the submitted version and the official published version of record. People interested in the research are advised to contact the author for the final version of the publication, or visit the DOI to the publisher's website.
- The final author version and the galley proof are versions of the publication after peer review.
- The final published version features the final layout of the paper including the volume, issue and page numbers.

[Link to publication](#)

General rights

Copyright and moral rights for the publications made accessible in the public portal are retained by the authors and/or other copyright owners and it is a condition of accessing publications that users recognise and abide by the legal requirements associated with these rights.

- Users may download and print one copy of any publication from the public portal for the purpose of private study or research.
- You may not further distribute the material or use it for any profit-making activity or commercial gain
- You may freely distribute the URL identifying the publication in the public portal.

If the publication is distributed under the terms of Article 25fa of the Dutch Copyright Act, indicated by the "Taverne" license above, please follow below link for the End User Agreement:

www.tue.nl/taverne

Take down policy

If you believe that this document breaches copyright please contact us at:

openaccess@tue.nl

providing details and we will investigate your claim.

Ferromagnetic Nanostructures by Laser Manipulation

PROEFSCHRIFT

TER VERKRIJGING VAN DE GRAAD VAN DOCTOR AAN
DE TECHNISCHE UNIVERSITEIT EINDHOVEN, OP GEZAG VAN
DE RECTOR MAGNIFICUS, PROF. DR. R.A. VAN SANTEN,
VOOR EEN COMMISSIE AANGEWEEZEN DOOR HET COLLEGE
VOOR PROMOTIES IN HET OPENBAAR TE VERDEDIGEN OP
DONDERDAG 21 MAART 2002 OM 16.00 UUR

DOOR

ROELAND CORNELIS MARIA BOSCH

GEBOREN TE BAARLO

DIT PROEFSCHRIFT IS GOEDGEKEURD
DOOR DE PROMOTOREN:
PROF.DR. K.A.H. VAN LEEUWEN
EN
PROF.DR. H.C.W. BEIJERINCK

Druk: Universiteitsdrukkerij Technische Universiteit Eindhoven
Ontwerp omslag: Astrid van den Hoek

CIP-DATA LIBRARY TECHNISCHE UNIVERSITEIT EINDHOVEN

Bosch, Roeland Cornelis Maria

Ferromagnetic Nanostructures by Laser Manipulation / by

Roeland Cornelis Maria Bosch. -

Eindhoven : Technische Universiteit Eindhoven, 2002 . - Proefschrift.

ISBN 90-386-1929-4

NUGI 812

Trefw.: atomaire bundels / laserkoeling / lithografie / nanotechnologie / deeltjesoptica /
ijzer

Subject headings: atomic beams / laser cooling / lithography / nanotechnology /
particle optics / iron

The image shows a handwritten musical score for the second page of 'Rhapsody in Blue' by George Gershwin. The score is arranged in ten staves. The first two staves are labeled 'J.B.' (Jazz Band). The third staff is labeled 'D' (Drum). The fourth and fifth staves are labeled 'I.B.' (Instruments). The sixth and seventh staves are labeled 'S.B.' (Solo). The eighth and ninth staves are labeled 'P.' (Piano). The score includes various musical notations such as notes, rests, and dynamic markings.

The second page of the score of *Rhapsody in Blue* in Gershwin's hand. J.B. stands for Jazz Band.

aan mijn ouders



The work described in this thesis was carried out at the Physics Department of the Eindhoven University of Technology and was part of the research program of the 'Stichting voor Fundamenteel Onderzoek der Materie' (FOM), which is financially supported by the 'Nederlandse Organisatie voor Wetenschappelijk Onderzoek' (NWO).

Contents

1	Introduction	3
1	Laser focusing	3
2	Limitations of laser focusing	4
3	Improved laser focusing	5
4	Experimental setup for improved laser focusing	6
5	Contents of thesis	7
6	Applications of atom lithography	9
2	Why iron?	13
1	Ferromagnetic elements	13
2	Isotopes	13
3	Atomic properties	14
4	Atomic transitions	15
5	Laser manipulation of Fe	17
3	Supersonic Fe beam source for chromatic aberration-free laser focusing	19
1	Introduction	19
2	Seeded supersonic expansions	20
3	Supersonic Fe beam source	23
4	Experimental setup	24
5	Results	28
6	Conclusions	32
4	UV laser system	35
1	Introduction	35
2	Second harmonic generation	37
3	Hollow cathode discharge cell	43
4	Polarization spectroscopy	45
5	Conclusions	51
5	Laser focusing of Fe atoms	53
1	Introduction	53
2	Laser focusing	55
3	Calculation on focusing	59

4	Numerical results	62
5	Atomic diffraction	71
6	Conclusions	72
6	Laser cooling of an atomic Fe beam	77
1	Introduction	77
2	Theoretical aspects of laser cooling	78
3	Simulations	82
4	Measurements of laser cooling of Fe	89
5	Future prospects	92
6	Conclusions	92
	Summary	95
	Samenvatting	97
	Dankwoord	99
	Curriculum Vitae	101

Chapter 1

Introduction

The process of advanced miniaturization of magnetic materials has led to the discovery of several fascinating physical effects. These novel phenomena, such as Giant Magneto Resistance (GMR) [1], are extremely rapidly being exploited by information technology industries, primarily to sustain the ongoing exponential growth of storage density in magnetic media. For the past three years the growth rate has held steady at a factor of two per year. At present, the storage density of commercial devices has reached 35 Gbit in^{-2} , corresponding to a magnetic bit spacing of 135 nm [2]. If the growth continues at the present rate, magnetic bits with dimensions of a few nanometer are quickly in sight. Viewed in this perspective, the study of nanomagnetic entities is a crucial element in the search for the ultimate fundamental limits involved in magnetic memory technologies. A prominent aspect is the fabrication of magnetic nanoparticles with nanometer control of shape and mutual separation. Efforts to develop a non-traditional technology to achieve this, based on *laser focusing of a beam of neutral iron atoms*, constitute the central subject of this thesis.

1 Laser focusing

Laser focusing is a relatively new area, where successful experiments have been performed with, e.g., chromium atoms [3,4]. Fig. 1.1 shows an AFM image of chromium structures that were deposited with laser focusing. The Cr dots have a typical size of 50 nm and a perfect periodicity of 213 nm (half the laser wavelength). Other experiments are in progress with the deposition of group III metals like indium, gallium and aluminum [6, 7], and with electronically excited rare gas atoms [8–12] used to expose resist layers. Iron is perhaps one of the most difficult elements for this kind of experiment. Nevertheless, it is the ferromagnetic element most suitable for laser focusing.

Figure 1.2(a) shows the basic idea of laser focusing. A beam of atoms is traveling through a strong standing light wave. The strong gradients of the light intensity in the standing wave lead to forces on the individual atoms. The light properties can be chosen such that the atoms are attracted to regions of low intensity, in the same sense that light in a gradient index lens is ‘attracted’ towards the high index region. The areas near the nodes of the standing wave will then act as micro-lenses. Atoms passing through these microlenses will be focused to spots at a certain distance behind the light wave. In this focal plane, a substrate will be placed.

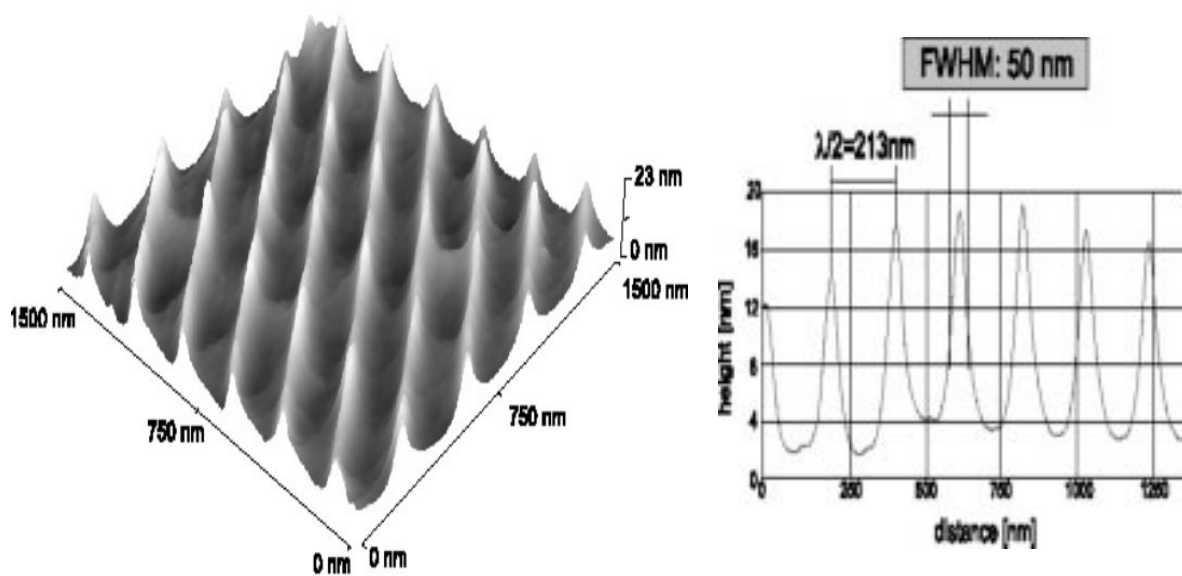


Figure 1.1: AFM image of chromium dots deposited with laser focusing. The structures are 50 nm in size with a perfect periodicity of 213 nm. Courtesy of M. Oberthaler, University of Konstanz.

The increased deposition rate at the focal spots will lead to the growth of a structure with a periodicity that matches that of the standing wave. In this way, an array of very small lines or dots (depending on whether a one- or two-dimensional standing wave is used) can be produced with a perfect periodicity of $\lambda/2 = 186$ nm.

2 Limitations of laser focusing

The conventional way of laser focusing, as illustrated in Fig. 1.2(a), does not lead to separated structures of 10 nm or smaller, which need to be fabricated for the study of fundamental limits of ferromagnetism or 1D and 0D nanomagnetics. The smallest chromium structures that have been produced by now have a width of 29 nm and are deposited on top of a chromium background layer with a thickness of 1/4 of the structure height [13].

The relatively large structure width and the background can be partially explained by chromatic and spherical aberration of the micro-lenses of the standing wave, respectively. Chromatic aberration arises from the fact the atoms in the atomic beam have different axial velocities. In all experiments on laser focusing of metal atoms so far, the atomic beam has been generated by an effusive beam source. The atoms in the resulting beam have a thermal velocity distribution, which means that the velocity spread is comparable to the mean velocity. The focal distance is, however, proportional to the square of the atomic velocity, resulting in the atom optics equivalent of chromatic aberration. The equivalent of spherical aberration occurs because only the regions close to the nodes of the standing wave contribute to the focal spot. Atoms traveling near the anti-nodes will not be focused and contribute to a background which is formed inbetween the structures.

Another important factor for adequate laser focusing is the requirement of a well collimated

beam, meaning that the beam divergence should be as low as possible. In the schematic view illustrated in Fig. 1.2(a) the atomic beam is parallel. However, atomic beams obtained from any beam source are divergent. This leads to a structure broadening on the order of $\varphi \cdot f$ with φ the beam divergence and f the focal distance, which is on the order of $50 \mu\text{m}$. For the production of 10 nm structures the FWHM beam divergence should be less than $200 \mu\text{rad}$. Aperturing the atomic beam to achieve this divergence leads to a dramatic loss of beam flux. Therefore laser cooling is applied to the atomic beam to decrease the beam divergence without excessive loss of beam flux.

There is another factor which is assumed to be responsible for broadening of the structures which have been fabricated so far. In experiments in which Cr atoms are focused, it is believed that because of surface diffusion of Cr atoms on top of the Cr background the structures tend to smear out, resulting in broader structures [13]. In the next chapter this problem will be discussed for our case, in which Fe atoms are focused.

Beam diffraction is the fundamental limit for the final resolution, just as in optical lithography. This limit is approximately the ratio of half the wavelength used to the numerical aperture, which at present results in a limit of around 70 nm . With laser focusing, which is often referred to as *atom lithography*, the same limit holds. However, the wavelength is equal to the deBroglie wavelength of the atom, which is many orders of magnitude smaller than the optical wavelength. For typical conditions in atom lithography experiments, the diffraction limit is only a few nanometer.

3 Improved laser focusing

We will apply two improvements to conventional laser focusing for the reduction of chromatic and spherical aberration:

- the atomic Fe beam is generated by a *supersonic beam source*.
- an additional mechanical grating is placed just upstream of the standing wave.

In a supersonic Fe beam the axial velocity spread of the atoms is less than 10% of the mean velocity, thus reducing chromatic aberration. The mechanical grating has 100 nm wide slits, which are aligned with the nodes of the standing wave. This way only atoms close to the nodes will be transmitted by the grating, thus largely eliminating spherical aberration so that the background vanishes. Figure 1.3 shows a SEM image of a grating that will be used. The slits are separated by $744.0 \pm 0.7 \text{ nm}$, i.e., four periods $\lambda/2$ of the standing wave. The slit width is 100 nm , etched into the SiN substrate material over an area of $250 \times 250 \mu\text{m}^2$. The total number of slits is therefore 336.

The effects using a supersonic beam source with a mechanical grating is shown schematically in Fig. 1.2(b). Background-free sub- 10 nm Fe structures can be produced with this configuration, provided that surface diffusion of the deposited Fe atoms can be minimized to an insignificant factor.

Improved laser focusing offers some advantages compared to alternatives such as optical lithography and e-beam, ion or X-ray lithography. The fundamental limitation of optical lithography is set by approximately half the wavelength used, which at present results in a limit of

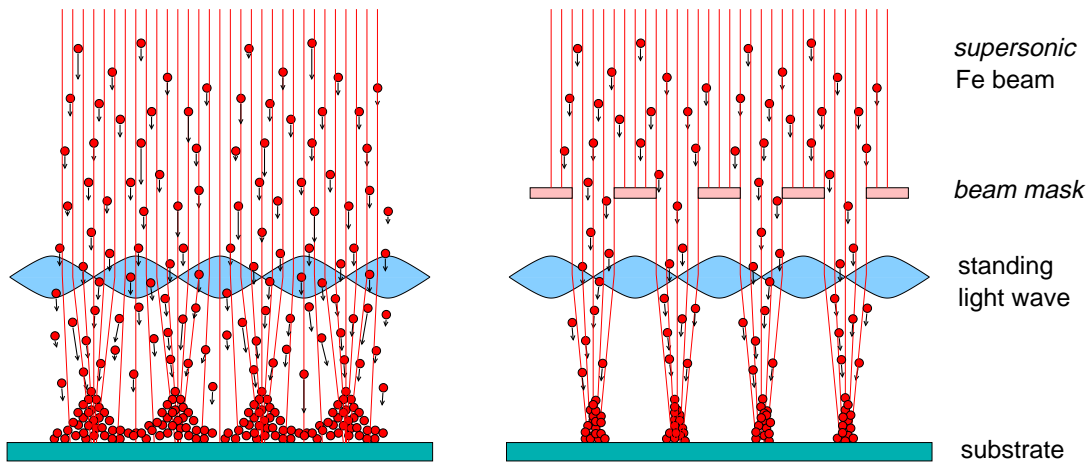


Figure 1.2: Laser focusing (a) and improved laser focusing (b) of an atomic beam. The nodes of the standing wave act as microlenses for the individual atoms. Periodic structures are grown at the focal plane where the substrate is located. Chromatic and spherical aberration of the microlenses can be reduced by using a supersonic beam and a mechanical grating upstream of the standing wave, respectively. The resulting well isolated Fe structures are 10 nm in size with a perfect periodicity of 186 nm.

around 70 nm. In comparison with alternatives like e-beam, ion or X-ray lithography, there are no limits set by charged particle interactions. Furthermore, the relatively low thermal speed of the atoms does not cause any surface damage, which is a problem when X-rays and charged particles are used.

4 Experimental setup for improved laser focusing

Figure 1.4 schematically shows the setup that is currently being developed. A supersonic Fe beam source generates a nearly monochromatic atomic Fe beam. This beam is first collimated by transverse laser cooling, reducing the beam divergence to below $100 \mu\text{rad}$. Two sets of counter-propagating laser beams, one set for each transverse direction, will align the velocity of the atoms to the desired beam axis. After the laser cooling section the beam is masked by a mechanical grating with holes of 100 nm diameter for dot patterns and slits of 100 nm width for line patterns. The masks have been produced with e-beam lithography and have a usable area of $250 \times 250 \mu\text{m}$. A standing wave with a $1/e^2$ half width of typically $10 \mu\text{m}$ in the beam direction will finally focus the atoms onto the substrate. The standing wave can either be two-dimensional for producing dots, or one-dimensional for depositing lines. The deposition rate of the structures will be in the range of 10 nm/h, in which case a processing time of approximately two hours is typical for the growth of the structures. Since Fe is chemically unstable in air, the samples need to be passivated with, e.g., a gold capping layer. A sample exchange unit will transport the samples into the passivation chamber. A vacuum better than 10^{-9} Torr is necessary for clean deposition and passivation.

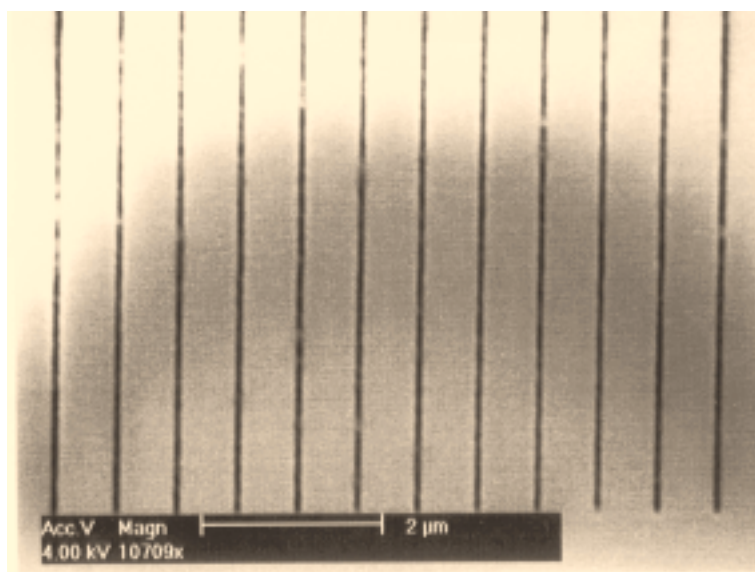


Figure 1.3: SEM image of a mechanical grating used as a beam mask for Fe laser focusing. The grating is made of SiN, into which 100 nm slits are etched. The slits are separated by 744 nm, which corresponds to every four periods of the standing wave. The usable area of the grating is $250 \times 250 \mu\text{m}^2$.

5 Contents of thesis

In the next chapter we motivate the choice of Fe for laser manipulation. Iron is not the only interesting ferromagnetic element to consider. However, there are a few aspects, such as laser manipulation, that put requirements on the atomic properties. Fe turns out to be the most suitable, and, fortunately, also the most interesting for this purpose.

The development of the supersonic Fe beam source turned out to a task that was extremely difficult from a practical point of view. Commercial evaporation sources are not suited for our experiment, since they generate thermal beams with a large velocity spread. Our solution to this problem is to use a high pressure seed gas (argon) which carries the Fe vapor into the vacuum by expansion through a $200 \mu\text{m}$ nozzle at a temperature of 2000 K. The Fe beam then becomes supersonic: the velocity spread of the atoms decreases to below 8% of the average beam velocity. The development and performance of the supersonic Fe beam source is described in Chapter 3.

Laser cooling and laser focusing require a frequency stabilized laser system locked to the atomic resonance frequency of Fe, which corresponds to a UV wavelength of 372 nm. However, high power UV CW-lasers are commercially not available. Therefore, an appropriate laser system has to be built which fulfills all the requirements. The development of this system is described in Chapter 4.

The theory of laser focusing is discussed in Chapter 5. A thorough understanding of laser focusing is required for the production of sub-10 nm structures, focusing on fundamental and practical limits involved in this process. Numerical simulations using various models have been performed. With the results, the effect of using a supersonic Fe beam and a mechanical grating

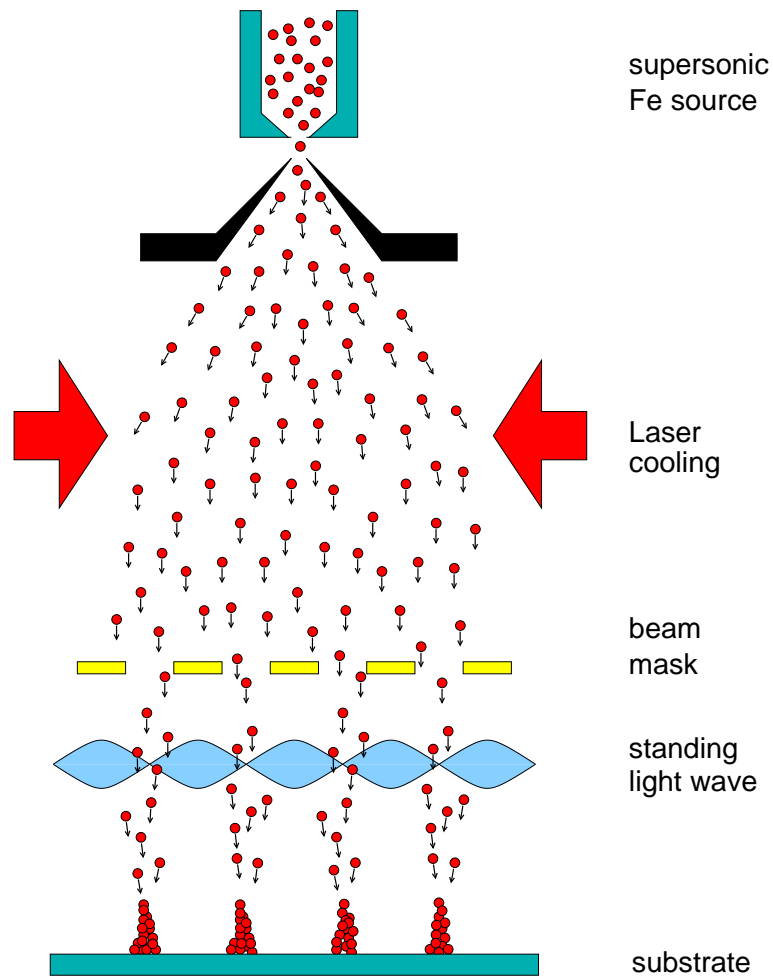


Figure 1.4: Experimental setup for laser focusing of Fe atoms to sub-10 nm structures. A nearly monochromatic Fe beam generated by a supersonic Fe beam source is collimated by transverse laser cooling and focused by a standing wave onto a substrate. A 100 nm mechanical transmission grating minimizes spherical aberration.

are demonstrated. Also, the effect of the finite Fe beam divergence after laser cooling has been studied. This puts an upper limit on the acceptable beam divergence and therefore sets a requirement on the performance of the laser cooling process, which is described in Chapter 6. The fundamental limit on laser focusing due to atomic beam diffraction is also investigated.

Laser cooling of the Fe beam is a necessary step before laser focusing can be applied experimentally. Laser cooling is a well established technique [5, 15]. However, laser cooling of Fe has never been performed. There is a significant leak in the used atomic Fe transition. This leads to the rather unusual restriction of reducing the number of scattered photons during the cooling process, at a cost to the beam divergence. Investigation of this process is presented in Chapter 6, in which numerical simulations on laser cooling of an atomic Fe beam are performed to predict if a sufficiently low Fe beam divergence can be obtained.

6 Applications of atom lithography

Laser focusing of atoms allows the fabrication of high quality structures. As shown before, we expect to deposit structures with excellent control of size, shape and mutual separation. The combination of a high quality Fe beam with beam masking leads to structures below 10 nm with no background. Perfect periodicity of the structures is guaranteed, matching the periodicity of the standing light wave ($\lambda/2 = 186$ nm). The perfect periodicity of the structures can be used for nanometer scale length calibration for scanning probe and electron microscopy.

The density of the dots can further be increased simply by moving the substrate in steps of, e.g., one sixth of the period (31 nm) during processing. The result is a smaller period structure with a dot separation limited only by the minimum feature size.

One of the most promising applications of laser focusing is the production of test samples with ferromagnetic dots for the study of ultra-high density recording. A periodicity of 31 nm leads to a hypothetical storage density of 0.7 Tbit in² inch, which is more than an order of magnitude higher than the density of 35 Gbit in² found in top-of-the-line disc drives today. However, the tiny overall area of the produced samples makes the application of laser focusing as a commercial production technique for magnetic storage media improbable. With laser focusing, this area is limited to 250×250 μm . Scaling to areas larger than a few square millimeters will be very difficult due to the required laser power for focusing and problems associated with the production of large masks.

The storage media of today's magnetic hard disk drives may be viewed as an array of magnetic nanoparticles. The magnetic coating of the disk consists of a ternary Co-Pt-Cr mixture which segregates into magnetic Co-Pt grains. These grains are magnetically separated by Cr at the grain boundaries [16]. Typical grain sizes are 10-20 nm, using about 10^3 grains per bit. The grains segregate randomly, which introduces statistical noise into the read-out signal due to variations in grain size, coercivity and domain structure. This explains the large numbers of grains that are required to reduce these fluctuations in a device.

The ultimate goal in magnetic recording is to use a single particle per bit, or quantized recording. It is aimed at producing single domain particles close to the super-paramagnetic limit with uniform switching properties. It is known that a ferromagnetic nanoparticle does not retain a fixed magnetization direction when its size is decreased. At some point the orientation is no longer stable since the thermal energy becomes comparable to the magnetic energy. It is

estimated that this so-called super-paramagnetic limit is around 10 nm [14]. Since we expect to be able to reach this dimension, it becomes possible to investigate this limit for Fe. It becomes clear from a look at the fundamental limits that magnetic storage has much room to continue its rapid development and that the control of magnetic nanostructures will play a key role for further advances.

In general, new effects that are likely to occur in complex patterned media of magnetic materials on the nanometer scale can also be investigated. Giant Magneto Resistance (GMR) was discovered in a 2D layered structure of Cu and Co [1]. Magnetoresistance is a change in the resistivity under the influence of a magnetic field. Anisotropic magnetoresistance (AMR) in $\text{Ni}_{0.8}\text{Fe}_{0.2}$ gives a 2% change in resistivity [17, 18], whereas giant magnetoresistance gives a 10% change at a low switching field of 10 Oe [18]. Currently, the GMR effect is used in reading heads of disk drives. Present challenges are directed towards lowering of the switching field while keeping a large magnetoresistance.

It is generally believed that upon a further reduction in dimensionality new physical phenomena will again show up, although for nanomagnetic lines (1D) and dots (0D) the research is still in its embryonic stage. As magnetic particles become smaller, they pass through a series of magnetic phases. The first change comes when their size shrinks below a domain wall thickness (typically 0.1-1 μm), which favors single-domain behavior. Small particles have a large surface to bulk ratio, so that magnetic properties are strongly affected by the surface. Reduced or enhanced magnetism are two of the many effects that can occur in this situation. The magnetic behavior of the 1D and 0D structures can very well lead to discoveries which are valuable for both scientific and commercial purposes.

Even if commercial applications seem to be somewhat further in the future, laser focusing of iron has the immediate potential of giving new fundamental insights in the field of nanomagnetics.

References

- [1] G.A. Prinz, *Physics Today*, 58, April 1995
- [2] see <http://www.almaden.ibm.com/sst>
- [3] B. Brezger, Th. Schulze, U. Drodofsky, J. Stuhler, S. Nowak, T. Pfau, and J. Mlynek, *J. Vac. Sci. Technol.* **B15**, 2905 (1997)
- [4] J.J. McClelland, R.E. Scholten, E.C. Palm, and R.J. Celotta, *Science* **262**, 877 (1993)
- [5] M. Drewsen, U. Drodofsky, C. Weber, G. Schreiber, and J.Mlynek, *J. Phys. B* **29**, 843 (1996)
- [6] S.J. Rehse, R.W. McGowan, and S.A. Lee, *Appl. Phys. B* **70**, 657 (2000)
- [7] McGowan, R.W., D. Giltner, and Siu Au Lee, *Opt. Lett.* **20**, 2535 (1995)
- [8] S.J.H.Petra, L.Feenstra, W.Vassen and W.Hogervorst, International Quantum Electronics Conference CLEO/Europe-IQEC 2000
- [9] K.K. Berggren, A. Bard, J.L. Wilbur, J.D. Gillaspay, A.G. Helg, J.J. McClelland, S.L. Rolston, W.D. Phillips, M.Prentiss, and G.M. Whitesides, *Science* **269**, 1255 (1995)

-
- [10] P. Engels, S. Salewski, H. Levsen, K. Sengstock, and W. Ertmer, *Appl. Phys. B* **69**, 407 (1999)
- [11] G. Timp, R.E. Behringer, D.M. Tennant, and J.E. Cunningham, *Phys. Rev. Lett.* **69**, 1636 (1992)
- [12] F. Lison, H.J. Adams, P. Schuh, D. Haubrich, and D. Meschede, *Appl. Phys. B* **65**, 419 (1997)
- [13] W.R. Anderson, C.C. Bradley, J.J. McClelland, and R.J. Celotta, *Phys. Rev. A* **59**, 2476 (1999)
- [14] F.J. Himpsel, J.E. Ortega, G.J. Mankey, and R.F. Willis, *Adv. Phys.* **47**, 511 (1998)
- [15] M.D. Hoogerland, J.P.J. Driessen, E.J.D. Vredenburg, H.J.L. Megens, M.P. Schuwer, H.C.W. Beijerinck, and K.A.H van Leeuwen, *Appl. Phys. B* **62**, 323 (1996)
- [16] H.N. Betram and J.G. Zhu, *Solid St. Phys.* **46**, 271 (1992)
- [17] E. Grochowsky, and D.A. Thompson, *IEEE Trans. Magn.* **30**, 3797 (1994)
- [18] D.E. Heim, R.E. Fontana, C. Tsang, V.S. Speriosu, B.A. Gurney, M.L. Williams, *IEEE Trans. Magn.* **30**, 316 (1994)

Chapter 2

Why iron?

1 Ferromagnetic elements

The investigation of magnetic properties at reduced dimensionality of ferromagnetic materials is very interesting. The three ferromagnetic materials at room temperature are Fe, Co and Ni. A fourth material, Gd, is sometimes referred to as the fourth ferromagnet, although the Curie temperature is slightly below room temperature, leaving Gd as a less appropriate candidate for the research in the field of nanomagnetism.

Elements such as Cr, Mn, Fe, Co, Ni have a partially filled $3d$ -shell. The atomic magnetic moment is dominated by the $3d$ -electrons with high angular momentum. However, when atoms are squeezed into a solid, some of the electrons are forced into common spatial wave functions which forces their spins to align antiparallel and reduces the overall magnetic moment. For example, the moment of $5\mu_B$ in the free Cr atom is reduced by an order of magnitude in the solid: Cr forms an antiferromagnetic solid.

For *ferromagnets* the energy bands in the solid are split in two subsets with opposing electron spin. The magnetic exchange splitting between the two spins is the key to ferromagnetism. Because of the exchange splitting the higher-energy band is less filled than the lower-energy band, thus creating the spin imbalance that creates the macroscopic magnetic moment. Most of the moment is carried by the $3d$ electrons (approximately 110%), whereas the s , p electrons are weakly polarized in the opposite direction (-10% of the total moment) [1].

Table I shows the magnetic properties of Fe, Co and Ni. It can be seen that for all three species the bulk phase magnetic moment is lower than the atomic moment with a factor of 2 to 3. Fe has the highest atomic and bulk phase magnetic moment of $4\mu_B$ and $2.2\mu_B$, respectively. The Curie temperature is lowest for Ni (628 K) and highest for Co (1393 K).

2 Isotopes

For the selection of a ferromagnetic element it is important to look at the stable isotopes of Fe, Co and Ni. The small nanostructures as shown in Fig. 1.4 are fabricated by laser manipulation. However, if the atomic beam consists of several isotopes, the laser light for beam collimation can only address one of the isotopes, since the frequency shift of an optical transition by the isotope effect is on the order of 100 MHz, much larger than the natural linewidth.

Table I also shows the natural abundance of the isotopes of Fe, Co and Ni. For Fe the most abundant isotope is ^{56}Fe , with a natural abundance of 92%. The remaining 8% mainly consists of ^{54}Fe (6%) and ^{57}Fe (2%). From this point of view, Fe is convenient for laser focusing. For Co the situation is even better, since there is only one stable isotope, which is ^{59}Co . Ni is a less convenient element because there are five Ni isotopes with a natural abundance above 1%. The two most dominant isotopes are ^{58}Ni (68%) and ^{60}Ni (23%), respectively. If Ni is used for laser focusing, then a significant background of ^{60}Ni will appear around the focused ^{58}Ni lines or dots.

However, the isotope composition of the atomic beam at the standing wave is changed since the atomic beam has been collimated by laser cooling. The improvement in ^{58}Ni beam collimation increases the ^{58}Ni beam flux downstream of the cooling region. This means that the fraction of ^{58}Ni in the collimated beam is significantly higher. This effect becomes more pronounced with increasing distance from the cooling region, which implies that the isotope background between the focused lines or dots will be smaller at a larger distance between the standing wave and the cooling region.

3 Atomic properties

The atomic properties of Fe, Co and Ni are listed in table I. Their ferromagnetic properties arise from the electrons in the $3d$ shell, which is filled with 6, 7 and 8 electrons for Fe, Co and Ni, respectively. The ground state configuration is important to consider. For example, a ground state Fe atom with atomic configuration of 5D_4 has an atomic spin $S = 2$ and an orbital angular momentum $L = 2$. Spin-orbit coupling results in a total angular momentum of $J = 0, 1, 2, 3, 4$, with the highest J value corresponding to the ground state. The states with smaller J value are separated in energy on the order of 43 to 130 meV, corresponding to 500 to 1500 K (for $J = 3$ to $J = 0$) above the ground state level. As a consequence, there will be a significant population of Fe atoms with a J value other than 4 when Fe is heated to 2000 K for the generation of an atomic Fe beam. The fraction of ground state Fe atoms is equal to

$$\frac{(2J_g + 1)}{\sum_{J=0}^{J_g} (2J + 1) \exp(-E_J/kT)}, \quad (2.1)$$

with J_g the ground state J value and E_J the energy of the atomic level with total angular momentum J . For Fe the ground state population with $J = 4$ at 2000 K is 50%. For Co and Ni these populations are higher due to a larger splitting of the energy levels, namely 56% and 70%, respectively.

For ^{59}Co the situation is more complex, since ^{59}Co has nuclear spin of $I = 7/2$, causing a hyperfine splitting of the $^4F_{9/2}$ ground state into eight levels with total angular momentum $F = 1, 2, \dots, 8$. This reduces the number of ground state ^{59}Co atoms at 2000 K from 56% (given by Eq. (2.1)) with an additional factor arising from the fact that all hyperfine levels are populated according to $(F_i + 1) / \sum_{F=1}^{F_g} (2F + 1)$. Therefore, at 2000 K only 12% of the ^{59}Co atoms are in the $^4F_{9/2}(F = 8)$ ground state. Hence, laser cooling is not practical as only 12% of the atoms can be cooled without any complicated repumping schemes, requiring many extra laser frequencies.

An atomic beam of Fe, Co and Ni is generated by thermal heating. For an adequate beam flux for laser focusing the vapor pressure should be in the range of 10^{-1} Torr. Table I gives the corresponding temperature. For the three materials considered this temperature lies in the range of 1920 to 1970 K. Unfortunately these are relatively high temperatures, which makes thermal evaporation difficult from a technical point of view.

4 Atomic transitions

Laser focusing of an atomic beam requires sufficient laser power at a wavelength corresponding to an atomic resonance frequency. Laser cooling requires in addition a *closed or nearly closed* two-level transition [2]. This is because laser cooling is based on the dissipative radiation force, which arises from absorption and spontaneous emission of photons. This process only works if the atomic upper state always decays back to the initial state, from which the process can be repeated. Laser cooling is therefore a many-photon process, so that the leak rate from the upper state to a third state should be as low as possible, preferably zero.

Despite the fact that there are a large number of atomic transitions from the ground state in Fe, Co and Ni [3], most of them are, however, not closed. The most appropriate transitions for laser cooling are listed in Table I.

For Fe there is a transition at a wavelength of 372 nm. The decay rate of the upper state to the ground state is 16.2 Mrad/s, which is convenient for laser cooling. The saturation intensity is 62 W/m². For example, a laser cooling beam of 5×100 mm² with a saturation parameter of unity (which is typical for laser cooling) requires a total laser power of 31 mW. The wavelength of 372 nm can be obtained utilizing an LBO crystal to frequency double a 744 nm beam generated by a Ti:S (titanium sapphire) laser.

For Co there is a very strong closed transition at 240 nm. The upper state decay rate is 360 Mrad/s, and the saturation intensity is 5156 W/m². However, generating a high power CW-laser beam in this wavelength range is practically impossible. Frequency doubling with a BBO crystal has a conversion efficiency on the order of only a few percent in this wavelength regime [5].

There is also a closed transition for Ni from the ground state. The corresponding wavelength is 323 nm. Frequency doubling by an LiIO₃ crystal of a 646 nm beam of a dye laser will generate a beam at 323 nm [4]. However, the doubling efficiency will be too low to obtain a power in the range of 150-500 mW.

The overall best atomic transition for the purpose of laser cooling and focusing is the transition at 372 nm from ground state Fe. However, there is a significant leak of 1:243 from the upper state, which means that there is a probability of $p = 1/243$ that the upper state will decay to other states (5F_5 or 5F_4), which are metastable. Once in one of these states, the Fe atom cannot be used for laser cooling and focusing. The number of photons used for the cooling process should therefore be kept small. If, for example, 100 photons are used, the fraction of remaining ground state Fe atoms is equal to $(1 - p)^{100} = (242/243)^{100} = 66\%$.

In fact, the transition for Ni at 323 nm can also be used for laser cooling. This transition is fully closed. However, it is uncertain whether sufficient power for laser cooling and focusing can be generated.

Table I: Properties of the ferromagnetic elements Fe, Co and Ni.

	Fe	Co	Ni
magnetic properties			
atomic magn. moment (μ_B)	4	3	2
bulk phase magn. moment (μ_B)	2.2	1.7	0.6
bulk phase crystal structure	bcc	hcp	fcc
Curie temperature (K)	1044	1393	628
isotopes			
Z	26	27	28
most abundant	^{56}Fe 92%	^{59}Co 100%	^{58}Ni 68%
other isotopes	^{54}Fe 6% ^{57}Fe 2%		^{60}Ni 26% ^{62}Ni 4% ^{61}Ni 1% ^{64}Ni 1%
material properties			
melting point (K)	1811	1768	1728
boiling point (K)	3134	3200	3168
T(K) @ 10^{-1} Torr vapor pressure	1920	1960	1970
surface energy (J/m^2)	2.9	2.7	2.5
atomic properties			
electron conf.	$3d^6 4s^2$	$3d^7 4s^2$	$3d^8 4s^2$
ground state conf.	5D_4	$^4F_{9/2}$	3F_4
ground state J	4	9/2	4
nuclear spin I	0 (^{56}Fe)	7/2 (^{59}Co)	0 (^{58}Ni)
ground state population @ 2000 K	50%	12%	70%
atomic transitions from ground state			
transition	$^5D_4 \rightarrow ^5F_5$	$^4F_{9/2} \rightarrow ^4G_{11/2}$	$^3F_4 \rightarrow ^3G_5$
wavelength (nm)	372.0	240.5	323.4
Γ upper state (Mrad/s)	16.2	360	7.3
saturation intensity I_s (W/m^2)	62	5156	43
leak rate	1:243	0	0

5 Laser manipulation of Fe

The requirements of high available laser power for laser manipulation and a suitable transition for laser cooling leaves only one option in the choice of one of the ferromagnetic elements Fe, Co and Ni, i.e., Fe. The most common Fe isotope is ^{56}Fe , with a relatively high abundance of 92%. This is convenient since the remaining isotopes will not affect the laser focusing significantly. Unfortunately, Fe is difficult to evaporate by thermal heating, since temperatures up to 2000 K are required. At this temperature the thermal occupation of the ground state level is 50%, which means that the remaining 50% cannot be used for the experiments.

Fe has a surface energy of 2.9 J/m^2 , high compared to metals or semiconductor materials. This also holds for the other magnetic materials as Co and Ni, which can be ascribed to the partially filled d shell. Care has to be taken in the choice of the substrate material onto which Fe is deposited. If the surface energy of the substrate is lower than the Fe surface energy, the substrate atoms will tend to trade places with the Fe atoms during deposition. We have confirmed this effect experimentally. A two nanometer thick Fe layer was deposited onto a gold substrate. The composition of the surface was determined using low energy ion spectroscopy (LEIS). It turned out that a large fraction, on the order of 50%, of the surface was covered with gold atoms. Solutions to overcome this problem are to deposit at low temperatures or to deposit at high deposition rate. The first solution will be difficult to apply from a practical point of view. The second solution is experimentally not feasible.

Transition metals as W, Mo and Ta have a surface energy which is even higher than the Fe surface energy. Therefore these materials are more convenient as a substrate for the deposition of Fe structures. Still, care has to be taken to prevent diffusion of Fe on the substrate during the growth of the first monolayers.

Tungsten (W) appears to be the best substrate material for this purpose [6]. It has the convenient property that it is resistant against oxidation in air at room temperature, making the cleaning of the substrate more easy. A second advantage of W is that it has a very strong binding with Fe [7, 8]. The four electrons in the $5d$ shell of W and the six electrons in the $3d$ shell of Fe make a completely filled d shell of Fe-W, resulting in a binding energy of 0.8 eV. For comparison, the Fe-Mo and Fe-Ta binding energies are approximately 0.2 eV [9].

Due to the strong binding of Fe-W the diffusion of an Fe atom on a smooth W surface is relatively slow. At room temperature this diffusion speed is on the order of 0.1 nm/s [6]. This is much lower than the diffusion of atomic Fe on an Fe surface, which is approximately 75 nm/s [6]. For the growth of isolated Fe structures this is convenient. Although the diffusion of Fe on Fe is extremely fast, the length scale of the diffusion is limited to the dimensions of the Fe structures, since an Fe atom needs to take several step-down energy barriers of 1.0 eV each to leave the Fe structure [10]. The resulting diffusion speed dramatically decreases already to 0.2 nm/s because of one step-down energy barrier. Furthermore, the large probability of nucleation of two Fe atoms on the same terrace make the Fe diffusion speed even smaller by many orders of magnitude. As long as the deposition rate of Fe is larger than 2 monolayers per hour [6], the Fe nanostructures are stable at room temperature. Experimental deposition rates are on the order of 10^1 to 10^2 monolayers per hour, so that stable Fe structures on a tungsten substrate are guaranteed.

References

- [1] F.J. Himpsel, J.E. Ortega, G.J. Mankey, and R.F. Willis, *Adv. Phys.* **47**, 511 (1998)
- [2] M.D. Hoogerland, J.P.J. Driessen, E.J.D. Vredenburg, H.J.L. Megens, M.P. Schuwer, H.C.W. Beijerinck, and K.A.H van Leeuwen, *Appl. Phys. B* **62**, 323 (1996)
- [3] see http://physics.nist.gov/cgi-bin/AtData/main_asd
- [4] S.J. Rehse, R.W. McGowan, and S.A. Lee, *Appl. Phys. B* **70**, 657 (2000)
- [5] see <http://www.castech-us.com/bbotun.htm>
- [6] K.M.R. v/d Stam, *The dynamic behaviour of Fe nanostructures*, internal report, Eindhoven University of Technology (2001)
- [7] J. Malzbender, *Surf. Sc.* **414**, 187 (1998)
- [8] T.T. Tsong, *Rep. Prog. Phys.* **51**, 759 (1988)
- [9] F.R. de Boer, R. Boom, and W.C.M. Mattens, *Cohesion in metals*, Amsterdam North-Holland (1988)
- [10] R.L. Swoebel, E.J. Shipsey, *J. Appl. Phys.* **37**, 3682 (1966)

Chapter 3

Supersonic Fe beam source for chromatic aberration-free laser focusing

R.C.M. Bosch, H.C.W. Beijerinck, P. van der Straten, and K.A.H. van Leeuwen
*Department of Applied Physics, Eindhoven University of Technology, P.O. box 513,
5600 MB Eindhoven, The Netherlands*

(to be published in European Physical Journal Applied Physics)

A monochromatic Fe beam is generated by heated supersonic expansion of argon seeded with Fe vapor. At a nozzle temperature of 1930 K and 800 Torr argon inlet pressure the Fe beam has an axial velocity spread of 8% and intensity of $3 \times 10^{15} \text{ s}^{-1} \text{ sr}^{-1}$, corresponding to a deposition rate of 10 nm/h at 150 mm from the nozzle. The two-chamber alumina crucibles are chemically stable for liquid Fe. With 400 mm³ Fe we have operated for more than 200 hours without reloading. The power consumption at 1930 K is 750 W. Temperature stability at constant power (without feedback) is better than 30 K. The source is intended for deposition of nanostructures by laser focusing of the Fe beam. The small axial velocity spread virtually eliminates the increase in focal spot size due to chromatic aberration.

1 Introduction

Laser focusing of atoms for the production of periodic nanostructures is increasingly gaining interest. Arrays of lines and dots have been produced by etching with metastable atoms, He* [1, 2], Ne* [3], and Ar* [4], etching with alkali atoms, Na [5] and Cs [6], and by deposition of metal atoms, Cr [2, 7] and Al [8]. The supersonic Fe source which is presented in this paper has been developed for the fabrication of periodic structures of Fe by laser focusing. This particular atom has been chosen for its ferromagnetic properties. The fabrication of arrays of nanometer-sized Fe lines and dots would provide an experimental entry into a new fascinating field of 1D and 0D nanomagnetism [9].

The technique of laser focusing for the production of these nanostructures requires a well defined atomic beam. Just as in conventional optics the quality of the focused image is limited

by initial beam collimation and chromatic aberration. These two aspects are determined by the initial spread in transverse velocity of the atomic beam and the spread in axial velocity of the atoms, respectively. Thus, for a controlled deposition of arrays the Fe beam needs to be collimated and “monochromatic” (single-axial-velocity). The first property can be established by aperturing the beam or by transverse Doppler cooling [10], resulting in beams collimated below 0.1 mrad. Monochromatic beams can be generated by Zeeman slowing of a thermal beam [5], or by using a supersonic beam [11]. The relatively low axial velocity spread in a supersonic beam is characterized by a high speed ratio S , defined by the ratio of the average axial velocity to the axial velocity spread. In experiments on laser focusing of metal atoms as Cr and Al, the atomic beam is generated by an effusive source, resulting in a thermal beam with an axial velocity spread comparable to the average velocity. The lack of monochromatic beams of metal atoms is one of the reasons that structures below 10 nm have not yet been produced. Calculations on laser focusing of a collimated Fe beam of 0.1 mrad show that the focal spot size decreases from 15 nm to 8 nm if a supersonic rather than a thermal beam is used [12].

This paper will describe the development of a supersonic Fe evaporation source. Supersonic beam sources for high-melting-point metals such as Fe are uncommon, because they pose special construction problems due to the required high temperature, large pressure and small exit nozzle. Expertise in this field was developed by the group of Hagena [13]. We have used the basic concept of their high temperature evaporation source for the generation of metal cluster beams. The result is the construction of a supersonic Fe evaporation source, containing a crucible which is chemically stable with molten Fe at temperatures well above 2000 K, and an oven with small temperature gradients to prevent diffusion of Fe and nozzle clogging. A supersonic Fe beam with center line intensities of up to 10^{16} atoms $\text{s}^{-1}\text{sr}^{-1}$ can be generated. With these intensities, the deposition rate of structures is at least 20 nm/h at 150 mm from the nozzle, requiring a background pressure of 10^{-9} Torr or lower to minimize contamination.

2 Seeded supersonic expansions

Supersonic beams are obtained by expanding a relatively high pressure ($p_0 \sim 10 - 10^4$ Torr) gas through a small nozzle into vacuum [14]. Producing such an expansion from pure Fe vapor is not practical, requiring an unrealistically high temperature. Thus, we use Ar as a high pressure carrier gas into which Fe is seeded at a moderate pressure. Other noble gases such as He or Ne could also be used. However, the resulting beam velocity (which is determined by the thermal velocity of the carrier gas) would be too high for adequate laser cooling and laser focusing. The Ar flux \dot{N} (atoms/s) and undisturbed Ar center line intensity I_0^{id} (atoms/s/sr) are given by [11]

$$\dot{N} = 0.513 n_0 \alpha_0 (\pi d^2 / 4) \quad (3.1)$$

$$I_0^{id} = \kappa \dot{N} / \pi, \quad (3.2)$$

where $n_0 = p_0 / kT_0$ is the reservoir density, $\alpha_0 = (2kT_0/m)^{1/2}$ the thermal velocity and d the nozzle diameter. For sonic nozzles the value of the peaking factor κ is equal to 2.08 [11]. Due to the high reservoir pressure the flow of the expansion is continuous during the first few nozzle diameters. In the expansion both the local temperature $T(z)$ and local density $n(z)$ decrease with the distance z from the nozzle. Most of the thermal energy of the atoms in the reservoir

will be transferred to kinetic energy in the direction of propagation, leading to the lowering of the local temperature and to an increase in the flow velocity. At some point, a few nozzle diameters from the nozzle, the stream lines become straight lines resulting in a radial expansion with an angular intensity distribution $I_\theta \propto \cos^3 \theta$, with θ the angle with respect to the center-line of the expansion. A back projection of these stream lines onto the nozzle plane results in a Gaussian distribution with a rms width defined as the virtual source radius R_v . When the beam is collimated by a pinhole some distance downstream, the virtual source radius determines the divergence of the transmitted beam.

When the local density becomes so low that collisions are no longer significant, the atoms move freely in straight line trajectories. The parallel temperature freezes [11] and is given by $\frac{1}{2}kT_\parallel = \frac{1}{2}m\alpha_\parallel^2$. The axial velocity distribution of the supersonic beam is then given by

$$P(v) \propto \left(\frac{v}{u}\right)^3 \exp\left[-\left(\frac{v-u}{u}\right)^2 S^2\right], \quad (3.3)$$

with the speed ratio S is defined as the ratio of the final flow velocity u to the final parallel velocity spread α_\parallel . The final flow velocity can be calculated from the enthalpy balance given by $\frac{5}{2}kT_0 = \frac{1}{2}mu^2 + \frac{3}{2}kT_\parallel$, resulting in

$$u = u_\infty \left(1 + \frac{3}{2}S^{-2}\right)^{1/2}, \quad (3.4)$$

with $u_\infty = (5kT_0/m)^{1/2}$ the final flow velocity for $S \rightarrow \infty$. Speed ratios of supersonic beams have been measured and calculated extensively [16]. The most widely used theoretical predictions are based on the sudden freeze model [11], resulting in

$$S = 19.1 \left(\frac{\Xi}{100}\right)^{0.495}, \quad (3.5)$$

where Ξ is the reservoir parameter which depends on the nozzle diameter d , the inlet pressure p_0 and oven temperature T_0 . For Ar the reservoir parameter Ξ can be expressed as [11]

$$\Xi = 100 \left(\frac{d}{0.2 \text{ mm}}\right) \left(\frac{p_0}{170 \text{ Torr}}\right) \left(\frac{T_0}{300 \text{ K}}\right)^{-4/3}. \quad (3.6)$$

Background pressures in the expansion chamber are on the order of 10^{-1} Torr, due to the large gas load into the vacuum system ($\dot{N} > 10^{20}$ atoms/s). As a result strong shock waves appear at the boundaries of the Campargue-type expansion [15] and a conical skimmer has to be used to extract an atomic beam on the center line carefully without excessive loss of beam intensity. Inside the skimmer tip the beam is attenuated according to Beer's law, i.e., an exponential decrease with an exponent scaling with the local inverse Knudsen number Kn^{-1} . Since this number is proportional to the inlet pressure p_0 , scattering with background Ar atoms inside the skimmer tip leads to an exponential decrease of beam intensity with p_0 [16]:

$$I_0 = I_0^{id} \exp[-qp_0]. \quad (3.7)$$

A supersonic Fe beam is obtained by heating Fe inside the reservoir to temperatures up to 2000 K, corresponding to Fe vapor pressures in the range of 10^{-2} to 10^{-1} Torr. The Ar gas carries the Fe vapor and the mixture expands supersonically. If thermodynamic equilibrium between Ar and Fe is established in the continuum flow regime of the expansion, the beam velocities and beam temperature of both species will be equal and their values will be almost the same as for a pure Ar expansion. The speed ratio of Fe is then given by

$$\frac{S_{Fe}}{S_{Ar}} = \left(\frac{m_{Fe}}{m_{Ar}} \right)^{1/2} \quad (3.8)$$

and is 18 % higher than the speed ratio of Ar (mass ratio of 56 over 40). However, Eq. (3.8) is an upper limit. Experimental values can differ significantly especially for heavier species, whose cooling process due to collisions with the much lighter carrier gas atoms is not that efficient. A closer look at the cooling of dilute binary mixtures in a supersonic expansion is given in [17], resulting in a modification of Eq. (3.8):

$$\frac{S_M}{S_m} = \left(\frac{M}{m} \right)^{1/2} \left[0.33 \left(\frac{m}{M} - 1 \right) + 1 \right]^{1/2} \left(\frac{C_{6m}}{C_{6M}} \right)^{1/12}, \quad (3.9)$$

where M is the mass of the dilute heavy atoms, and m the mass of the light atoms driving the expansion. The second and third term of Eq. (3.9) represent the efficiency of the cooling of species with different masses and cross sections. For noble gases collision processes at low temperature are dominated by the long-range attractive branch of $V(r) \propto -C_6/r^6$ with C_6 the Van der Waals constant, resulting in cross sections that can be written as $(C_6/kT)^{1/3}$. For metal atoms such as Fe, the collision cross section has been estimated by experiments on metal cluster beams [18], leading to an artificial C_6 coefficient which is a factor of 6.3 larger than the C_6 coefficient of argon. Equation (3.9) then predicts an Fe speed ratio which is 3% lower than the Ar speed ratio.

The Fe beam intensity between nozzle and skimmer is just the undisturbed Ar beam intensity times the ratio of the Fe vapor pressure p_v to the Ar inlet pressure p_0 :

$$I_{0,Fe}^{id} = \frac{p_v}{p_0} I_0^{id}, \quad (3.10)$$

which is independent of the argon inlet pressure p_0 , since I_0^{id} is proportional to p_0 according to Eqs. (3.1) and (3.2). Due to collisions between Fe atoms with Ar atoms at the skimmer tip, the Fe beam is attenuated by

$$I_{0,Fe} = I_{0,Fe}^{id} \exp \left[-q (C_{6M}/C_{6m})^{1/6} p_0 \right], \quad (3.11)$$

with a different exponential decay factor than the argon beam attenuation according to Eq. (3.7), due to different cross sections of Fe and Ar represented by the coefficients C_{6M} and C_{6m} . Since the speed ratio of Fe increases with increasing p_0 according to Eq. (3.5) and the skimmer transmission decreases exponentially with p_0 , a compromise has to be chosen between speed ratio and beam intensity.

3 Supersonic Fe beam source

Figure 3.1 shows a drawing of the supersonic Fe source. Different crucible materials have been tested for their thermal shock resistance and chemical stability with liquid Fe at $T > 1800$ K. The most important materials and the corresponding crucible constructions that have been tested are shown in Fig. 3.2. Eventually, alumina crucibles with a nozzle diameter of $230 \mu\text{m}$ have been used.

The crucible is heated by a high density graphite heating coil. The coil is doubly wound with a cross section of $3 \times 5 \text{ mm}^2$, necessary because of the high electrical resistance of graphite. The last turn which is located at the nozzle has been made thin ($1.5 \times 5 \text{ mm}^2$) to increase the resistance power output, to keep the nozzle hotter than the rest of the crucible. The total resistance is 0.5Ω , convenient for DC heating.

To minimize the input power and to reduce temperature gradients, 20 layers of wrapped tantalum foil heating shield are used in the radial direction and 5 layers at the nozzle side. An opening of 20 mm diameter allows an undisturbed supersonic expansion of the Ar gas. The outside stainless steel cylindrical mount is water cooled. With this construction, the main contribution to heat losses of the oven are radiative heat loss out of the front side opening and conduction heat loss through the heating coil.

The crucible assembly is a separate unit that can be removed from the heating unit very easily for maintenance or reloading of metal. The heating coil has proven to be very stable and durable and has been run on and off for several years up to now without any signs of deterioration. The concept of a separate crucible assembly combined with a graphite heating coil, has been used by Hagen for the generation of metal cluster beams [13]. His design formed the basis of our Fe source design.

High density graphite crucibles (as shown in Fig. 3.2(a) and 3.2(b)) were tested first, as graphite is easily machinable into a variety of different shapes, with a threaded nozzle assembly which makes reloading of metal very easy. The temperature was monitored using a W Re(3%/26%) thermocouple inserted in a small hole in the crucible wall at the position of the melt. However, problems arose at temperatures above the Fe melting point (1800 K), where molten Fe reacts with the graphite crucible wall at a rate of typically 0.1 mm/h. An insert in the graphite reservoir made of boron nitride (BN) increased the lifetime. However, the nozzle was attacked by Fe vapor, causing the nozzle size to increase by approximately 10% after ten hours of operation.

Crucibles made entirely of BN (Fig. 3.2(c)) were also tested. These crucibles can operate at slightly higher temperatures. However, above 2000 K deterioration by the molten Fe was also observed.

Highly purified alumina (>99,7%) (Fig. 3.2(d)) was found to have high tolerance to molten Fe. The maximum operating temperature was 2200 K, above which this material starts to sublime. Alumina is difficult to machine, and in particular, the fabrication of the nozzle of $230 \mu\text{m}$ diameter could only be realized by laser ablation. The assembly consists of two alumina tubes, the smaller one with a 1 mm orifice inserted into the larger nozzle tube. This way diffusion of the molten metal into the gas feed is prohibited by a constant flow of Ar out of the 1 mm orifice into the reservoir. Because of the loose fit between the two tubes, Ar also flows in between the two tube walls into the reservoir and prevents the metal vapor from diffusing in between the tube walls. The smaller tube can also be removed easily, making a reload of metal possible.

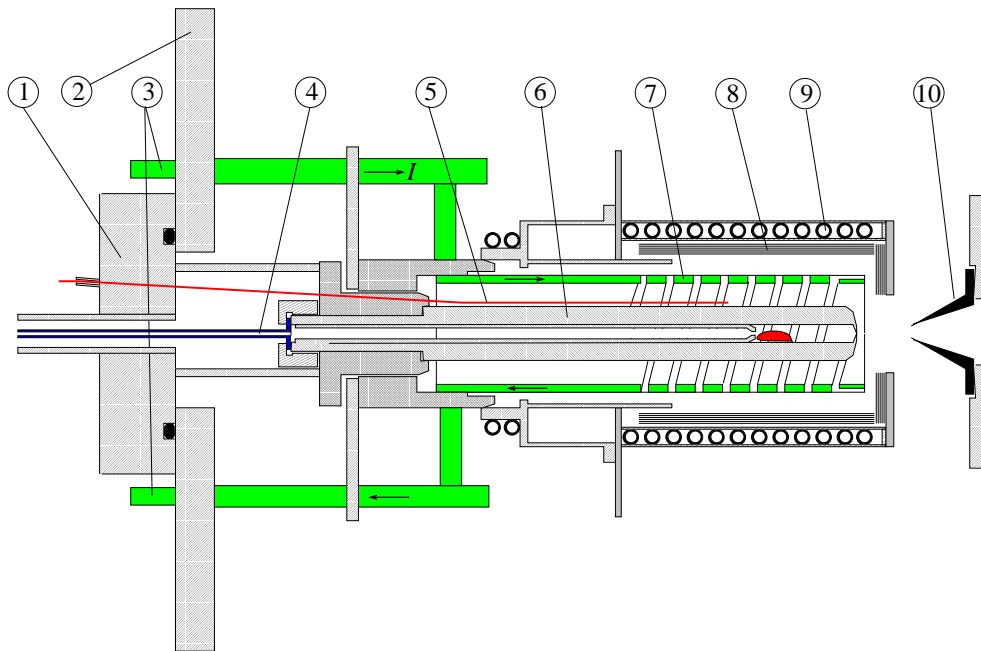


Figure 3.1: Schematic view of the supersonic metal evaporation source: 1) flange with crucible unit, 2) flange with heating unit, 3) copper feed through for DC heating, 4) tantalum tube for argon gas inlet, 5) W Re(3%/26%) thermocouple, 6) graphite crucible, 7) heating coil, 8) radiation shields, 9) water cooled stainless steel mount, 10) graphite skimmer

Table I gives an overview of the most relevant properties of the Fe source.

4 Experimental setup

The beam properties of Fe and seed gas Ar have been determined using a time-of-flight setup with a mass spectrometer as detector to measure the relative beam intensities of Fe and Ar. A calibration procedure was used in order to obtain absolute values. Undisturbed Ar beam intensities, i.e., an ideal Ar beam that is not attenuated at the skimmer, can be calculated using Eqs. (3.1) and (3.2). However, experimental Ar beam intensities will be lower by a factor of $\exp(-qp_0)$ as given in Eq. (3.7). The parameter q of this factor can be determined by fitting the data shown in Fig. 3.3. In this graph the Ar detector signal (left vertical axis) is shown for various Ar inlet pressures in the range of 100 to 1000 Torr. The ideal beam intensity indicated by the dashed line is a straight line with a slope equal to the slope of the fit of the measured data serie at $p_0 = 0$. Absolute values for experimental beam intensities are obtained by multiplying the ideal beam intensity calculated with Eq. (3.2) with the decay factor $\exp(-qp_0)$. The result of the fit is given in Table I.

The Fe beam intensity can be determined in two ways: first by multiplying the calibrated Ar beam intensity with the ratio of the detector signal of Fe to Ar, secondly with the ratio of the Fe vapor pressure to the Ar inlet pressure according to Eqs. (3.10) and (3.11).

Speed ratios of all species can be determined by time-of-flight measurements using a rotating slotted disk type mechanical beam chopper and a mass spectrometer. The beam chopper

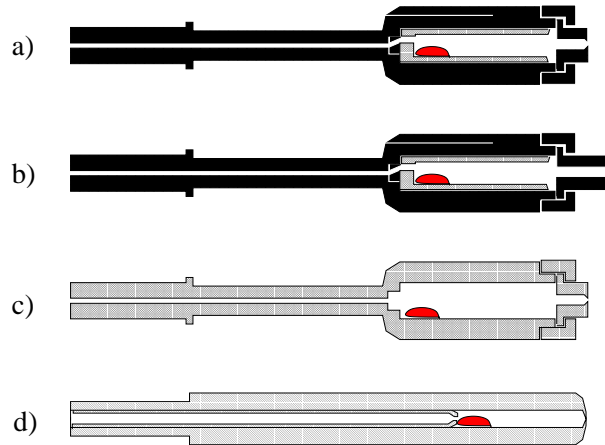


Figure 3.2: Crucibles tested for the evaporation of different metallic elements. a) high density graphite crucible with BN insert and threaded nozzle assembly with short nozzle, b) high density graphite crucible with BN insert and longer nozzle, c) BN crucible and nozzle assembly, d) Al_2O_3 crucible with fixed nozzle on outside tube. The inside tube prohibits back diffusion of metal atoms.

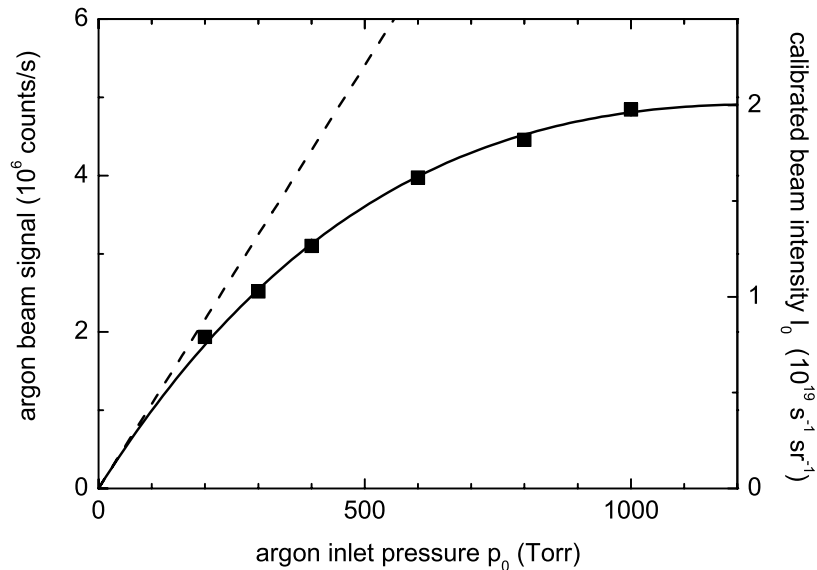


Figure 3.3: Calibration of the argon beam intensity I_0 . The ideal beam intensity (dashed line) is linear with the inlet pressure and can be calculated using Eq. (3.2), whereas the disturbed beam intensity as measured is lower by a factor $\exp(-qp_0)$. Absolute values for the Ar beam intensity can be obtained by fitting the measured data with Eq. (3.7). Nozzle temperature is 1930K.

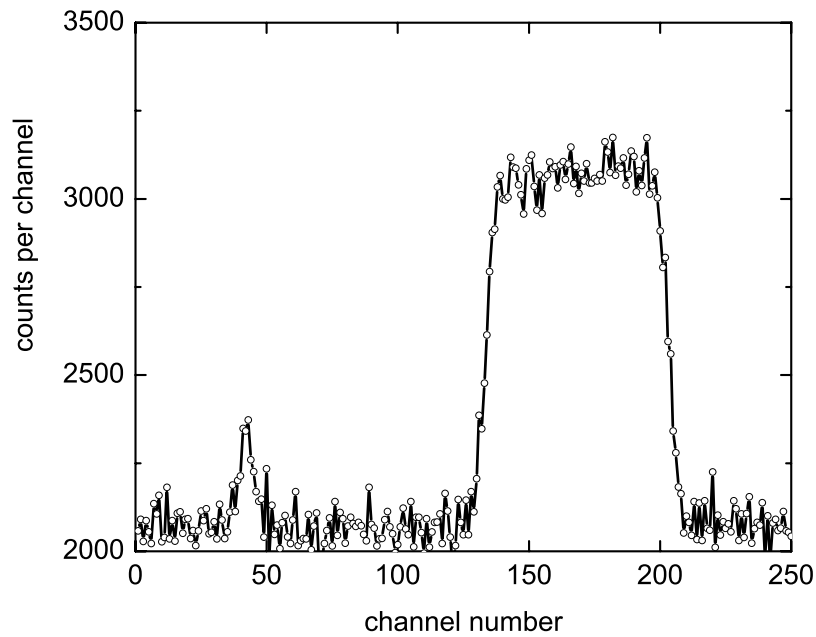


Figure 3.4: Measured time-of-flight distribution of Fe atoms at $T_0 = 1930$ K and $p_0 = 800$ Torr. The small peak gives the flow velocity and speed ratio of the Fe beam when fitting with Eq. 3.12. The large peak gives the Fe beam intensity. The distribution is obtained by a summation of 60,000 TOF-sweeps collected in a multiscaler with a channel time of $20 \mu\text{s}$.

has two narrow slits of 1 mm for the time-of-flight measurements and two wide slits of 39 mm which transmit the full beam. The chopper gate time of the small slit is much shorter than the average time the atoms need to reach the detector. This way the measured time-of-flight signal directly reflects the velocity distribution of the beam. For a density sensitive detector such as the ionization detector of the mass spectrometer, this signal is

$$N(t) \propto t^{-4} \exp \left[-S^2 \left(\frac{L}{ut} - 1 \right)^2 \right]. \quad (3.12)$$

The flow velocity u and speed ratio S can be determined by fitting the measured time-of-flight distribution with Eq. (3.12). The nozzle temperature follows from the flow velocity u by Eq. (3.4). Figure 3.4 shows an example of a time-of-flight distribution of Fe. The distribution is obtained by a summation of 60,000 TOF-sweeps collected in 250 channels of a multiscaler with a channel time of $20 \mu\text{s}$. The small peak in the distribution can be fitted to Eq. (3.12) to obtain the flow velocity and speed ratio. The large peak is the full beam signal transmitted by the wide slits of the chopper. In this measurement the full Fe beam signal is 830 counts/s. Properties of the time-of-flight setup are listed in Table I.

Table I: Properties of the experimental setup and typical Fe/Ar beam properties.

supersonic source		
operating temperature	T_0	300 - 2300 K
Ar inlet pressure	p_0	100 - 1200 Torr
flow rate	\dot{N}	$10^{19} - 10^{20} \text{ s}^{-1}$
nozzle diameter	d	0.2 - 0.25 mm
skimmer diameter		0.5 - 0.8 mm
nozzle - skimmer distance		10 - 15 mm
beam attenuation parameter	q	$8.6 \times 10^{-4} \text{ Torr}^{-1}$
typical beam properties		
source temperature	T_0	1930 K
Ar inlet pressure	p_0	800 Torr
Fe vapor pressure	p_v	0.1 Torr
Ar beam intensity	$I_{0,Ar}$	$2 \times 10^{19} \text{ s}^{-1} \text{ sr}^{-1}$
Fe beam intensity	$I_{0,Fe}$	$3 \times 10^{15} \text{ s}^{-1} \text{ sr}^{-1}$
Ar speed ratio	S_{Ar}	11
Fe speed ratio	S_{Fe}	11
virtual source radius	R_v	0.25 mm
beam divergence	R_v/z ($z = 1 \text{ m}$)	0.25 mrad
time-of-flight setup		
flight path	L	1265 mm
beam chopper diameter		90 mm
slit #1 width		1.0 mm
slit #2 width		39 mm
chopping frequency		200 Hz

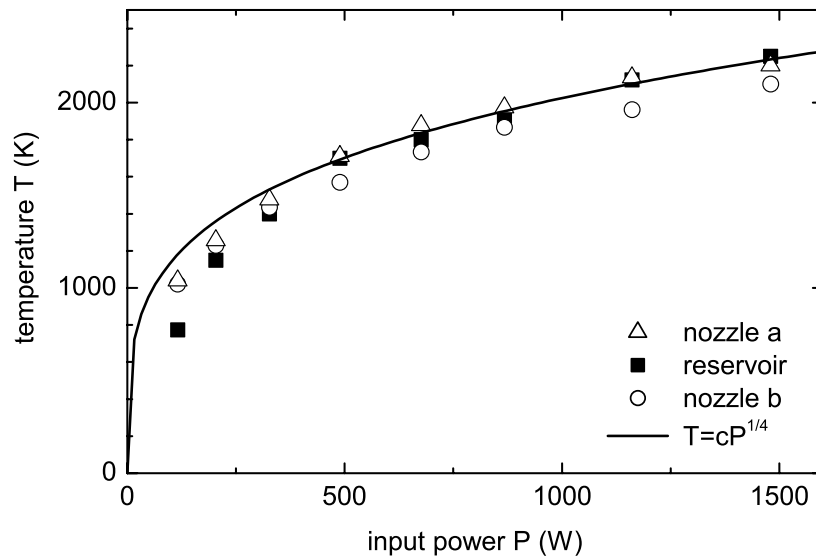


Figure 3.5: Reservoir and nozzle temperature T at increasing input power P . Reservoir temperatures have been measured with a thermocouple. Nozzle temperatures have been measured by time-of-flight analysis. The shorter, recessed nozzle (a) is significantly hotter than the longer nozzle (b), with temperatures exceeding the reservoir temperature, thus preventing nozzle clogging. The solid line gives the radiative heating loss dependence $T \propto P^{1/4}$ and shows that at high temperatures radiative heating loss is dominant. Losses due to thermal conductivity, which scale as $T \propto P$, are more important at low temperatures.

5 Results

Figure 3.5 shows the results of DC heating of the source. Due to the careful radiation shielding, temperatures up to 2200 K can be reached at relatively low input powers of less than 1500 W. Figure 3.5 shows three temperature curves. One curve has been measured by a thermocouple inserted in the graphite crucible wall. This is a measure of the reservoir temperature and therefore the temperature of the metal vapor. Temperature stability is within 25 K. The reproducibility is within 25 K over the last two years.

The other two curves in Fig. 3.5 represent the nozzle temperature as measured with time-of-flight analysis of the Ar beam. Two different nozzle assemblies as shown in Fig. 3.2(a) and 3.2(b) have been compared: nozzle (a) is recessed 10 mm more into the heating coil than nozzle (b) to obtain a higher nozzle temperature. This effect can clearly be seen. Pushing the nozzle even further into the oven leads to a disturbance of the Ar expansion cloud and would reduce the beam intensity dramatically. It can also be seen that nozzle (a) is hotter than the reservoir temperature as a result of the thinner last winding of the graphite heating coil. Nozzle clogging does therefore not occur.

To demonstrate the performance of the source for different metals, Fe and Sn have been put into the Al_2O_3 crucible simultaneously. The center line beam intensities of Ar, Fe and Sn at an

oven temperature of 1930 K are shown in Fig. 3.6. It can be seen that the Ar beam intensity increases with increasing Ar inlet pressure p_0 , but starts to saturate due to the exponential decay factor caused by beam attenuation at the skimmer. This causes the beam intensities of Fe and Sn to decrease exponentially. However, still more than 50% of the undisturbed intensity is left at 1000 Torr inlet pressure. Calculating the exponential decay rates of Fe and Sn gives slightly different rates, as predicted by Eq. (3.11). Table II shows the results of the exponential beam attenuation of Ar, Fe and Sn, as measured in Fig. 3.6.

Table II: Measured beam attenuation $\exp(-q'p_0)$ of the Ar, Fe and Sn beam due to collisions at the skimmer tip.

$q = 8.6 \times 10^{-4} \text{ Torr}^{-1}$	q'/q (Eq. (3.11))	q'/q (Fig. 3.6)
Ar	1	1
Fe	1.35	1.33 ± 0.15
Sn	1.38	1.39 ± 0.1

The absolute values of the beam intensities of Fe and Sn are calculated in two ways: first by multiplying calibrated Ar intensities with the ratio of the detector beam signals of Fe and Sn to Ar. This approach naively assumes that the sensitivity of the detector is the same for all three species. A second and better estimate is to use Eq. (3.10). However, both estimates seem to result in a very good agreement for Sn and in a reasonable agreement (within a factor of 2) for Fe. Evidently, Fe beam intensities exceeding $10^{15} \text{ s}^{-1} \text{ sr}^{-1}$ can very well be achieved.

Increasing the oven temperature by 200 K results in a 10 fold increase of the beam intensities of Fe and Sn. However, a more intensive maintenance of the skimmer after approximately every 8 hours of operation is then necessary due to a very high deposition rate of Sn onto the skimmer tip. With only Fe in the crucible, the latter problem should not exist and Fe fluxes well exceeding 10^{16} could be achieved for long periods without maintenance.

The speed ratios of the Ar, Fe and Sn atoms have also been measured. Figure 3.7 shows the result of a measurement of a supersonic expansion at a nozzle temperature of 1930 K. The oven temperature has been determined together with the speed ratios by fitting the time of flight spectra with Eq. (3.12). It can be seen that the speed ratios increase with increasing Ar pressure to values well above 10 for Ar, Fe and Sn. The difference between Ar, Fe and Sn speed ratios is hardly discernable. From Eq. (3.9) it is to be expected that the Fe speed ratios should be the same as the Ar speed ratios, but the Sn speed ratios should be approximately 25% higher. However, the last aspect is not confirmed experimentally. The accuracy of these measurements is determined by the signal to noise ratio of the TOF data. This ratio is highest for argon, and lowest for Fe, in which case a signal to noise ratio of around 3 has been measured. As a result, the uncertainty in the speed ratio is approximately 10%. The speed ratio of Ar and Sn have been determined within 5% and 7% accuracy.

A more detailed series of measurement of speed ratios of Ar is shown in Fig. 3.8. In these measurements the speed ratio of Ar has been determined at various nozzle temperatures in the range of 1200 to 2200 K. A good agreement with published values [16] represented by Eqs. (3.5) and (3.6) can be observed.

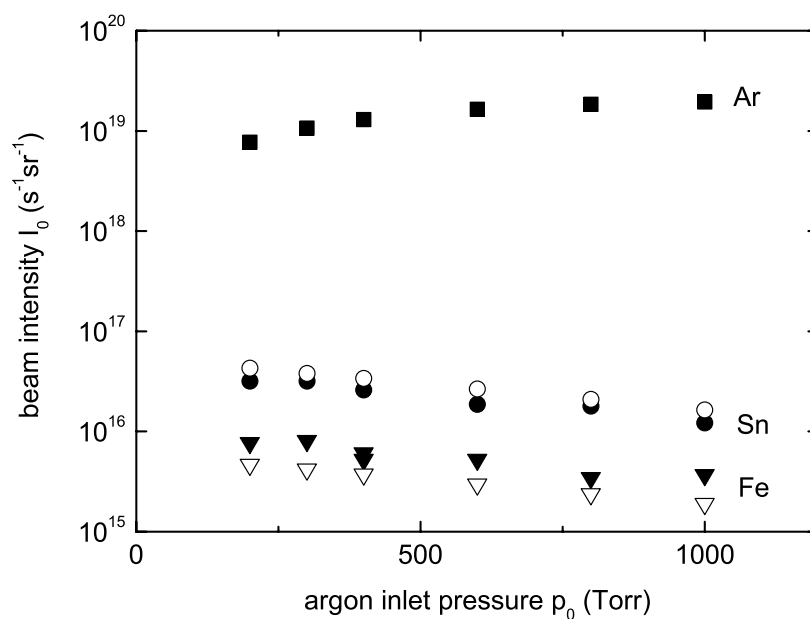


Figure 3.6: Center line beam intensities I_0 of Ar, Fe and Sn at a nozzle temperature of 1930 K. Ar beam intensities are calculated using Eq. (3.7), the Fe and Sn beam intensities (closed symbols) are calculated by multiplying the Ar beam intensity with the ratio of the count rates of Fe or Sn to Ar. Open symbols represent more accurate values of the Fe and Sn beam intensities calculated by Eq. (3.11), using known values for the vapor pressure at 1930 K.

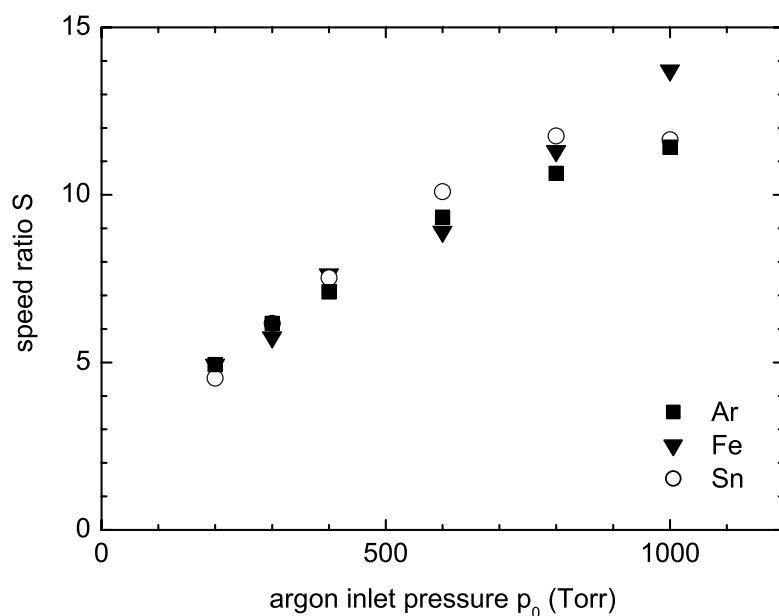


Figure 3.7: Speed ratio S of Ar, Fe and Sn measured by TOF as a function of the inlet pressure p_0 at a nozzle temperature of 1930 K.

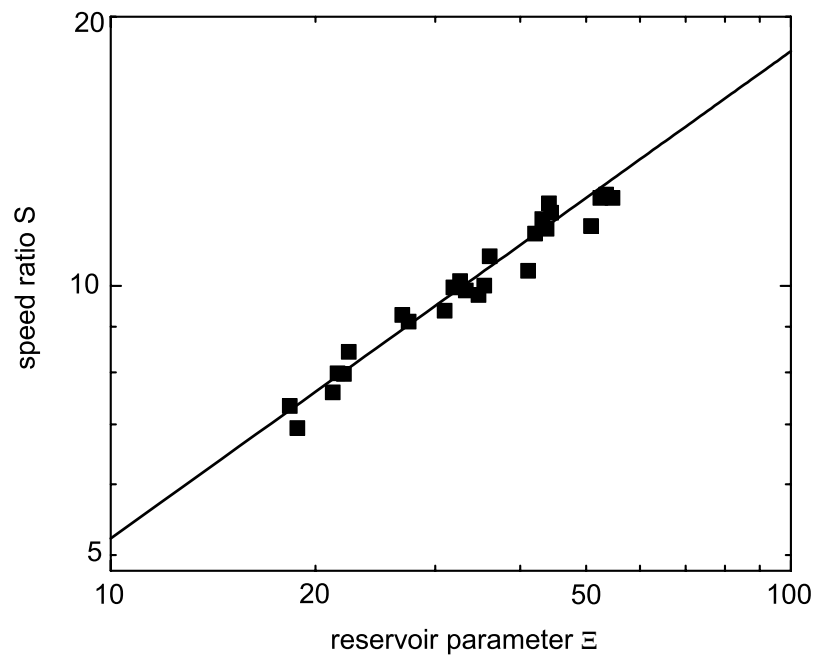


Figure 3.8: Log-log plot of Ar speed ratios measured by TOF as a function of the reservoir parameter Ξ . The solid line represents published values represented by Eq. (3.5).

6 Conclusions

The presented high temperature evaporation source shows excellent performance for the generation of a supersonic Fe beam. Care has to be taken in the choice of the crucible materials to prevent difficulties with the reactive Fe atoms. The alumina crucible seems to suffer least from this restriction. The design allows metal to be reloaded many times without damaging the crucible.

The properties of the Fe beam at a nozzle temperature of 1930 K have been determined. Beam intensities up to $5 \times 10^{15} \text{ s}^{-1} \text{ sr}^{-1}$ can be achieved. Increasing the temperature by 200 K will increase the beam intensity by a factor of 10.

Increasing the argon inlet pressure to 1000 Torr leads to a skimmer transmission still above 50%, thus not reducing the Fe beam intensity dramatically. At these higher pressures the beam monochromaticity is excellent, resulting in speed ratios well above 10. Speed ratios for argon are in agreement with earlier published values. Speed ratios for Fe are the same, as predicted theoretically.

Since a well defined Fe beam with controllable beam properties can be achieved, the presented supersonic Fe source shows great promise for future fabrication of nanomagnetic Fe structures.

References

- [1] S.J.H.Petra, L.Feenstra, W.Vassen and W.Hogervorst, International Quantum Electronics Conference CLEO/Europe-IQEC 2000
- [2] B. Brezger, Th. Schulze, U. Drodofsky, J. Stuhler, S. Nowak, T. Pfau, and J. Mlynek, *J. Vac. Sci. Technol.* **B15**, 2905 (1997)
- [3] P. Engels, S. Salewski, H. Levsen, K. Sengstock, and W. Ertmer, *Appl. Phys. B* **69**, 407 (1999)
- [4] K.K. Berggren, A. Bard, J.L. Wilbur, J.D. Gillaspay, A.G. Helg, J.J. McClelland, S.L. Rolston, W.D. Phillips, M.Prentiss, and G.M. Whitesides, *Science* **269**, 1255 (1995)
- [5] F. Lison, H.J. Adams, P. Schuh, D. Haubrich, and D. Meschede, *Appl. Phys. B* **65**, 419 (1997)
- [6] G. Timp, R.E. Behringer, D.M. Tennant, and J.E. Cunningham, *Phys. Rev. Lett.* **69**, 1636 (1992)
- [7] J.J. McClelland, R.E. Scholten, E.C. Palm, and R.J. Celotta, *Science* **262**, 877 (1993)
- [8] R.W. McGowan, D. Giltner, and Siu Au Lee, *Opt. Lett.* **20**, 2535 (1995)
- [9] F.J. Himpfel, J.E. Ortega, G.J. Mankey, and R.F. Willis, *Adv. Phys.* **47**, 511 (1998)
- [10] M.D. Hoogerland, J.P.J. Driessen, E.J.D. Vredenburg, H.J.L. Megens, M.P. Schuwer, H.C.W. Beijerinck, and K.A.H van Leeuwen, *Appl. Phys. B* **62**, 323 (1996)
- [11] H.C.W. Beijerinck, and N.F. Verster, *Physica* **111C**, 327 (1981)
- [12] R.C.M. Bosch, *Vacuum Solutions*, 17, March/April 2000
- [13] O.F. Hagen, *Z. Phys. D* **20**, 425 (1991)

-
- [14] J.B. Anderson, molecular beams and low density gas dynamics, ed. P.P. Wegener (Dekker, New York), 1 (1974)
- [15] R. Campargue, Rev. Sci. Instr. **35**, 111 (1964)
- [16] H.C.W. Beijerinck, R.J.F. van Gerwen, E.R.T. Kerstel, J.F.M. Martens, E.J.M. van Vliembergen, M.R.Th. Smits, and G.H. Kaashoek, Chemical Physics **96**, 153 (1985)
- [17] D.R. Miller, and R. Andres, Rarefied Gas Dynamics, Proc. VI symp. **2**, Academic Press New York, 1385 (1969)
- [18] O.F. Hagen, G. Knop, R. Fromknecht, and G. Linker, J. Vac. Sci. Technol. A **12**, 282 (1994)

Chapter 4

UV laser system

1 Introduction

Laser manipulation of Fe atoms requires a laser wavelength corresponding to the atomic Fe transition ${}^5D_4 \rightarrow {}^5F_5$. This wavelength is equal to 372 nm, which is in the near-UV region. Two stages of laser manipulation are used for the focusing of Fe atoms. First, Fe atoms have to be collimated to beam collimation angles on the order of 100 μrad . This is done by transverse Doppler cooling which is described in Chapter 6. Secondly, the collimated Fe beam is focused by a standing light wave onto a substrate. Both stages of laser manipulation put some further requirements on the specifications of the laser system:

- output power of 150 - 500 mW
- frequency stabilization of $\Delta\nu/\nu < 3 \cdot 10^{-9}$

Transverse Doppler cooling requires a laser power of 50 to 100 mW. The power of the standing light wave for focusing of the Fe atoms needs to be in the range of 100 to 400 mW. The frequency $\nu = c/\lambda$ of the laser system needs to be stable to within one atomic linewidth $\Gamma = 2.58 (2\pi)$ MHz of the transition ${}^5D_4 \rightarrow {}^5F_5$, so $\Delta\nu < 2.58$ MHz .

This chapter describes the UV laser system which has been developed in order to fulfill these requirements. This system is schematically shown in Fig. 4.1. The UV laser beam at a wavelength of 372 nm is obtained by so-called second harmonic generation (SHG) of a 744 nm beam. A part of the 744 nm laser beam obtained from a titanium-sapphire (Ti:S) laser can be frequency doubled to a 372 nm beam when passing through a nonlinear crystal. The efficiency of frequency doubling is proportional to the laser beam intensity in the crystal. Therefore, the crystal is placed in a high finesse cavity, in which the power is enhanced by two orders of magnitude. This way a bright beam at 372 nm is obtained, that is used for the experiment.

A small fraction of the second harmonic beam is directed through an Fe hollow cathode discharge (HCD). This discharge generates a relatively small density of Fe atoms, which supply the reference needed to lock the doubled Ti:S laser to the atomic resonance frequency. Because of the required frequency stability on the order of 10^{-9} , Doppler free spectroscopy needs to be used. Polarization spectroscopy (PS) has been chosen because of the large sensitivity of this method. With this technique an error signal is obtained that is used as a feedback signal for the Ti:S laser. This way the Ti:S laser frequency is locked to the atomic resonance frequency.

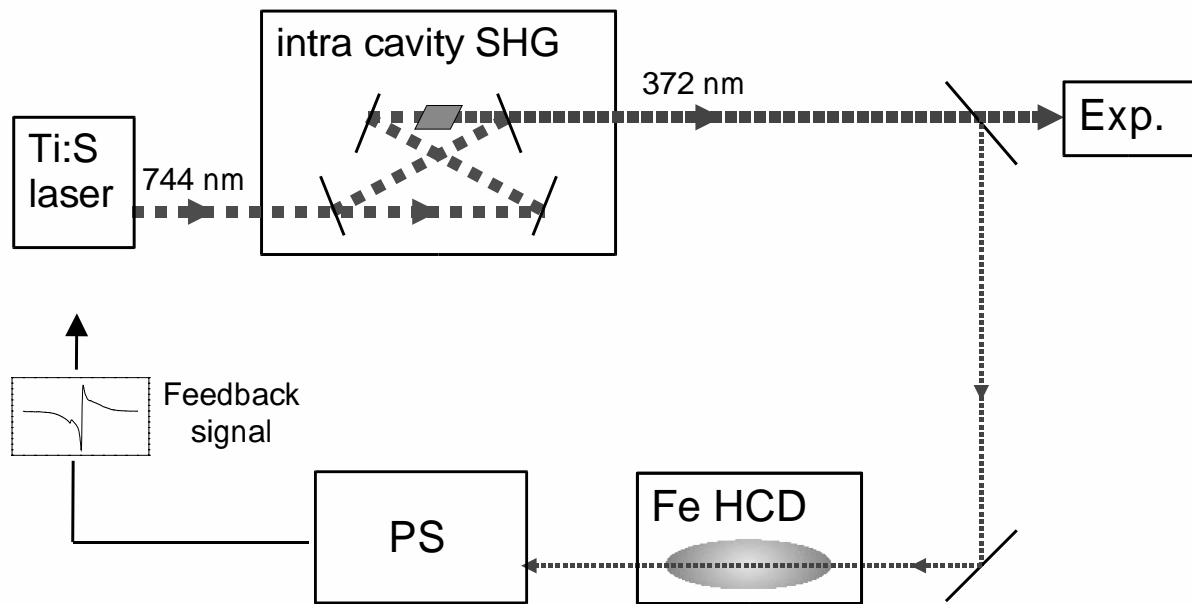


Figure 4.1: UV laser system used for the production of Fe nanostructures. A Ti:S laser produces a laser beam at a wavelength of 744 nm with a maximum power of 2 W. This beam is coupled into a high finesse cavity in which it passes through an LiB_3O_5 nonlinear crystal, which generates a second harmonic beam at 372 nm (SHG). A small fraction of the beam is directed through an Fe hollow cathode discharge (HCD), which provides a reference for the resonance frequency of the ${}^5D_4 \rightarrow {}^5F_5$ Fe transition. With polarization spectroscopy (PS) an error signal is obtained, which is used as a feedback signal to lock the Ti:S laser.

2 Second harmonic generation

General

For linear optical materials, the macroscopic polarization \mathbf{P} induced by light propagating in the medium is proportional to the electric field \mathbf{E} :

$$\mathbf{P} = \epsilon_0 \chi_1 \cdot \mathbf{E}. \quad (4.1)$$

The linearity is represented by χ_1 , which is a tensor of rank 2. The product sign in Eq. (4.1) is therefore a tensor product. The linear optical susceptibility χ_1 and the corresponding linear dielectric constant $\epsilon_1 = \epsilon_0(1 + \chi_1)$ are field-independent constants of the medium.

By using laser sources, light intensities orders of magnitude higher than what could be produced by any conventional source are now possible. As a consequence, the optical susceptibility χ of the medium becomes a function of the electric field. At strong light intensities the optical susceptibility can be expanded as

$$\chi(\mathbf{E}) = \chi_1 + \chi_2 \cdot \mathbf{E} + \dots \quad (4.2)$$

When the field-dependent term χ_2 in the optical susceptibility is not negligible, the induced macroscopic polarization in the medium contains terms that depend nonlinearly on the field:

$$\begin{aligned} \mathbf{P} &= \epsilon_0 \chi_1 \cdot \mathbf{E} + \epsilon_0 \chi_2 : \mathbf{E}^2 + \dots \\ &= \mathbf{P}^{(1)} + \mathbf{P}^{(2)} + \dots \end{aligned} \quad (4.3)$$

As the field intensity increases, the nonlinear polarization terms $\mathbf{P}^{(2)}$ become more and more important and lead to nonlinear optical effects. Specifically, when the initial electric field is given as a monochromatic light field $E e^{i\omega t}$, the tensor product $\chi_2 : \mathbf{E}^2$ of Eq. (4.3) contains terms $e^{i2\omega t}$ oscillating at the second harmonic frequency. These terms in the polarization will generate an electromagnetic wave at frequency 2ω and thus produce the frequency doubling.

SHG in an LBO crystal

The simple anharmonic oscillator model [1] shows that only materials without inversion symmetry can have a second order nonlinearity. Thus, only specific asymmetric crystals can be used for second harmonic generation. One such crystal is LiB_3O_5 (LBO), which has a large nonlinearity and good optical properties.

The components of the second order nonlinear polarization vector $\mathbf{P}^{(2)}$ can be calculated with

$$P_i^{(2)} = \sum_{j,k} \epsilon_0 \chi_{ijk}^{(2)} E_j E_k. \quad (4.4)$$

The form of the optical susceptibility tensor $\chi_{ijk}^{(2)}$ is related to the spatial symmetry of the crystal structure [2] and in general has 27 independent coefficients before any symmetry conditions are taken into account. Taking into account the permutation symmetry (i.e., the order in which E_i and E_k appear in Eq. (4.4) is not important) the number of independent coefficients reduces to

Table I: Properties of the LBO crystal.

crystal	LiB ₃ O ₅ (LBO) negative uniaxial
non-zero Kleinmann tensor elements	
d_{31}	1.05 ± 0.09 pm/V
d_{32}	-0.98 ± 0.09 pm/V
d_{33}	0.05 ± 0.06 pm/V
xy-plane phase matching (type I) phase-matching angle θ_p	$d = d_{32} \cdot \cos \theta_p$ 37.7°

18. This way $\chi_{ijk}^{(2)}$ can be expressed as a so-called 3×6 Kleinmann \mathbf{d} -tensor [3]:

$$\begin{pmatrix} P_x \\ P_y \\ P_z \end{pmatrix} = \epsilon_0 \begin{pmatrix} d_{11} & \dots & d_{16} \\ d_{21} & \dots & d_{26} \\ d_{31} & \dots & d_{36} \end{pmatrix} \begin{pmatrix} E_x^2 \\ E_y^2 \\ E_z^2 \\ 2E_y E_z \\ 2E_x E_z \\ 2E_x E_y \end{pmatrix}. \quad (4.5)$$

In an LBO crystal, the only non-vanishing terms of the Kleinmann tensor are d_{31} , d_{32} and d_{33} (Table I).

As mentioned before, with E_j a monochromatic field, Eq. (4.4) will contain terms at the second harmonic frequency that will generate frequency doubled light. However, on a microscopic scale, the nonlinear optical effect is usually rather small even at relatively high light intensity levels. In order to obtain appreciable power at the doubled frequency, the waves generated through the nonlinear material *must add coherently* on a macroscopic scale. This requires that the phase velocities of the generated wave and the incident fundamental wave are matched.

Because of the inevitable material dispersion, in general this is not the case: the fundamental and second harmonic wave will propagate at a different phase velocity. *Phase matching* requires that the refractive indices for the fundamental and second harmonic wave are equal, or $n_\omega = n_{2\omega}$. In a birefringent material the refractive index depends on the direction of the polarization of the light wave in the material. In an LBO crystal, this property is used to match the index of refraction for the fundamental and second harmonic wave, since their polarizations are orthogonal. If the fundamental wave propagates as an ordinary wave, i.e., a wave with polarization axis normal to the plane formed by the optical axis and the direction of propagation, the second harmonic wave is an extraordinary wave with polarization axis parallel to that plane (see Fig. 4.2). The optical axis is defined as the direction of propagation in which the refractive index is independent of the polarization. For the ordinary fundamental wave, the refractive index n^o is independent of the angle θ between the optical axis and the direction of propagation, whereas for the extraordinary wave the refractive index n^e is not independent of θ [4]:

$$\frac{1}{(n^e(\theta))^2} = \frac{\cos^2 \theta}{(n^o)^2} + \frac{\sin^2 \theta}{(n^e(\frac{\pi}{2}))^2}. \quad (4.6)$$

LBO is a negative uniaxial crystal which means that it has one optical axis and $n_e < n_o$. Phase-matching occurs when θ_p is chosen such that the indices of refraction for the fundamental (ordinary) beam and for the second harmonic (extraordinary) beam are the same, or $n_{2\omega}^e(\theta_p) = n_\omega^o$. There is one angle for which this is achieved. This *phase matching angle* θ_p is given by

$$\sin^2 \theta_p = \frac{(n_\omega^o)^{-2} - (n_{2\omega}^o)^{-2}}{(n_\omega^e(\frac{\pi}{2}))^{-2} - (n_\omega^o)^{-2}}. \quad (4.7)$$

For the LBO crystal the phase matching angle θ_p for the fundamental wavelength of 744 nm is equal to 37.7° (Table I).

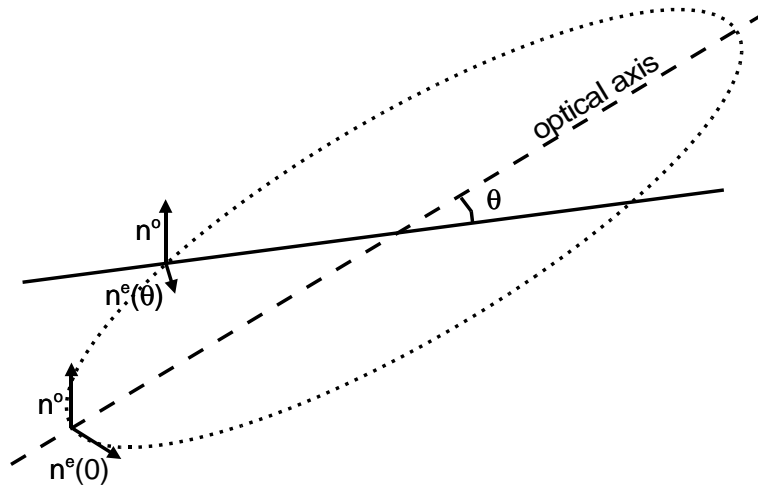


Figure 4.2: Schematic view of the relation between the refractive index of ordinary (n^o) and extraordinary (n^e) waves in a negative uniaxial crystal.

SHG power conversion efficiencies

The second harmonic beam intensity can be calculated under the small-signal approximation, i.e., a negligible fundamental wave depletion in the medium due to second harmonic generation. The beam intensity $I_{2\omega}$ at the exit of the crystal ($z = L$) is given by [1]

$$I_{2\omega} = \frac{8\pi^2 d^2 I_\omega^2 L^2}{c \epsilon_0 n_\omega^2 n_{2\omega}} \cdot \text{sinc}^2 \left[\frac{L\omega}{c} (n_\omega - n_{2\omega}) \right], \quad (4.8)$$

with d a function of the appropriate element of the Kleinmann \mathbf{d} -tensor and the phase matching angle as given in Table I, L the length of the crystal and I_ω the intensity of the fundamental pump wave. Maximum intensity $I_{2\omega}$ is achieved at phase matching ($n_\omega = n_{2\omega}$). When there is no phase matching, the intensity decreases dramatically with $n_\omega - n_{2\omega}$. For example, at a small difference in the refractive indices n_ω and $n_{2\omega}$ of 0.01, the intensity drops by six orders of magnitude in an LBO crystal with a length of 10 mm.

Equation (4.8) shows that the second harmonic beam intensity under phase matched conditions is proportional to the square of the length of the medium and to the square of the fundamental beam intensity, as expected for a second order nonlinear process.

It is tempting to assume that to increase the second harmonic power conversion efficient, all that needs to be done is to focus the fundamental beam very tightly in the crystal to increase the beam intensity I_ω . However, this decreases the length of the focal region in which the intensity is high and the angle of the k -vector of the light is equal to the phase-matching angle within the tolerance. Therefore, optimum focusing is achieved when the Rayleigh range of the focal region becomes the limiting interaction length rather than the crystal length. The maximum second harmonic power $P_{2\omega}^{max}$ that can be generated in practice is [1]

$$P_{2\omega}^{max} = \left(\frac{2\pi^2}{c\epsilon_0 n_\omega^2 n_{2\omega}} \right) \left(\frac{L}{\lambda_{2\omega}^3} \right) d^2 P_\omega^2, \quad (4.9)$$

and is linear proportional to the crystal length L . For an LBO crystal this results in a second harmonic power conversion efficiency η_{SHG} at 744 nm defined by

$$P_{2\omega}^{max} = \eta_{SHG} \cdot P_\omega^2 \quad (4.10)$$

of $1.5 \cdot 10^{-4} \text{ W}^{-1}$. For example, focusing a 1 W beam at 744 nm into an LBO crystal leads to a second harmonic beam at 372 nm with a power of 0.15 mW.

Cavity enhanced SHG

Single pass SHG of a CW-laser beam through an LBO crystal cannot generate sufficient UV power for laser collimation and laser focusing of Fe atoms. Therefore, the LBO crystal has been placed in a high finesse build-up cavity, in which the power of the fundamental beam P_ω is enhanced by two orders of magnitude.

Fig. 4.3 gives a schematic presentation of the UV laser setup that has been developed to produce a bright UV beam. An Ar-ion laser (Coherent Innova 200) with a maximum power output of 20 W pumps a Ti:S laser (Coherent 899) with a maximum output of 2 W, tuned at 744 nm. The light from the Ti:S laser is coupled into a ring cavity (the SHG cavity), which consists of 4 mirrors, placed as shown in Fig. 4.3. The mirrors are transparent for UV light, thus the UV light will leave the cavity through mirror M4. The length of the cavity is 61.5 cm.

The doubling system, which includes the crystal build-up cavity and locking electronics, has been constructed at the Vrije Universiteit in Amsterdam. Table II gives detailed specifications of the SHG cavity. The calculated cavity finesse is 469, resulting in an intra-cavity power enhancement factor of 230. However, measurements indicate a lower finesse of 177, which results in a power enhancement factor of 85. These lower values are most likely caused by absorption in the LBO crystal and remaining reflections at the Brewster-cut surface of the crystal. The beam waist w_1 between mirrors 1 and 2 is 0.15 mm. This results in a second beam waist $w_2 = 25 \mu\text{m}$ at the center of the LBO crystal, which corresponds to a Rayleigh length of $\pi w_2^2/\lambda \approx 3 \text{ mm}$. Cavity mirror M2 is mounted on a piezo transducer to keep the cavity in resonance with the 744 nm beam entering the cavity. A Pound Drever Hall locking scheme [5] is used in order to obtain an error signal that is used to drive the piezo transducer. An electro optic modulator (EOM) generates side bands to the 744 nm beam at 20 MHz from the fundamental frequency.

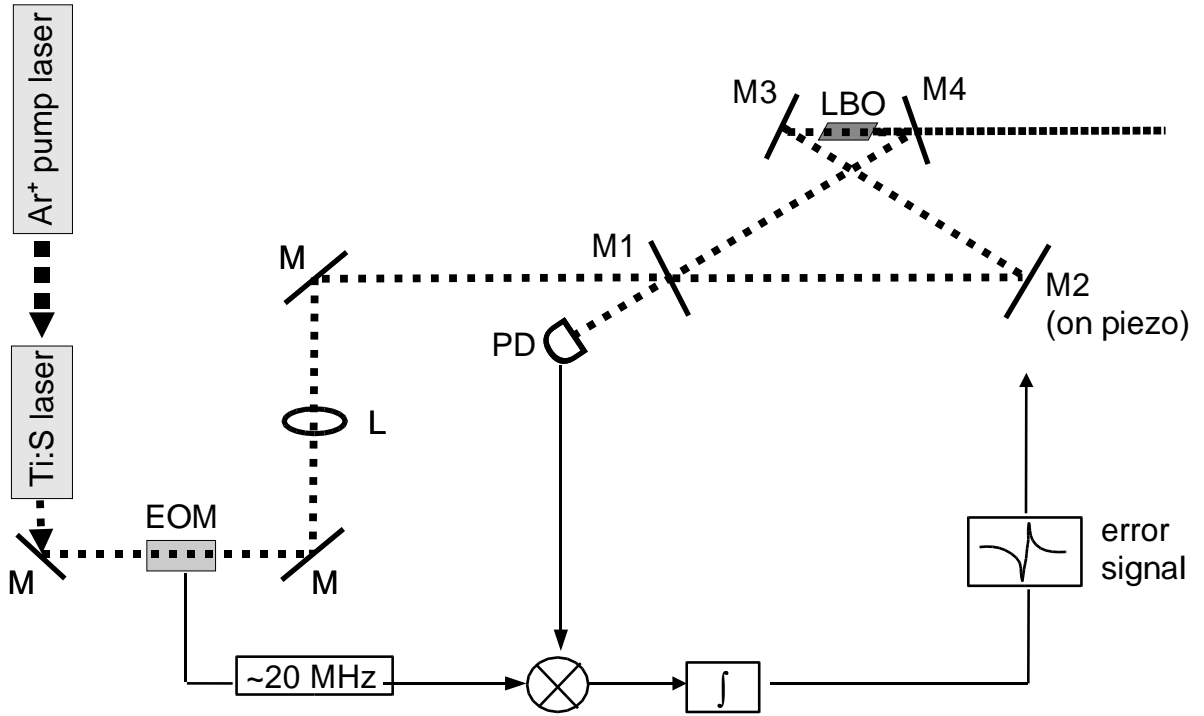


Figure 4.3: Schematic view of the frequency doubling unit. An Ar ion laser pumps a Ti:S laser, which generates light at a wavelength of 744 nm. A Brewster-cut non-linear LBO crystal is placed between the mirrors M3 and M4 of the ring cavity. Mirror M2 is mounted on a piezo transducer which is controlled using a Pound Drever Hall locking scheme to keep the cavity into resonance with the 744 nm Ti:S laser beam.

Table II: Properties of the SHG cavity.

input coupler M1	99,0%
piezo mirror M2	99,9%
curved mirror M3	99,9%, R=7.5 cm
output coupler M4	99,9%, R=7.5 cm
distance M1-M2	20.5 cm
distance M2-M3	16.5 cm
distance M3-M4	8.5 cm
distance M4-M1	16.5 cm
beam waist w_1 between M1 and M2	0.15 mm
beam waist w_2 in the LBO crystal	25 μm
free spectral range F	488 MHz
finesse \mathcal{F}	496 (calc.), 177 (measured)
intra-cavity power enhancement	230 (calc.), 85 (measured)

A fast photo diode (PD) monitors the reflection of the 744 nm beam coming from the input coupler M1. This signal is mixed and integrated with the 20 MHz oscillating frequency of the EOM, which results in an error signal for the piezo transducer [6].

Figure 4.4 shows the result of intra cavity second harmonic generation performed with the setup described in Fig. 4.3. The quadratic dependence as predicted by Eq. (4.9) is clearly visible. A quadratic fit of the data results in a power conversion efficiency of $\eta_{SHG} = 2.2 \cdot 10^{-4} \text{ W}^{-1}$. This result can be compared with the theoretical prediction of Eq. (4.9). Applying this equation to the high finesse cavity as specified in Table II gives $\eta_{SHG} = 1.2 \cdot 10^{-3} \text{ W}^{-1}$, which predict approximately 6 times more UV output power compared to the measurements. This factor can be explained by the fact that the theoretical predictions are upper limits that can be achieved, since it is assumed that over the entire Rayleigh range of 3 mm in the crystal the second harmonic conversion is optimal.

From the measurements presented in Fig. 4.4 it is clear that a sufficiently strong UV beam can be generated. Extrapolating the data to an input power of 2W into the SHG cavity would result in a UV beam of 880 mW, which is more than enough for Fe laser cooling and focusing experiments. UV powers of 600 mW have been measured but are not shown in Fig. 4.4, since the input power has not been documented. During recent measurements as shown in Fig. 4.4 the Ti:S laser was not capable of delivering more than 1200 mW. Efforts to increase this power have been done, however, not resulting in a significant improvement. The decreases in laser power is caused by deterioration of the Ar discharge tube of the pump laser.

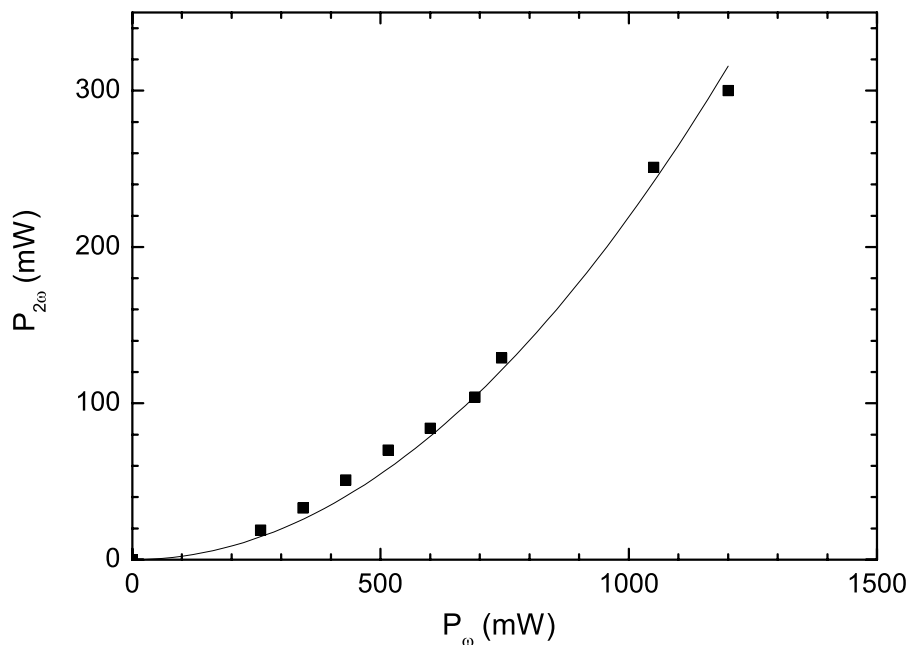


Figure 4.4: UV output power of intra cavity second harmonic generation as a function of the input power coupled in the cavity.

3 Hollow cathode discharge cell

An Fe hollow cathode discharge (HCD) cell is used to lock the laser system to the ${}^5D_4 \rightarrow {}^5F_5$ transition of the Fe atom. The HCD cell is schematically shown in Fig. 4.5. In the cell a DC discharge can be run on a variety of gases. In this case, He is used at a pressure in the range of $5 \cdot 10^{-2}$ to $5 \cdot 10^{-1}$ Torr. To prevent cell pollution the feed gas is continuously supplied and pumped away. A typical refresh rate of the total volume of the cell is once every second. The discharge runs in a 30 mm long Fe cathode with a diameter of 5 mm. Two ring shaped anodes on both sides of the grounded Fe cathode are at a DC voltage of +300 V. He^+ ions will bombard the Fe cathode, and thus sputter Fe atoms into the discharge. The properties of the Fe HCD cell are listed in Table IV.

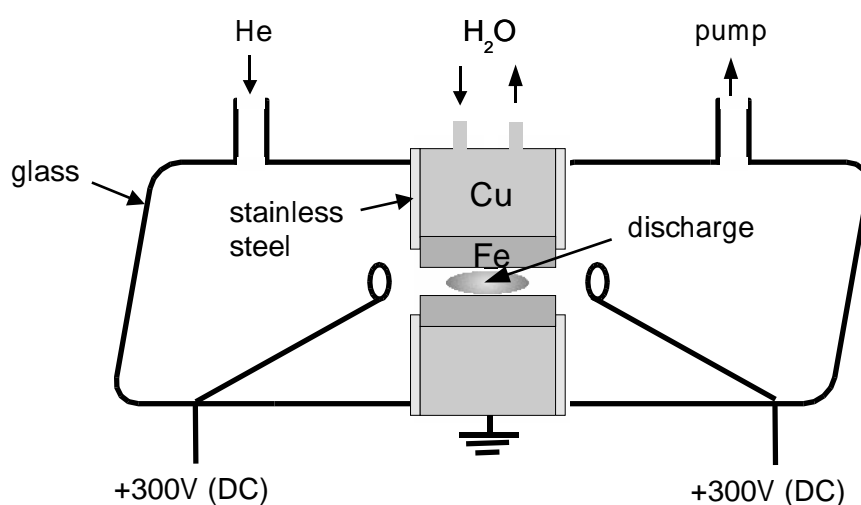


Figure 4.5: Schematic drawing of the hollow cathode discharge cell. The discharge runs from two anodes at +300V to the grounded Fe cathode. There is a continuous flow of He gas through the cell at a pressure of $5 \cdot 10^{-2}$ to $5 \cdot 10^{-1}$ mbar. The Fe cathode is mounted in a water cooled copper cylinder.

Emission spectrum of the discharge

To determine whether sufficient Fe atoms are sputtered into the discharge, the emission spectrum of the discharge has been measured. The spectrum will also contain lines of the discharge carrier gas. Table III shows the most dominant lines of He, Ne, Ar and Fe around a wavelength of 372 nm. He has been chosen as the discharge gas since Ne and Ar have some strong lines around 372.0 nm, making it difficult to distinguish the Fe lines in the emission spectrum.

The emission spectrum has been measured by focusing a part of the discharge emission into a monochromator (Jarell-Ash), containing 100 μm slits at the entrance and exit and a grating with 2340 lines/mm. This way a resolution of approximately 0.1 nm can be achieved according to the specifications. The selected light is detected by a SSR-1140B photomultiplier with an RGA photo cathode (180-590 nm). The resulting emission spectrum is shown in Fig. 4.6. The Fe lines are clearly visible. The measured resolution is approximately 0.5 nm, which is larger

Table III: The strongest atomic lines of He, Ne, Ar, and Fe around 372 nm [7].

atom	wavelength in air (nm)	relative intensity
He	370.50	3
	373.29	1
Ne	370.1	1100
	370.9	150
	371.3	250
	372.7	250
Ar	371.82	35
	372.93	70
Fe	370.56	1200
	371.99	8000
	372.26	1500

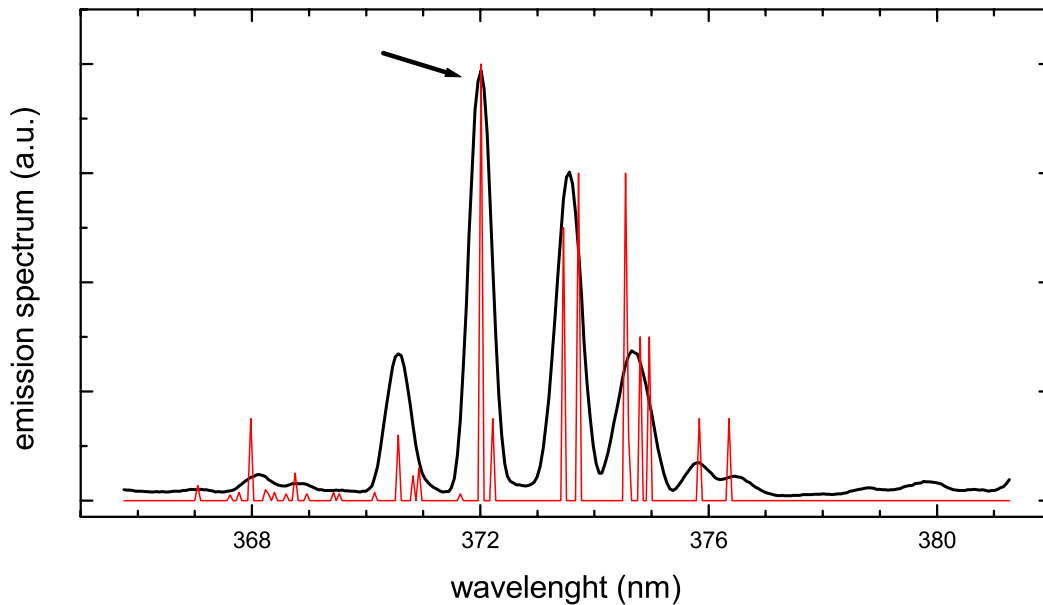


Figure 4.6: Measured emission spectrum of a He discharge running in an Fe HCD at a current of 80 mA and a pressure of $2 \cdot 10^{-1}$ mbar (solid line). Sharp lines indicate literature values of Fe lines [7]. The line at 372.0 nm indicated by the arrow corresponds to the Fe transition used for laser cooling and focusing.

than specified. The most dominant line is the $^5D_4 \rightarrow ^5F_5$ line which is used for Doppler cooling and laser focusing of Fe atoms.

Fe density and temperature determination

Figure 4.7 shows the absorption of the UV laser beam through the discharge. The laser frequency is tuned around 744.0 nm and scanned over a range of 3 GHz, which results in a UV

beam of 372.0 nm scanned over 6 GHz around the ${}^5D_4 \rightarrow {}^5F_5$ Fe line. The UV laser beam power is measured by a photodiode located behind the hollow cathode discharge cell. The measured FWHM of the absorption dip is 2.0 ± 0.05 GHz for the second harmonic frequency, which can be attributed to Doppler broadening. Theoretically the FWHM of the Doppler broadening $\Delta\nu_D$ is equal to [4]

$$\Delta\nu_D = 2\sqrt{\ln 2} \nu_0 \bar{v}/c, \quad (4.11)$$

with $\nu_0 = \omega_0/2\pi$ the resonance frequency of the ${}^5D_4 \rightarrow {}^5F_5$ transition and \bar{v} the most probable velocity of the Fe atoms. Using $\Delta\nu_D = 2.0$ GHz leads to a most probable velocity of the Fe atoms of 447 ± 11 m/s which corresponds to a discharge temperature of 673 ± 30 K.

The density of ground state Fe atoms in the discharge can be determined by the amplitude of the absorption dip. Absorption of a monochromatic beam in a medium is given by Beer's law:

$$I/I_0 = e^{-a \cdot L}, \quad (4.12)$$

with a the absorption coefficient in the medium of length L . The absorption coefficient a is given by [4]

$$a(\nu) = n \cdot (3/2\pi)\lambda^2 C^{*2} \Gamma \cdot S(\nu), \quad (4.13)$$

with $C^{*2} = 0.407$ an average over the Clebsch-Gordan coefficients due to the fact that only $\Delta m = 0$ transitions occur since the laser beam is linearly polarized. The natural atomic linewidth is represented by Γ . The function $S(\nu)$ in Eq. (4.13) represents the Doppler profile resulting from the Maxwell-Boltzmann distributions of the Fe atoms in the discharge, and is given by $S(\nu) = (0.94/\Delta\nu_D) \exp(-2.77(\nu - \nu_0)^2/\Delta\nu_D^2)$ [4].

The density of ground state Fe atoms in the discharge can be calculated using Eqs. (4.12) and (4.13) taking $I/I_0 = 0.6$ on resonance (Fig. 4.7). This gives a density of $n = 5 \cdot 10^{17} \text{ m}^{-3}$, or a ground state Fe pressure of $5 \cdot 10^{-5}$ mbar. An overview of the spectroscopy results is given in Table IV.

4 Polarization spectroscopy

In this section the technique for locking the laser to the Fe transition is explained. The partial pressure of Fe atoms in the discharge is $5 \cdot 10^{-5}$ mbar. This is a relatively low pressure, so that a sensitive spectroscopy method needs to be applied. Polarization spectroscopy (PS) is a sensitive Doppler-free method which has been applied for detection of the Fe resonance frequency. A convenient, readily accessible description of the theory of polarization spectroscopy is not easily found in literature. For this reason the theory is outlined here.

Principle of polarization spectroscopy

A linearly polarized weak probe beam and a strong circularly polarized pump beam with frequency ω pass through the discharge in opposite directions. The laser is tuned close to the atomic resonance frequency ω_0 (see Fig. 4.8).

Due to the saturation induced by the circularly polarized pump beam the magnetic sublevels of the Fe atoms in the discharge are not equally populated any more. This induces circular birefringence for the probe beam. As a result the plane of polarization of the linearly polarized

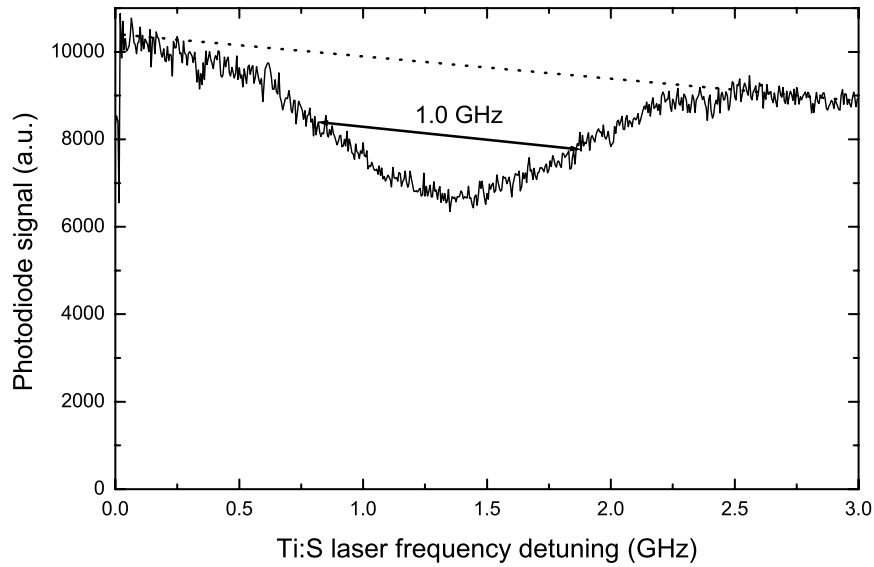


Figure 4.7: Absorption the UV laser beam by ground state Fe atoms in the hollow cathode discharge, running at 180 mA at a He pressure of $2 \cdot 10^{-1}$ mbar.

Table IV: Properties of the Fe hollow cathode discharge.

discharge	
voltage	250-300V (DC)
current	10-200 mA
volume	$\varnothing 5 \times 30 \text{ mm}^3$
He pressure	$5 \cdot 10^{-2} - 5 \cdot 10^{-1}$ mbar
refresh rate	1 cell volume/s
absorption spectroscopy	
Doppler width $\Delta\nu_D$	2.0 GHz
discharge temperature	673 ± 30 K
absorption at resonance	40%
ground state Fe density	$5 \cdot 10^{17} \text{ m}^{-3}$
ground state Fe pressure	$5 \cdot 10^{-5}$ mbar
polarization spectroscopy	
probe beam power	1 mW
pump beam power	20 mW
error signal width	40 ± 2 MHz (^{56}Fe)
	38 ± 3 MHz (^{54}Fe)
	32 ± 7 MHz (^{57}Fe)
pressure broadening	50 kHz
quadratic Stark shift	1 kHz

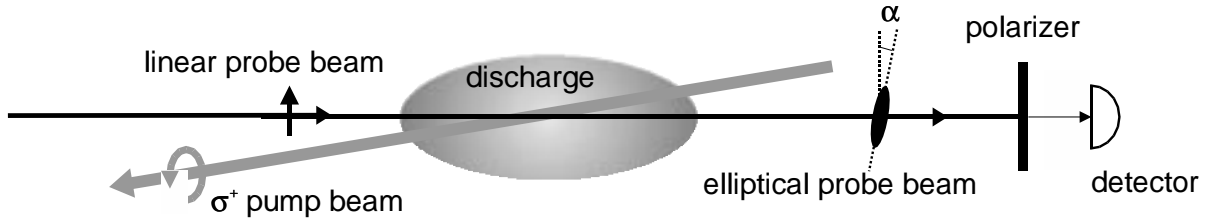


Figure 4.8: Basic setup of polarization spectroscopy. A linearly polarized probe beam and a circularly polarized pump beam pass through the sample in opposite directions. The probe beam is analyzed with a polarizer and a detector.

probe beam becomes slightly rotated. This happens only if the laser frequency ω is tuned to within the homogeneous atomic linewidth from the atomic resonance frequency ω_0 . In this case, both counter-running laser beams address the same group of atoms in the velocity distribution, namely the atoms with zero velocity in the direction of the laser beams.

We consider an incoming wave of linear polarized light in the x -direction:

$$\vec{E} = E_0 \hat{x} \exp[i(\omega t - kz)]. \quad (4.14)$$

The incoming wave can be expressed in two circular components $\vec{E} = E_+ \hat{e}_+ + E_- \hat{e}_-$, with $\hat{e}_+ = \frac{1}{\sqrt{2}}(\hat{x} + i\hat{y})$ and $\hat{e}_- = \frac{1}{\sqrt{2}}(\hat{x} - i\hat{y})$, with

$$E_+ = E_- = \frac{1}{\sqrt{2}} E_0 \exp[i(\omega t - kz)]. \quad (4.15)$$

These two components travel through the cell of length L . In the cell, the induced wavevector k_{\pm} and absorption coefficients α_{\pm} depend on the polarization. After the cell the components E_+ and E_- have changed to

$$E_{\pm} = \frac{1}{\sqrt{2}} E_0 \exp[i(\omega t - k_{\pm}L + i\alpha_{\pm}L/2)]. \quad (4.16)$$

The difference in the wavevectors is called *birefringence* and the difference in absorption *dichroism*.

It is convenient to introduce the average wavevector $k = (k_+ + k_-)/2$ and the difference $\Delta k = k_+ - k_-$. The same can be done for the absorption coefficient: $\alpha = (\alpha_+ + \alpha_-)/2$ and $\Delta\alpha = \alpha_+ - \alpha_-$. The difference Δk is caused by a difference in the index of refraction, since $k = n\omega/c$. Near an atomic resonance, the index of refraction is related to the absorption coefficient by the Kramers-Kronig relations [8]:

$$\Delta n = -\frac{1}{2} \Delta n_0 \frac{x}{1+x^2} \quad \text{and} \quad \Delta\alpha = \Delta\alpha_0 \frac{1}{1+x^2}, \quad (4.17)$$

with $x = 2\delta/\Gamma$, i.e., the ratio of the detuning δ and the atomic linewidth Γ . The relation between the change in the index of refraction and the change in absorption is given by $\Delta n_0 = -c\Delta\alpha_0/\omega$. Thus, near a resonance we can write $\Delta k = -\Delta\alpha x/2$. Due to the Kramers-Kronig relations the absorption has a Lorentzian shape and the index of refraction a dispersive shape near a resonance. After passage of the light through the cell we can write

$$E_{\pm} = \frac{1}{\sqrt{2}} E_0 e^{\mp iQ} \exp[i(\omega t - kL + i\alpha L/2)], \quad (4.18)$$

with Q defined by $Q = L\Delta k/2 - iL\Delta\alpha/4$. Using the Kramers-Kronig relations we get

$$Q = \frac{\Delta\alpha_0 L}{4} \frac{x - i}{1 + x^2}. \quad (4.19)$$

The linear components $E_{x,y}$ of the field $\vec{E} = E_x\hat{x} + E_y\hat{y}$, can be calculated to be

$$E_x = \frac{1}{2}E_0 \exp[i(\omega t - kL + i\alpha L/2)] (e^{+iQ} + e^{-iQ}), \quad (4.20)$$

$$E_y = -\frac{1}{2}iE_0 \exp[i(\omega t - kL + i\alpha L/2)] (e^{+iQ} - e^{-iQ}). \quad (4.21)$$

Note, that since for the pump beam the y component is 90° out of phase with the x component, that also the induced y component in the probe beam is 90° out of phase with the x component. Generally, Q will be small ($|Q| \ll 1$) and E_x and E_y can be approximated by

$$E_x \approx E_0 \exp[i(\omega t - kL + i\alpha L/2)], \quad (4.22)$$

$$E_y \approx E_0 Q \exp[i(\omega t - kL + i\alpha L/2)]. \quad (4.23)$$

So for small Q only the y -component depends on Q and in case $Q = 0$ the light remains linear polarized in the x -direction. The only problem that remains to be discussed is how to measure such a field in a sensitive way. In order to detect this polarization difference, we consider three cases:

- Polarizer in y -direction

The transmitted electric field is the y -component: $E_t = E_y$. For the intensity we obtain

$$I_t = \epsilon_0 c E_y E_y^* = I_0 e^{-\alpha L} |Q|^2 \quad (4.24)$$

$$= I_0 e^{-\alpha L} \left(\frac{\Delta\alpha_0 L}{4} \right)^2 \frac{1}{1 + x^2}. \quad (4.25)$$

Since $\Delta\alpha_0$ is small, the transmitted intensity will be small. The resulting lineshape will be a pure Lorentzian.

- Polarizer under an angle θ with y -direction ($\theta \ll 1$)

The transmitted electric field is given by $E_t \approx E_x\theta + E_y$, resulting in a transmitted intensity of

$$I_t = \epsilon_0 c E_t E_t^* = I_0 e^{-\alpha L} |\theta + Q|^2 \quad (4.26)$$

$$= I_0 e^{-\alpha L} \left[\theta^2 + \frac{1}{2}\Delta\alpha_0 L \theta \frac{x}{1 + x^2} + \left(\frac{\Delta\alpha_0 L}{4} \right)^2 \frac{1}{1 + x^2} \right]. \quad (4.27)$$

By choosing $\theta \gg |Q|$ but still $\theta \ll 1$, we can amplify the effects of the index of refraction, since the transmitted intensity now has a term linear in Δk . The drawback of this method is that we also introduce a constant intensity proportional with θ^2 .

- Polarizing beam splitter under 45°

Two detectors measure the intensity of the two beams exiting from the PBS. The transmitted electric field of these two beams is $E_{1,2} = \frac{1}{2}\sqrt{2}(E_x \pm E_y)$. The signal used is the

difference between the two photodiodes:

$$I_t = I_1 - I_2 = \frac{1}{2}I_0e^{-\alpha L} \left[|1 + Q|^2 - |1 - Q|^2 \right] \quad (4.28)$$

$$= \frac{1}{2}I_0e^{-\alpha L} \Delta\alpha_0L \frac{x}{1+x^2}. \quad (4.29)$$

The signal is linear in Δk and purely dispersive, thus ideal to lock the laser to resonance. The intensities measured by the two photodiodes need to be matched perfectly outside the resonance. Small imbalances can lead to a non-dispersive signal that is easily larger than the signal of (4.29).

Polarization spectroscopy is more sensitive than, e.g., saturation spectroscopy which is a more common method. The reason for this is that in the last case the signal is superimposed on the laser intensity. Therefore, fluctuations in the laser intensity will be detected directly. In case of polarization spectroscopy the signal is balanced between the two beams. The fluctuations are then due to the finite extinction ratio ξ of the polarizer. In case the polarizer is placed under an angle θ , the signal is proportional to θ and the noise is proportional to $\xi + \theta^2$. The signal-to-noise ratio becomes:

$$\frac{S}{N} \propto \frac{\theta}{\xi + \theta^2}. \quad (4.30)$$

This is optimal for $\theta = \sqrt{\xi}$ and the optimal value becomes:

$$\left(\frac{S}{N} \right)_{\max} \propto \frac{1}{\sqrt{\xi}}. \quad (4.31)$$

So compared to saturation spectroscopy the signal-to-noise ratio goes down by a factor 100–1000, since ξ is on the order of 10^{-4} – 10^{-6} for good polarizers .

Experimental Setup

The setup used for polarization spectroscopy on the hollow cathode discharge shown in Fig. 4.9. A circular polarized pump beam and a linear polarized probe beam pass through the hollow cathode in opposite directions. The probe beam is analyzed by a polarizing beam splitter cube rotated under 45° with the polarization of the probe beam. The two beams coming from the beam splitter are detected by photodiodes PD1 and PD2. The photodiode signals are subtracted. The difference signal is a dispersive signal as given by Eq. (4.29). To further reduce noise contributions, the resulting signal is analyzed by a lock-in amplifier (PAR 121), operating at 1 kHz. The 1 kHz signal is fed to an optical chopper (DigiRad C-980) which chops the pump beam at the same frequency.

Figure 4.10 shows the resulting lock-in signal that has been measured. The dispersive signal of ^{56}Fe is approximately 40 MHz wide from peak to peak. The dispersive signal is much wider than the natural linewidth of the transition, which is 2.58 MHz. A typical pressure broadening due to Fe-He collisions in the discharge is on the order of 50 kHz (Table IV). The quadratic Stark shift is on the order of 1 kHz for ground state Fe at electric fields on the order of 100 V/mm. It is clear that pressure broadening and stark shift do not explain the relatively broad error signal of 40 MHz. It is known that collisions of Fe atoms with ions and electrons in

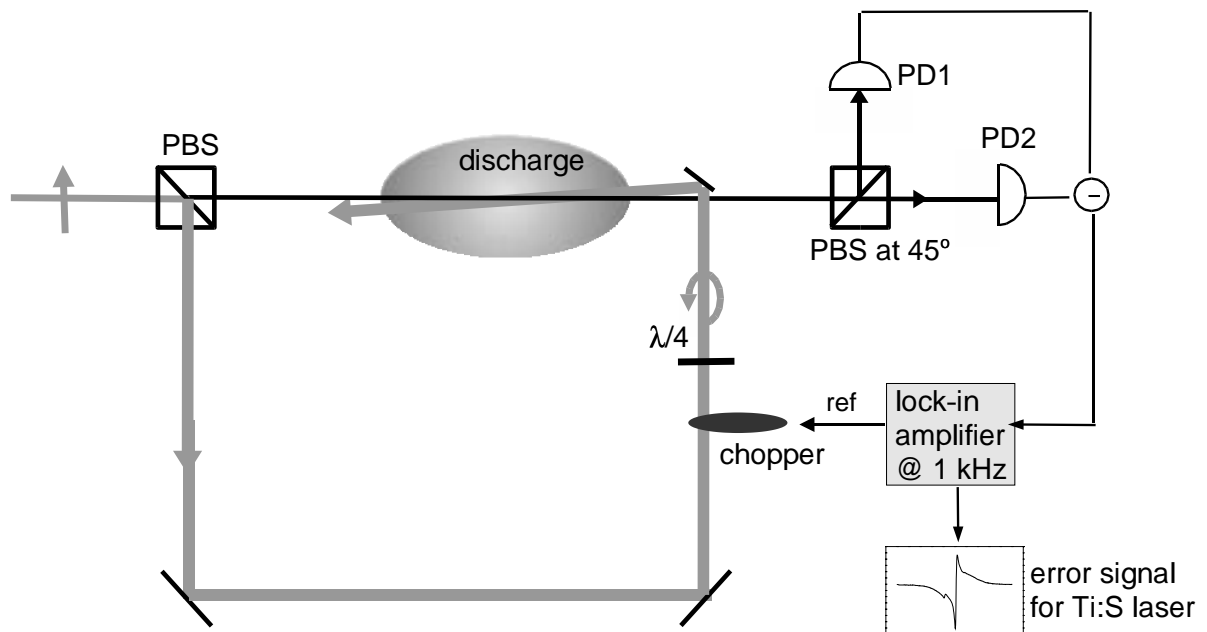


Figure 4.9: Scheme of the polarization spectroscopy setup. A linear probe and a circular pump pass through the hollow cathode in opposite directions. The probe beam is analyzed with a polarizing beam splitter under an angle of 45° . The two signals of the beams emerging from this beam splitter are subtracted and analyzed by a lock-in amplifier.

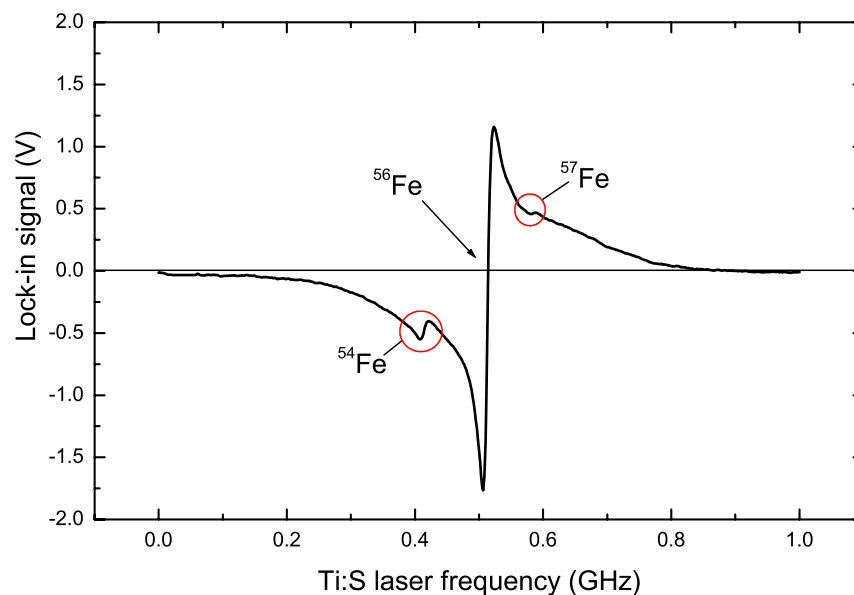


Figure 4.10: The dispersive lock-in signal, obtained from polarization spectroscopy on an Fe hollow cathode discharge. The peak-to-peak width is 40 MHz. The dispersive signals from the ^{54}Fe and ^{57}Fe isotopes are also visible.

the discharge can also contribute to the Fe line broadening. However, varying the discharge parameters does not result in a significant change in the width of the error signal. Still, the relatively large linewidth of 40 MHz is not surprising, since linewidths in a discharge below 10 MHz are rarely reported.

The error signals coming from the two other Fe isotopes (^{54}Fe and ^{57}Fe) have also been detected. These signals have a peak-to-peak width of 38 ± 3 and 32 ± 7 MHz, respectively (Table IV). The error signal of ^{56}Fe is used to lock the Ti:S laser. The estimated stability of the lock is 2 MHz, which is within one natural linewidth of the Fe transition.

5 Conclusions

A UV laser system has been developed which satisfies the requirements for further experiments on laser cooling and focusing of Fe atoms. A UV output power of 300 mW has been obtained with 1.2 W of the Ti:S laser beam coupled into the frequency doubling unit. The Ti:S laser was operating below the 2W specified power due to a defective Ar-ion pump laser. Extrapolating the measured data, over 800 mW of UV output power can be expected. The requirement of 500 mW for adequate laser cooling and focusing can thus very well be achieved.

An Fe hollow cathode discharge cell has been constructed and used for Doppler-free polarization spectroscopy. The Fe lines of the discharge spectrum have been measured successfully and the most dominant Fe lines, including the transition line used for laser cooling and focusing, have been identified. The temperature of the discharge has been determined from an absorption measurement and is approximately 670 K. From the same measurement a ground state atomic Fe density of $3 \cdot 10^{16} \text{ m}^{-3}$ in the discharge has been determined.

The UV laser frequency has been stabilized to within 2 MHz from atomic resonance using the polarization spectroscopy signal for feedback. This stability is within the Fe atomic linewidth and is therefore appropriate for laser cooling of the Fe beam.

References

- [1] C.L. Tang, *American Optical Society optics handbook* **2**, McGraw-Hill New York, 38.1 (1994)
- [2] P.A. Franken and J.F. Ward, *Rev. Mod. Phys.* **35**, 23 (1963)
- [3] A. Yariv, *Quantum Electronics*, John Wiley New York, 410 (1975)
- [4] P.W. Milonni, *Lasers*, John Wiley & Sons New York (1988)
- [5] R.W.P. Drever, J.L. Hall, F.V. Kowalski, J. Hough, G.M. Ford, A.J. Munley, and H. Ward, *Appl. Phys. B* **31**, 97 (1983)
- [6] B. Smeets, *UV laser system for the production of Fe nanostructures*, internal report, Eindhoven University of Technology (2001)
- [7] see http://physics.nist.gov/cgi-bin/AtData/main_asd
- [8] W. Demtröder, *Laser spectroscopy*, Springer-Verlag New York (1981)

Chapter 5

Laser focusing of Fe atoms

1 Introduction

This chapter describes numerical simulations of the focusing of Fe atoms using a standing light wave. Experiments on laser focusing of Cr atoms and Al atoms have led to structure sizes of 30 to 60 nm [1, 2], depending on the standing light wave properties. However, structure sizes of less than 30 nm have not yet been reported [3]. In order to be able to fabricate sub-10 nm structures of Fe, a thorough understanding of the mechanisms of laser focusing is required.

This chapter discusses three different standing light wave configurations that can be used to obtain nanometer sized structures by laser focusing:

- *thin lens regime*: atoms are being focused relatively far behind the center of the standing wave (Fig. 5.1). A typical beam waist of the standing wave is $w_z \approx 20 \mu\text{m}$, resulting in focal distances of $f \sim 20 - 100 \mu\text{m}$.
- *thick lens regime*: atoms are focused at the center of the wave. The substrate is located at the center of the standing wave and will cut off half the laser beam. Typical beam waists are $w_z \sim 50 - 500 \mu\text{m}$.
- *channeling regime*: a relatively broad standing wave ($w_z \approx 2 \text{ mm}$) is used in which the atoms are channeling towards the nodes in an increasingly steeper potential. The substrate is positioned at the center of the wave at maximum intensity.

Experiments on laser focusing of atoms using the thin lens configuration have never been reported. Channeling has been performed using metastable He atoms [4]. In all experiments so far on the deposition of nanostructures of Cr and Al [1, 3, 5, 6], the thick lens configuration is applied, with a typical beam waist $w_z = 200 \mu\text{m}$. In order to explore the possibilities of the thin lens and channeling configuration, numerical simulations have been performed on all three regimes.

Different models have been used for the calculations. The first model, which uses the steady-state dipole potential to describe laser focusing is commonly used. It can easily be used to calculate individual atomic trajectories through a standing light wave [7, 8]. The calculated sizes of Cr nanostructures have been found to be in good agreement with the size of the experimentally fabricated structures [3].

However, the effect of stimulated atomic diffusion, which can play an important role especially at high light field intensities, is not taken into account in this model. A more sophisticated model is required if stimulated diffusion is to be taken into account. This model, which is based on the *dressed atom approach* [9], is the second model that is used for the calculations. This model does not use the steady-state dipole potential. Especially in the case of laser focusing in the thin lens regime the interaction time of the atom in the standing wave can be shorter than the lifetime of the excited state. Steady-state solutions are then not valid. This way, the range of validity of the first model can be investigated.

The effect of atomic diffraction on the structure size is investigated with a third model. The atomic beam is treated as a wave packet and the process of laser focusing is calculated quantummechanically, resulting in an evolution of the atomic wave packet. The diffraction limit, which is the fundamental limit in laser focusing can be determined using this model.

Some theoretical aspects on the models that are used are given in the next section. In the remaining sections the results are presented. First the effect of the atomic beam properties is investigated. These beam properties will play a crucial role if sub-10 nm structures are to be obtained. After that, the results using the first two models are presented for the three standing wave configurations as shown in Fig. 5.1. Finally, the effect of atomic diffraction will be shown.

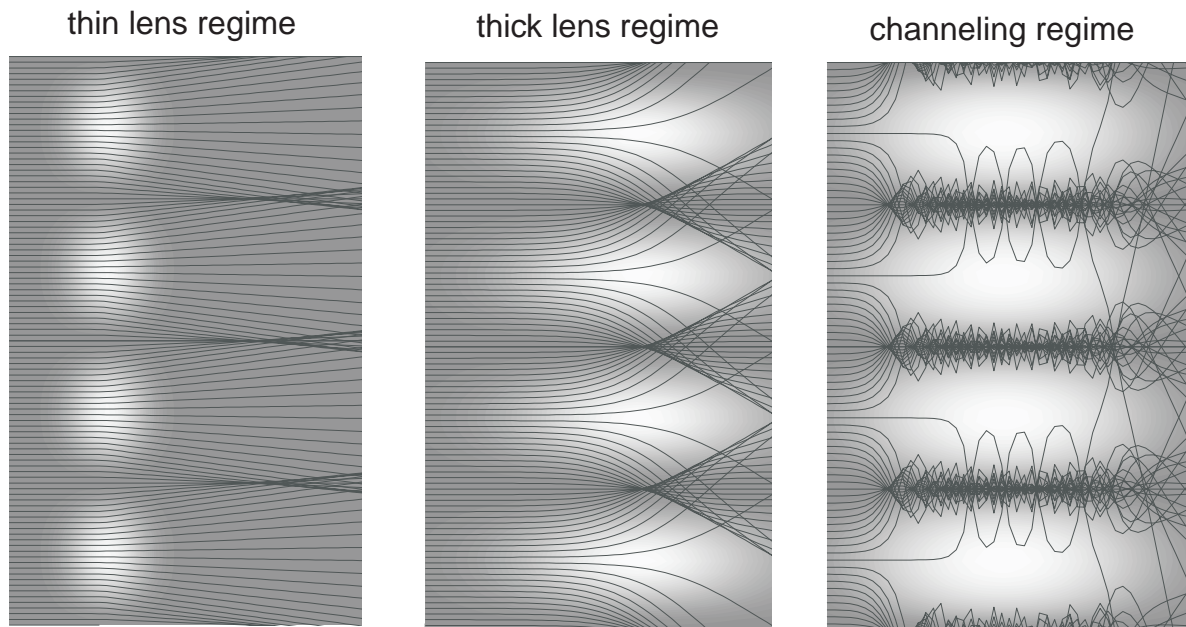


Figure 5.1: Atomic trajectory calculations on laser focusing. The atomic beam is traveling from left to right. The individual atomic trajectories are indicated by the lines. The intensity of the standing wave is shown on a grey scale, with white as a maximum intensity. Three different focusing regimes are shown: thin lens regime, thick lens regime, and channeling regime.

2 Laser focusing

2.1 Steady-state dipole potential

In general, the force felt by an atom in a light field has both velocity dependent and conservative terms. The velocity dependent terms, which arise from Doppler shifts experienced by the atom and from non-adiabatic effects, are used for laser cooling as described in Chapter 6.

For a wide range of parameters the velocity-dependent terms in the light force can be ignored, and a conservative potential can be derived. In this regime the force is referred to as the dipole force, since it can be thought of classically as the interaction of the induced atomic dipole moment with the gradient of the electric field of the light. If the laser intensity I is relatively low and the detuning δ from resonance is relatively large, such that there is not a significant population of excited state atoms, the light force potential on a two-level atom can be written as [10]

$$U_{dip} = \frac{\hbar\Gamma^2}{8\delta}s_0, \quad (5.1)$$

with Γ the decay rate of the excited state and $s_0 = I/I_s$ the saturation parameter at resonance, defined as the ratio of the light field intensity I to the saturation intensity I_s associated with the atomic transition.

For laser focusing the light field intensity can become very large, so that Eq. (5.1) can no longer be used. The effect of saturation needs to be taken into account and the dipole potential becomes [10]

$$U_{dip} = \frac{\hbar\delta}{2} \ln \left[1 + \frac{s_0}{1 + (2\delta/\Gamma)^2} \right]. \quad (5.2)$$

Equation (5.2) represents the steady-state dipole potential, which means that equilibrium between the atomic internal state and the radiation field should be maintained. This is the case if the atom moves slow enough in the spatially varying light field, or $(\vec{v} \cdot \vec{\nabla} I)/I \ll \Gamma$.

In a standing light wave the light intensity varies along the \vec{k} direction according to $I \propto \sin^2(kx)$. For a Gaussian laser beam with waists of w_y and w_z in the y and z direction respectively, the beam intensity can be written as:

$$I(x, y, z) = 4I_0 \sin^2(kx) \exp\left(-2y^2/w_y^2 - 2z^2/w_z^2\right) \quad (5.3)$$

with I_0 the centerline beam intensity of a single traveling wave given by $I_0 = 2P/(\pi w_y w_z)$ where P is the laser power. The steady-state dipole potential of a standing wave can then be expressed as

$$U_{dip} = \frac{\hbar\delta}{2} \ln \left[1 + \frac{I(x, y, z)/I_s}{1 + (2\delta/\Gamma)^2} \right]. \quad (5.4)$$

An example of some dipole potentials for Fe atoms traveling through a near resonant standing wave is shown in Fig. 5.2. Upper curves are potentials with blue detuning ($\delta > 0$), lower curves are potentials with red detuning. For the blue detuned standing waves, the minimum of the potential coincides with the nodes. Therefore the Fe atoms will be attracted to regions of low intensity. For the red detuned waves, the situation is reversed: the atoms are attracted to regions of high intensity. The effect of saturation is also clear from Fig. 5.2. At low laser power the shape of the potentials at the minima for a blue and red detuning is the same. However, at

increasing power the minima for blue detuned waves become steeper, as for the red detuned waves they become more flat. In this region the potential is getting more saturated. In the limit of small s_0 and or large δ (no saturation), where the dipole potential of Eq. (5.2) approximates to Eq. (5.1), the potential scales with $\sin^2(kx)$ and has therefore the same shape at the nodes and anti-nodes. At increasing power, the logarithm of Eq. (5.2) plays a more dominant role and breaks this symmetry.

Focusing of atoms will occur in regions close to the minima of the potential where it can be approximated by a parabolic potential: $U \propto x^2$. For a blue and red detuned standing wave the potential at the nodes and anti-nodes, respectively, can be approximated as

$$\begin{aligned} U_{dip,nodes} &\approx (\hbar\delta/2)Ak^2x^2, \\ U_{dip,anti-nodes} &\approx -(\hbar\delta/2)[Ak^2x^2/(1+A) - \ln(1+A)]. \end{aligned} \quad (5.5)$$

Note that the signs of the second order terms in Eq. 5.5 are the same, since the detuning δ has an opposite sign. The quantity A takes into account the local light field parameters and represents the saturation of the potential:

$$A = 4\frac{I_0}{I_s}(1 + (2\delta/\Gamma)^2) \exp\left(-2y^2/w_y^2 - 2z^2/w_z^2\right). \quad (5.6)$$

As can be seen, for low saturation (low laser power P or high detuning δ) the parabolic approximation becomes the same for blue and red detuned standing waves. The focal distance will scale inversely with the pre-factor of x^2 of the parabolic potential. This means that at high saturation, the focal distance for blue detuned standing waves will be much shorter than for red detuned waves. As will be shown by the simulations, a short focal distance is desired. This is one of the two reasons that blue detuned waves are more appropriate for laser focusing than red detuned waves. The second reason is that the effect of spontaneous emission, which can disturb laser focusing, is reduced when using a blue detuned standing wave. Atoms are localized near the nodes of the standing wave by which they are focused and therefore spend more time in regions of low laser intensity. When using red detuned waves the situation is reversed. Atoms spend more time in regions of high intensity, where spontaneous emission is more likely to occur.

If the standing wave is used in the thin lens regime, the focal distance is located downstream of the standing wave (see Fig. 5.1). In the limit where the focal distance f is much larger than the standing wave beam waist w_z in the direction of the atomic beam, the focal distance f for a blue detuning can be calculated analytically [7], resulting in

$$f|_{y=0} = (2/\pi)^{1/2} \frac{mv_z^2}{\hbar\delta} \cdot \frac{\pi w_y I_s}{8P} \cdot (1 + (2\delta/\Gamma)^2)k^{-2}. \quad (5.7)$$

The focal distance is in first order independent of the beam waist w_z . The atomic beam parameters are represented by the kinetic energy $\frac{1}{2}mv_z^2$, with v_z the axial velocity and m the atomic mass.

In the thick lens regime the atoms are focused to the center of the Gaussian laser beam. The beam waist w_z required to bring the atoms into focus at the center is given by [7]

$$w_z = 5.37 \cdot \frac{mv_z^2}{\hbar\delta} \cdot \frac{\pi w_y I_s}{8P} \cdot (1 + (2\delta/\Gamma)^2)k^{-2}. \quad (5.8)$$

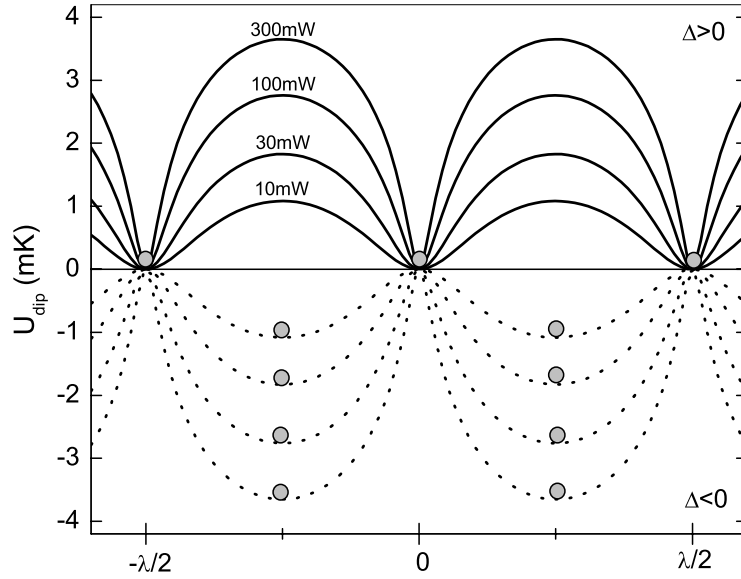


Figure 5.2: Dipole potential for Fe atoms at the centerline of a $w_y \times w_z = 200 \times 200 \mu\text{m}^2$ standing light wave. The upper curves are the dipole potentials for a blue detuning of +500 Mrad/s, the lower curves for a red detuning of -500 Mrad/s. Because of the opposite signs of the potentials, the minima are located at the nodes for blue detuning and at the anti-nodes for red detuning (indicated by the circles).

2.2 Stimulated atomic diffusion: dressed atom approach

Dalibard and Cohen-Tannoudji have introduced a new model to describe the forces on an atom in a light field [9]. This so-called *dressed atom approach* leads to some new effects occurring at high laser intensity. One of them is “stimulated enhancement” of the spontaneous-emission induced diffusive movement of atoms, which is of direct relevance for laser focusing.

We review the the dressed atom model briefly. The model treats a two-level atom and light field simultaneously. The eigenfunctions of the Schrödinger equation for a two-level atom in a monochromatic light field are best described in terms of *dressed states* of the atom. It begins with the total Hamiltonian

$$H = H_a + H_{rad} + H_{int}, \quad (5.9)$$

where H_a is the usual atomic part with eigenvalues E_g and E_e that gives the unperturbed atomic energy levels (ground and excited state), H_{rad} represents the quantized light field energy with eigenvalues $E_n = (n + \frac{1}{2})\hbar\omega_L$, and H_{int} is the atom-field interaction Hamiltonian.

The energy level diagram of the first two terms of Eq. (5.9) consists of the levels with energy $E_g + (n + \frac{1}{2})\hbar\omega_L$ and $E_e + (n + \frac{1}{2})\hbar\omega_L$, with n the number of photons in the light field. As the detuning $\delta = \omega_L - (E_e - E_g)/\hbar$ of the light field is assumed to be much smaller than ω_L , $E_g + (n + \frac{1}{2})\hbar\omega_L$ and $E_e + (n - \frac{1}{2})\hbar\omega_L$ form a closely spaced pair as shown in Fig. 5.3(a).

The third term of the Hamiltonian H_{int} couples the two states and splits the energies further apart to $\hbar\Omega_{12}$, as shown in Fig. 5.3(b). The parameter Ω_{12} is defined as

$$\Omega_{12} = \sqrt{\Omega_R^2 + \delta^2}, \quad (5.10)$$

with Ω_R the on-resonance Rabi-frequency defined by $s_0 = 2\Omega_R^2/\Gamma^2$. The mixing of the states is expressed in terms of a mixing angle θ given by $\cos(2\theta) \equiv -\delta/\Omega_{12}$. The eigenstates of the Hamiltonian of Eq. (5.9) thus do not represent pure atomic ground or excited states anymore. The combined states of the atom and the light field are called the *dressed states* of the atom.

$$\begin{aligned} |1, n\rangle &= \sin(\theta)|g\rangle + \cos(\theta)|e\rangle, \\ |2, n\rangle &= \cos(\theta)|e\rangle - \sin(\theta)|g\rangle, \end{aligned} \quad (5.11)$$

with eigenvalues given by

$$\begin{aligned} E_{1,n} &= (n+1)\hbar\omega_L - \frac{1}{2}\hbar\delta + \frac{1}{2}\hbar\Omega_{12}, \\ E_{2,n} &= (n+1)\hbar\omega_L - \frac{1}{2}\hbar\delta - \frac{1}{2}\hbar\Omega_{12}. \end{aligned} \quad (5.12)$$

Equation (5.12) reveals that the forces f_1 and f_2 on dressed state 1 and 2, respectively, are different:

$$\begin{aligned} f_1 &= -\nabla E_{1,n} = -\frac{1}{2}\hbar\nabla\Omega_{12}, \\ f_2 &= -\nabla E_{2,n} = +\frac{1}{2}\hbar\nabla\Omega_{12}. \end{aligned} \quad (5.13)$$

Evidently, the forces are opposite. Figure 5.3(c) shows how both dressed states would evolve when travelling through an increasing and decreasing light field with blue detuning. Dressed state 1 is lower in energy in regions of low intensity, dressed state 2 in regions of high intensity.

Atoms are distributed among the dressed states 1 and 2 and are allowed to change from state when *spontaneous emission* occurs. This effect is shown in Fig. 5.3(d). The transition rate Γ_{ij} describes the rate of spontaneous emission from state i to j , and can be expressed as

$$\begin{aligned} \Gamma_{12} &= \Gamma \cos^4(\theta), \\ \Gamma_{21} &= \Gamma \sin^4(\theta), \\ \Gamma_{11} &= \Gamma \cos^2(\theta) \sin^2(\theta), \\ \Gamma_{22} &= \Gamma \cos^2(\theta) \sin^2(\theta), \end{aligned} \quad (5.14)$$

with Γ^{-1} the natural life time of the excited state of the atom. In a steady state situation, the populations Π_1 and Π_2 of atoms occupying states 1 and 2, respectively, can be written as

$$\begin{aligned} \Pi_1 &= \Gamma_{21}/(\Gamma_{12} + \Gamma_{21}), \\ \Pi_2 &= \Gamma_{12}/(\Gamma_{12} + \Gamma_{21}), \end{aligned} \quad (5.15)$$

with Γ^{-1} the natural life time of the excited state of the atom. The mean force on an atom at rest, i.e. the the sum of the forces f_1 and f_2 weighted by the steady state populations Π_1 and Π_2 is

$$\langle f \rangle = \Pi_1 f_1 + \Pi_2 f_2 = -\hbar\delta \frac{\Omega_R \nabla \Omega_R}{\Omega_R^2 + 2\delta^2} = -\nabla \left[\frac{\hbar\delta}{2} \ln\left(1 + \frac{\Omega_R^2}{2\delta^2}\right) \right]. \quad (5.16)$$

As can be seen Eq. (5.16) results in the earlier expression for the steady-state dipole force in the limit $\Omega_{12} \gg \Gamma$ given by

$$\langle f \rangle = -\nabla U_{dip}, \quad (5.17)$$

with U_{dip} the steady-state dipole potential given by Eq. (5.2). In the dressed state model, atoms traveling through a standing light wave can be described as follows. Initially, when the light field intensity is zero ($\Omega_R = 0$), all the atoms are in dressed state 1, as can be checked with Eqs.

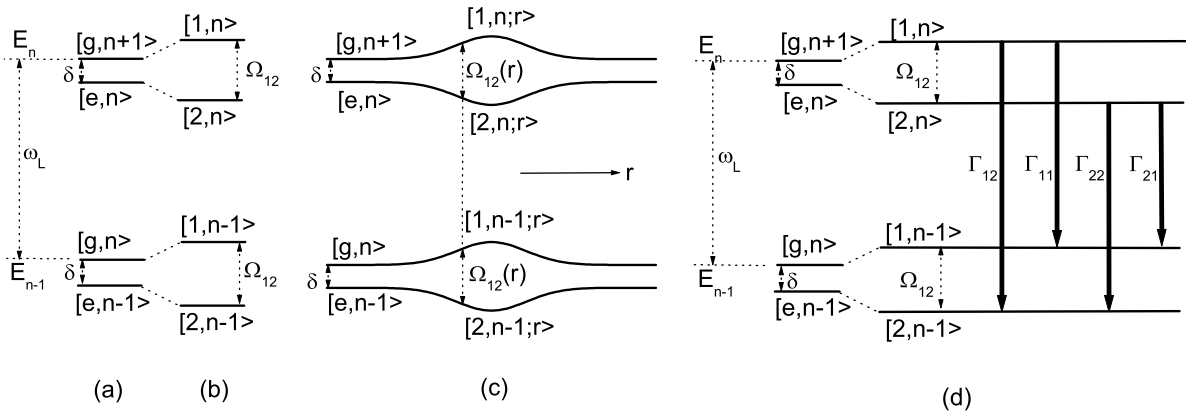


Figure 5.3: Dressed atom energy diagram for blue detuning. (a) energy states of the unperturbed Hamiltonian. The energy levels E_n are split by δ . (b) the atom field coupling results in an increased splitting of Ω_{12} of the dressed states. (c) variation of the dressed atom energy diagram across an increasing and decreasing light field. The energy splitting Ω_{12} is position dependent. (d) spontaneous emission between two, split, dressed state energy levels. There are four allowed transitions, represented by the rates Γ_{11} , Γ_{12} , Γ_{22} and Γ_{21} .

(5.14) and (5.15). The rate of spontaneous decay Γ_{12} from state 1 to 2 is zero. When the light field intensity increases, the decay rates Γ_{ij} are changing, depending on the local field intensity. As a result, the population of states 1 and 2 are changing as well. It is to be expected that the atoms spend most of the time in state 1. This is because these atoms are low field seeking and are therefore localized in regions close to the nodes. The probability Γ_{12} of decaying to state 2 is then relatively small (Eq. (5.14)). However, a crucial difference with the steady-state model results from the fact that this probability is still finite. Once they have decayed to state 2 the atoms become high field seeking and will travel towards the *anti-nodes*. In this picture, spontaneous emission does not only result in a random recoil momentum of $\hbar k$, but can also result in a change in the direction of the force according to Eq. (5.13). These spontaneous-emission induced force changes give rise to a significant diffusion in the atomic motion which does not saturate.

The effect of stimulated diffusion becomes most pronounced at high light field intensities and in the case the atoms spend enough time in the light field to have a significant number of spontaneous decays to a different dressed state. Relatively large standing waves at high intensities are used in the channeling regime, where a large deviation between the results of the two models is to be expected.

3 Calculation on focusing

Numerical simulations on Fe atoms traveling through a standing light wave have been performed in order to obtain insight in the mechanisms that play a role in laser focusing. With the simulations the following quantities have been investigated:

- location of the focal distance f , in case the standing wave is used in the thin lens regime.
- beam waist required to put the focal plane at the center of the standing wave w_z in case the standing wave is used in the thick lens regime.
- FWHM of the atomic distribution taken at the focal plane. This represents the size of the deposited nanostructures in the real experiment.
- fraction of the atoms that is focused, defined as ratio of the area of the Lorentzian shaped distribution (FWHM \times peak height) to the total area (including background)
- contrast of the same atomic distribution, which is defined as the ratio of the maximum to the minimum of the distribution.

All these quantities have been studied as a function of laser power and detuning from resonance. The Fe beam parameters that have been chosen are typical experimental parameters, which is a beam velocity $v_z = 1400$ m/s and a speed ratio $S = 10$. A typical beam collimation is $100 \mu\text{rad}$, slightly above the Doppler limit. According to the simulations presented in Chapter 6 this beam divergence should be experimentally feasible.

Steady-state model

The calculations are based on a Monte Carlo simulation of classical atomic trajectories through the standing wave. Calculations are performed in the (x,z) plane at $y = 0$, resulting in

$$U_{dip}(x, z) = U_{dip}(x, y, z)|_{y=0} \quad (5.18)$$

which means that the potential $U_{dip}(x, y, z)$ as given by Eq. (5.4) is evaluated along the center of the beam in y-plane.

Typically 10^4 trajectories are calculated, each trajectory starting with initial velocities $v_z = \langle v_z \rangle + dv_z$ and $v_x = 0 + dv_x$, where dv_z and dv_x are random velocities taken randomly from Gaussian distributions f_z and f_x , respectively, given by

$$f_z \propto \exp\left(-\frac{(v_z - \langle v_z \rangle)^2}{2\sigma_{v_z}^2}\right) \quad (5.19)$$

$$f_x \propto \exp\left(-\frac{v_x^2}{2\sigma_{v_x}^2}\right). \quad (5.20)$$

The widths of these distributions σ_{v_z} and σ_{v_x} are given as input parameters and represent the speed ratio and collimation of the Fe beam. A histogram of the atomic positions at the focal plane determines the atomic distribution. The atomic trajectories can be calculated by solving

$$\frac{\delta^2 x}{\delta t^2} + \frac{1}{m} \frac{\delta U}{\delta x} = 0 \quad (5.21)$$

$$\frac{\delta^2 z}{\delta t^2} + \frac{1}{m} \frac{\delta U}{\delta z} = 0 \quad (5.22)$$

Table I: Input parameters of the simulation programs.

P δ	power and detuning
w_z, w_y, z_0	beam waists and location
$\langle v_z \rangle, dv_z, dv_x$	Fe beam properties

with the potential U as given by Eq. (5.4) for a standing wave. Discretizing these equations using time intervals of Δt leads to the difference equations

$$x_{n+1} - 2x_n - x_{n-1} = -\frac{(\Delta t)^2}{m} \frac{\delta U}{\delta x}(x_n, z_n) \quad (5.23)$$

$$z_{n+1} - 2z_n - z_{n-1} = -\frac{(\Delta t)^2}{m} \frac{\delta U}{\delta z}(x_n, z_n), \quad (5.24)$$

which can be used for the numerical integration of Eqs. (5.21) and (5.22). The initial values x_0, z_0, x_1 and z_1 are taken from the boundary conditions on the atomic trajectories, given by the position (x_0, z_0) and initial velocity (v_x, v_z) . The program is written in FORTRAN/77, using NAG library routines for (Gaussian) random number generation. A simulation of 10^4 atomic trajectories takes approximately 30 s on a PIII/600 computer. Table I shows the input parameters of the simulation program. Note that the focal distance is given as input parameter. This value needs to be determined from the output file containing the atomic trajectories, which is generated with a previous simulation.

Dressed atom model

For numerical implementation of the dressed atom model, the same concept is used as in the previous model. In addition each atom is labeled to one of the two dressed states, starting with dressed state 1 outside the light field. Obviously, the steady-state force as given by the gradient of the steady-state potential in Eq. (5.21) needs to be replaced by the dressed state according to Eq. (5.13). The sign of the force is determined by the dressed state. During each time step Δt , the probabilities $\Gamma_{ij}(x, z, t) \cdot \Delta t$ of a decay from state i to state j are considered. The local decay rates $\Gamma_{ij}(x, z, t)$ are given by Eq. (5.14).

Quantum mechanical model

In order to investigate the effect of atomic diffraction, the wave nature associated with the center-of-mass motion of the atoms needs to be taken into account. The atomic wave function is defined as [11]

$$|\Psi(x, t)\rangle = \sum_{i=g,e} |i\rangle \psi_i(x, t), \quad (5.25)$$

in which $\psi_i(x, t)$ denotes the spatial wave function for internal state $|i\rangle$. Since the interaction between the atoms and the standing light field is given by a spatially periodic Hamiltonian $\propto \sin(kx)$ and the incoming atomic deBroglie wave can be approximated by a plane wave, the

spatial wave function $\psi_i(x, t)$ can be assumed periodic. Therefore $\psi_i(x, t)$ is expanded in a Fourier series:

$$\psi_i(x, t) = \sum_n \phi_{i,n}(t) \exp(i(n + \Delta n)kx). \quad (5.26)$$

This equation represents an expansion in atomic motional states with momentum $(n + \Delta n)\hbar k$. Initially, only the $n = 0$ coefficient $\phi_{i,0}$ is nonzero. The initial momentum $\Delta n\hbar k$ represents the angle between the standing wave and the atomic beam. For $\Delta n = 0$ the atomic beam and standing wave are orthogonal. The finite atomic beam collimation can then be represented by performing a series of calculations for different values of Δn .

The master equation that needs to be solved is the time-dependent Schrödinger equation for $|\Psi(x, t)\rangle$ with the following Hamiltonian [11]

$$H = -\frac{\hbar^2}{2m} \frac{\partial^2}{\partial x^2} - \hbar\delta|e\rangle\langle e| + \hbar\Omega_R (|e\rangle\langle g| + |g\rangle\langle e|) \cos(kx), \quad (5.27)$$

with δ the laser detuning and Ω_R the on-resonance Rabi frequency. The following set of coupled differential equations can be derived:

$$\begin{aligned} \frac{d}{dt}\phi_{g,n}(t) &= -i[(n + \Delta n)^2\omega_{rec}]\phi_{g,n} - i\frac{\Omega(t)}{2} (\phi_{e,n-1}(t) + \phi_{e,n+1}(t)), \\ \frac{d}{dt}\phi_{e,n}(t) &= -i[(n + \Delta n)^2\omega_{rec} - \delta]\phi_{e,n} - i\frac{\Omega(t)}{2} (\phi_{g,n-1}(t) + \phi_{g,n+1}(t)) - \Gamma/2\phi_{e,n}(t), \end{aligned} \quad (5.28)$$

with $\omega_{rec} = \hbar k^2/2m$ the recoil frequency. The last term on the right hand side of Eq. (5.28) is an artificial damping term which represents the probability of spontaneous emission [12]. Equations (5.28) are implemented in a FORTRAN/77 program and solved numerically for 256 Fourier components for the ground state and another 256 components for the excited state. The NAG FORTRAN library is used for integration and FFT routines. One simulation takes approximately one hour on a PIII/600 computer.

4 Numerical results

4.1 Effect of atomic beam properties and beam masking

Background-free structures of Fe will ultimately be fabricated using a standing light wave with a mechanical grating. The size of the structures will strongly depend on the Fe beam parameters, i.e., beam divergence and speed ratio.

The effect of beam divergence can simply be estimated by a broadening of the structures which is directly proportional to the transverse velocity spread dv_x and the focal distance f as $2b \approx 2dv_x \cdot f$, with $2b$ a typical contribution to the FWHM of the structures. Therefore it is clear that short focal distances will have to be chosen in order to reduce the effect of the final beam collimation after laser cooling of the Fe beam.

Experiments with deposition of atoms by laser focusing have been performed by using the standing light wave as a thick lens of typically $400 \times 400 \mu\text{m}^2$ [1, 2]. As will be shown, this results in a relatively large focal distance of typically $200 \mu\text{m}$. For a beam collimation of $100 \mu\text{rad}$, this results in a minimum structure size of around 40 nm FWHM. By using the standing wave as a thin lens it is possible to benefit from the strong forces in a relatively small area of

$w_z \times w_y = 10 \times 200 \mu\text{m}^2$. Due to the resulting short focal distance of less than $50 \mu\text{m}$, a final structure size of 10 nm can be achieved with the same atomic beam parameters.

Not only the beam collimation, but also the speed ratio will affect the structure size. Optimal focusing occurs if all atoms have the same axial velocity. However, the experiments with Cr or Al that have been reported so far, have been performed with thermal beams, i.e., beams with an axial velocity spread comparable to the average axial velocity. An additional broadening of the structures will occur as a consequence of this spread, since the focal distance is inversely proportional to the atomic velocity squared.

Figure 5.4 shows the calculated atomic distributions at the focal plane after laser focusing of an atomic Fe beam through a $10 \times 200 \mu\text{m}$ standing wave which is masked by a 100 nm mechanical grating placed $30 \mu\text{m}$ in front of the standing wave. The focal plane is located $42 \mu\text{m}$ behind the center of the standing wave. Three different cases are shown. Graph (a) shows the atomic distributions for a perfect collimated beam. An extremely sharp distribution of less than 0.2 nm FWHM would be obtained with a monochromatic beam (infinite speed ratio). A nearly monochromatic beam with a speed ratio of 10 would lead to a distribution of around 0.7 nm , whereas a thermal Fe beam would give a FWHM of 5 nm .

Figure 5.4(b) shows the same calculations with an Fe beam with a finite collimation of $100 \mu\text{rad}$. These are more realistic parameters, since this collimation can be obtained by Doppler cooling. It is clear that the distributions are broader compared to the previous case. For the same three different speed ratios the FWHM of the atomic distributions are $8, 8$ and 15 nm , respectively. Furthermore, if the beam divergence is doubled to $200 \mu\text{rad}$ as shown in Fig. 5.4(c), the distributions become again broader with a FWHM of $20, 20$ and 40 nm , respectively.

Evidently, both beam parameters, i.e., divergence and speed ratio, seem to have a significant effect on the atomic distribution at the focal plane. Increasing either the beam divergence or the axial velocity spread leads to a broader distribution. Moreover, the effect of speed ratio becomes more pronounced at a better beam collimation. *This clearly demonstrates the need for a (nearly) monochromatic atomic Fe beam if 10 nm structures of Fe should be fabricated.*

The effect of beam masking can be seen in the level of the background of the distributions. If beam masking would not occur, this level would be in the range between 0.5 and 1 (without laser focusing this level would be exactly equal to 1 , and the distribution would be flat). However, with the use of beam masking the background level completely vanishes and the deposited structures become isolated.

4.2 Comparison of standing light wave configurations

Figures 5.5, 5.6 and 5.7 show the results of numerical simulations of atomic trajectories through a standing wave used in the thin lens, thick lens and channeling regime, respectively. Calculations have been performed using the steady-state model indicated by the closed symbols and the dressed atom model (open symbols). The Fe beam has a speed ratio of 10 and a beam collimation of $100 \mu\text{rad}$, which is expected to be experimentally feasible. Beam masking by means of a mechanical grating upstream of the standing wave has not been included in these calculations. However, it has been verified that the primary influence of masking is only on the background level.

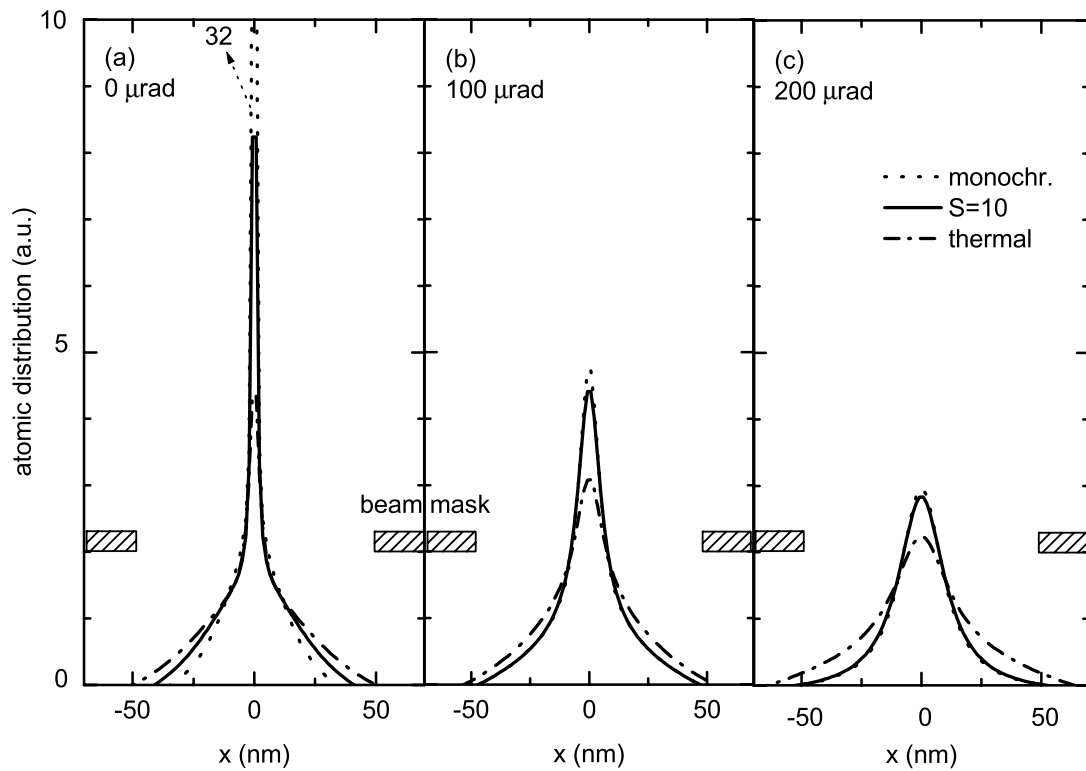


Figure 5.4: Atomic distributions at the focal plane of a $w_z \times w_y = 10 \times 200 \mu\text{m}^2$ standing wave (thin lens regime) calculated with the dressed atom model. Fe beam collimation of $0 \mu\text{rad}$ (a), $100 \mu\text{rad}$ (b) and $200 \mu\text{rad}$ (c) has been used. The Fe beam is initially masked with a 100 nm grating aligned at the nodes of the standing wave (50 mW , 5000 Mrad/s).

Thin lens regime

Figure 5.5 shows the results of simulations on laser focusing of an Fe beam through a $10 \mu\text{m}$ standing wave. Graph (a) shows the location of the focal plane f as a function of the laser power for four different laser detunings in the range of 500 - 5000 Mrad/s. It can be seen that as the power is increased, the focal distance becomes shorter. This is expected, since the forces on the atoms are getting stronger if more laser power is used. Typical focal distances are between 10 and $100 \mu\text{m}$.

The dotted lines show the results for the focal distance as given by the expression of Eq. (5.7). For high f values this expression is in agreement with the simulations. However, deviations occur when the focal distance is getting comparable to the size of the laser beam waist.

The size of the atomic distributions at the focal plane is shown in Fig. 5.5(b). As expected, the FWHM of the distributions decreases with increasing laser power. This can be explained by the fact that the focal distance decreases, thus reducing the increase of the FWHM due to the finite Fe beam collimation. Evidently, at focal distances exceeding $100 \mu\text{m}$, the FWHM of the distributions can become as large as 60 nm, whereas a FWHM of 10 nm is obtained at focal distances of around $20 \mu\text{m}$. Even in the latter case, the laser power can be very modest at a low laser detuning. Using 10 mW at a detuning of 500 Mrad/s leads to a FWHM below 10 nm.

Figure 5.5(c) shows the focused fraction of Fe atoms. This quantity is a direct measure for the saturation of the dipole potential, illustrated in Fig. 5.2. At high saturation the effective area of the dipole potential in which atoms are focused decreases. It is then to be expected that the fraction of focused atoms decreases for higher saturation, i.e., for higher laser power or lower detuning. This can be seen in the simulations. At a low power and high detuning more than 40% of the atoms are focused, whereas at a high power and low detuning this fraction becomes less than 5%.

Figure 5.5(d) shows the contrast of the atomic distribution, defined as the ratio of the maximum of the distribution to the background. Since beam masking has not been used, a background will be present which results in a finite contrast. The contrast increases for increasing laser power, as a result of an increasing maximum. However, it is also clear that the contrast increases with increasing detuning. This is because at higher detuning the background will slightly decrease since more atoms are focused (Fig. 5.5(c)).

Comparison of the results of the two models used, i.e., the steady-state model and the dressed atom model, shows a remarkable agreement. The steady-state is only valid in case the atom can follow the changes of the potential diabatically. This means that a considerable time on the order of $1/\Gamma = 62 \text{ ns}$ is required for an atom to adapt to the changes in the light field. In this case the atoms only spends only 15 ns in the standing wave. However, the agreement can be explained by the fact that the dressed state force given by Eq. (5.13) does not differ significantly from the steady-state force in the region near the nodes. Obviously, both forces vanish exactly at the nodes, but their gradients which are a measure for the focal distance differ hardly. The ratio of these gives $\nabla f_1/\nabla F_{st-st} = 1 + (\Gamma/2\delta)^2$, which is very close to unity in the used parameter range of $\delta \gg \Gamma$. This explains that both models will predict the same location of the focal plane. Only the focused fraction of Fe atoms is higher when the dressed atom model is used, because of a different shape of the corresponding dipole potential. As a result the contrast of the distributions is higher.

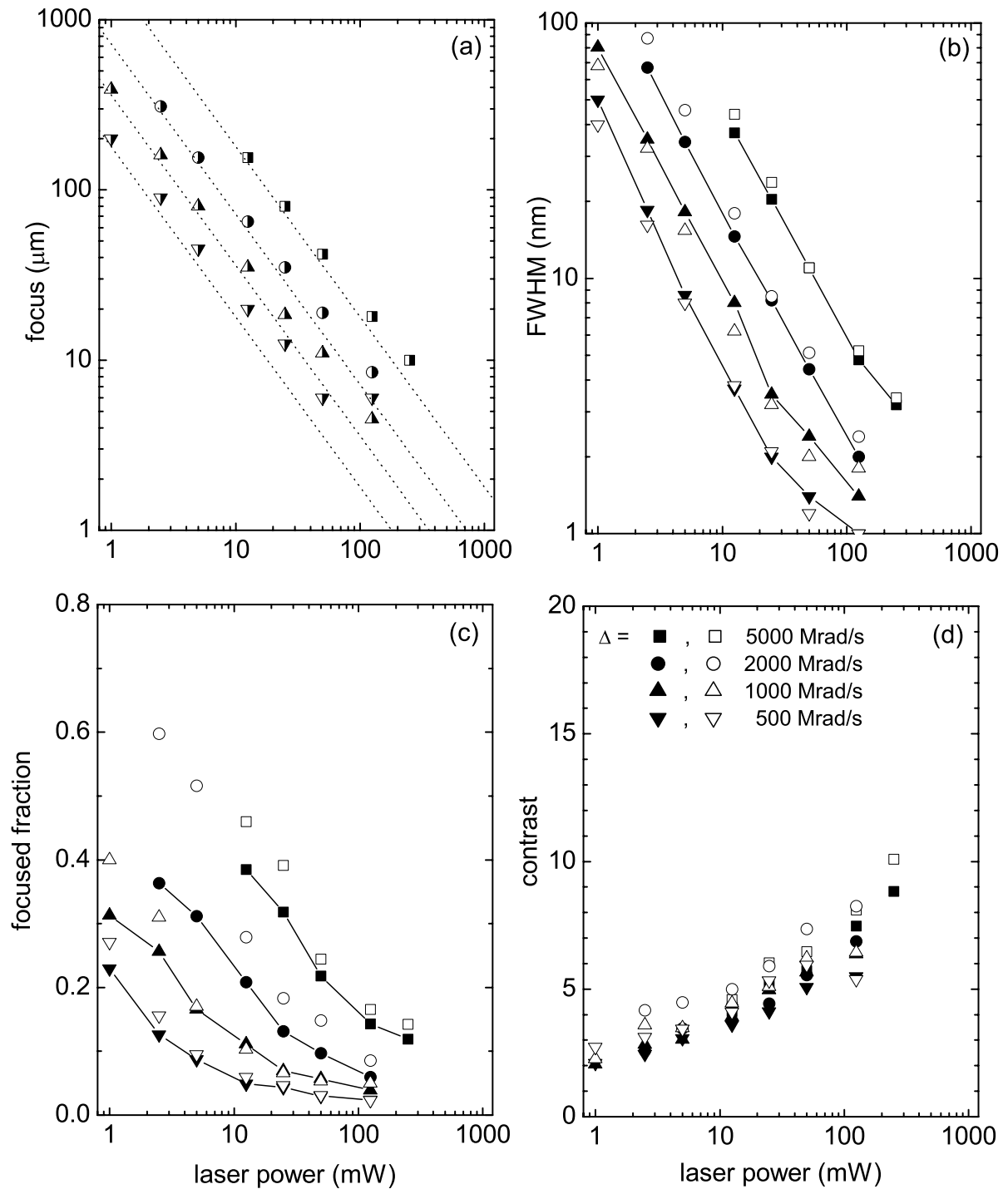


Figure 5.5: Thin lens regime. Closed symbols: steady-state model, open symbols: dressed atom model. Focal distance (a), FWHM of the atomic distribution at the focal plane (b), the fraction of focused atoms (c), and contrast of the distributions (d) are shown as function of the laser power at different laser detunings. The dotted lines in the upper graph represent the calculations of the focal distance according to Eq. (5.7). Standing light wave: $w_z \times w_y = 10 \times 200 \mu\text{m}^2$

Thick lens regime

Figure 5.6 shows the results of numerical simulations of atomic trajectories through a standing wave in which the atoms are focused in the center of the laser beam. It is this regime that has been explored in most experiments. The graph (a) shows the laser beam waist w_z in the direction of the atomic beam that is necessary for focusing at the center. The waist is calculated as a function of the laser power for 4 different laser detunings in the range of 500 - 2000 Mrad/s. It can be seen that as the power is increased, the required beam waist decreases. Higher laser power leads to shorter focal distances, explained by increasingly stronger dipole forces.

The dotted lines show the results for the focal distance as given by the expression of Eq. (5.8). The theory is in agreement with the simulations at low power. At very high laser power this theory predicts smaller beam waists than according to the simulations.

The atomic distribution sizes at the center of the standing wave are shown in Fig. 5.6(b). The FWHM of the distributions will decrease with increasing laser power. At low power, distributions become relatively broad (> 40 nm). However, much smaller distributions of 10 nm are obtained with 30 mW of power at a low detuning of 500 Mrad/s. Compared to focusing with a $10 \mu\text{m}$ thin lens as shown in Fig. 5.5(b), this is approximately 3 times more power.

The focused fraction of atoms is shown in Fig. 5.6(c). Evidently, this fraction decreases for higher laser power and lower detuning, both resulting in a higher saturation of the dipole potential. The contrast of the distributions shown in Fig. 5.6(d) shows a somewhat different behavior than in the previous calculations with the thin lens regime, where the contrast is generally lower.

One of the disadvantages of using a standing wave in the thick lens regime, is that half of the laser power is not used: the substrate is positioned in the center of the laser beam and cuts off half of the beam. Because the laser beam grazes the substrate, diffraction effects might ruin the focusing process. However, in all the experiments performed so far with laser focusing in the thick lenses regime [1,2], a low power in the range of 1 to 10 mW has been used and significant effects from diffraction have not been observed.

Again, a comparison between the two models used for the simulations shows an excellent agreement. Especially at low laser power results are almost identical. In this case the beam waist is relatively large for focusing at the center. Since atoms spend a longer time in the standing wave and intensity gradient are not that strong, the steady-state model is certainly valid.

Channeling regime

Channeling of atoms through a standing wave is a somewhat different process than focusing with a standing wave in the thin or thick lens regime. This has already been shown in Fig. 5.1. A focal plane cannot be defined. The atoms are getting closer to the nodes by oscillatory trajectories with decreasing amplitude since they experience increasingly stronger forces as they are traveling towards the center of the standing wave where the intensity is highest. As in focusing with a thick lens, the substrate needs to be placed at the center.

Figure 5.7(a) shows the FWHM of the atomic distribution at the center of the standing wave. A strong deviation between the two models appears. Distributions are smaller with the dressed atom model. Another difference appears in Fig. 5.7(b), where the contrast of the distributions is shown. With the dressed atom model a contrast in the range of 10 to 100 can be obtained. This is much higher than a typical contrast obtained with focusing with a thin or thick lens. Results with the steady-state model can not be shown in this graph, since the resulting distributions

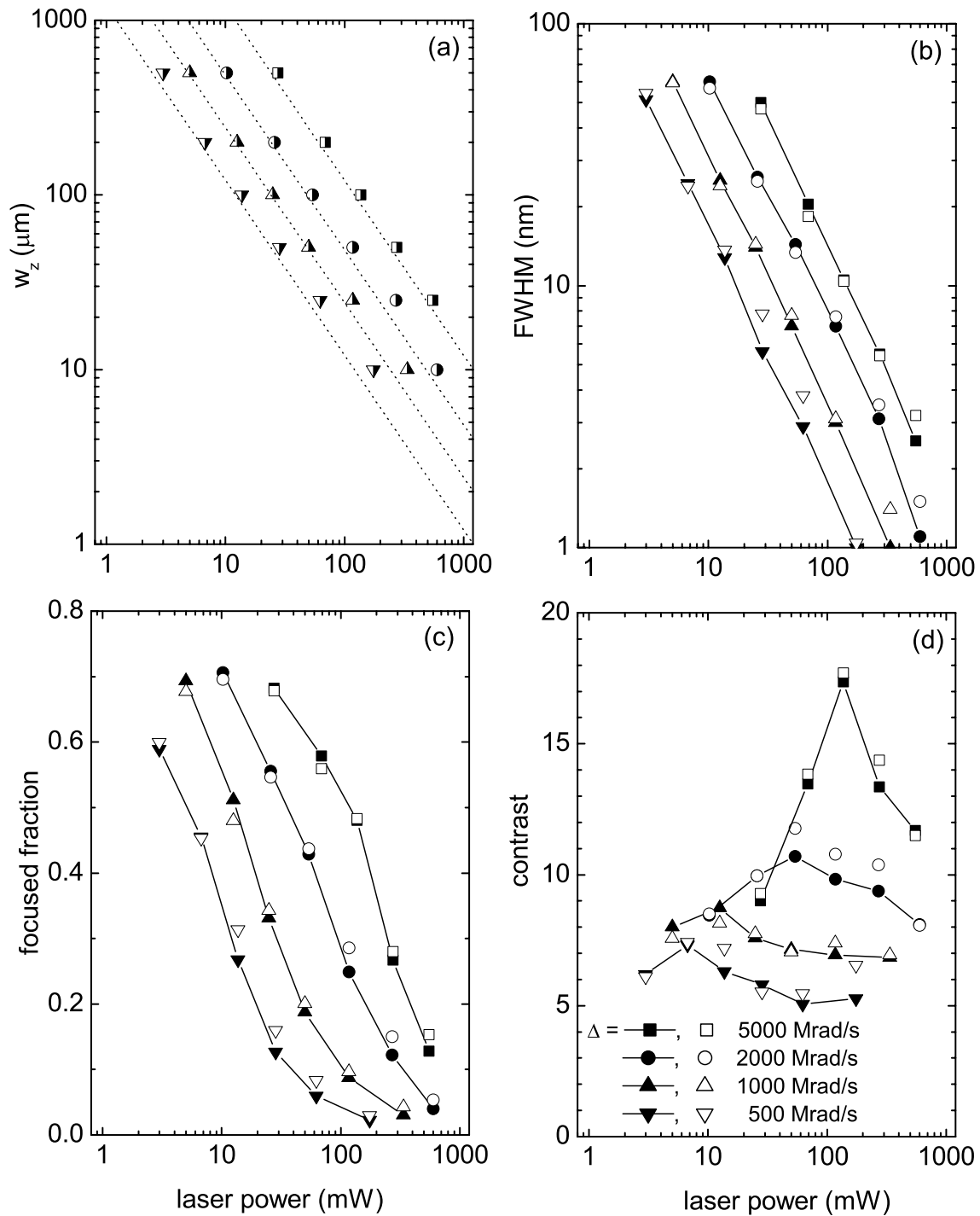


Figure 5.6: Thick lens regime. Closed symbols: steady-state model, open symbols: dressed atom model. Beam waist w_z (a), FWHM of the atomic distribution at the focal plane (b), the fraction of focused atoms (c), and contrast of the distributions (d) are shown as function of the laser power at different laser detunings. The dotted lines in the upper graph represent the calculations of the beam waist according to Eq. (5.8). Standing light wave: $w_y = 200 \mu\text{m}^2$.

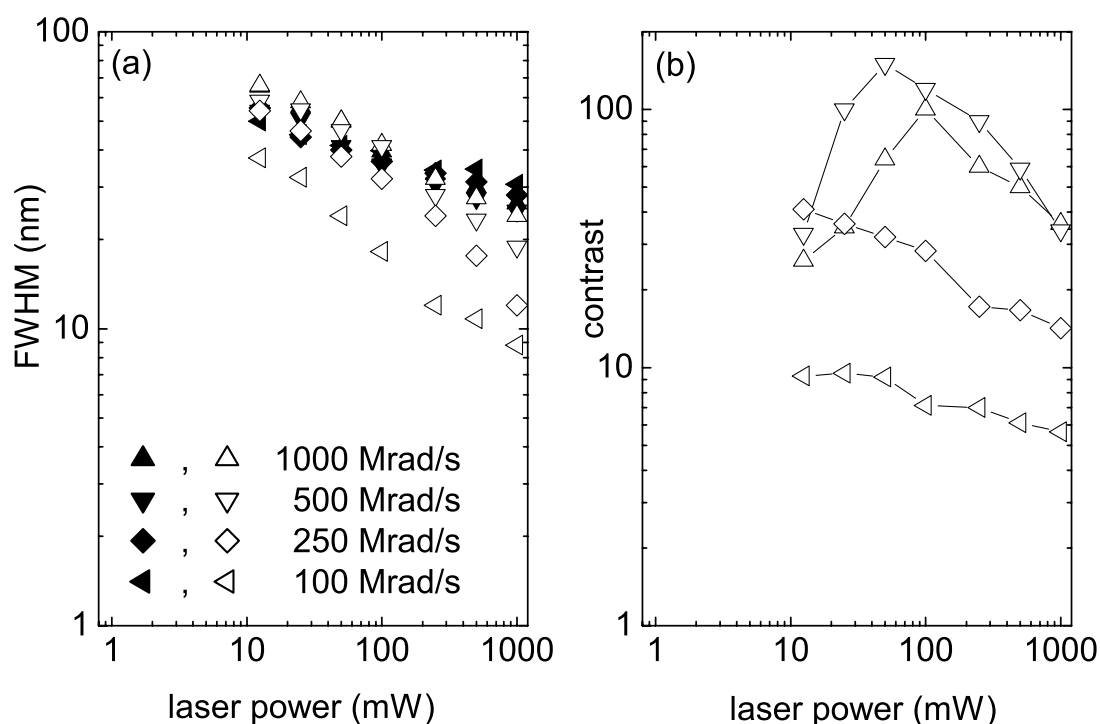


Figure 5.7: Channeling regime. Closed symbols: steady-state model, open symbols: dressed atom model. FWHM of the atomic distribution at the focal plane (a), and contrast of the distributions (b) are shown as function of the laser power at different laser detunings. Note that a strong deviation occurs between the two models. The contrast obtained from the steady-state model which is infinity high (zero background) is not shown. Standing light wave: $w_z \times w_y = 2000 \times 200 \mu\text{m}^2$.

show no background so that the contrast would be infinitely high.

From Fig. 5.8 the difference between both models can be explained. The upper graph shows the trajectories of Fe atoms channeling through a standing wave of $1000 \mu\text{m}$ beam waist in the direction of the atomic beam, detuned at 250 Mrad/s from atomic resonance with a relatively high power of 1000 mW. In the lower graph the same calculations have been performed with the dressed atom model. It is clearly visible how the regions of high intensity are much more occupied in this case. This is a result of spontaneous emissions from dressed state 1 to state 2, in which atoms are attracted to regions of high intensity. The solid circles in the graph indicate the locations of a change of dressed state. The changing sign of the dipole force is beautifully demonstrated by the sudden change in the atomic trajectory after such an event. Especially atoms channeling with a relatively high amplitude around the regions of low light field intensity have a significant probability of decaying into the high field seeking dressed state. The total number of spontaneous decays is 50% higher compared to results obtained with the steady-state model, due to the fact that atoms spend more time in regions of high intensity.

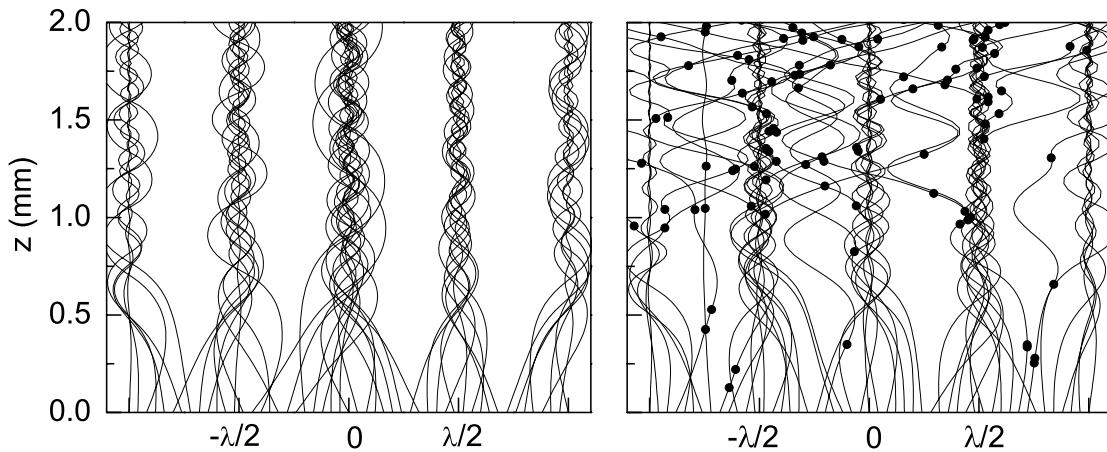


Figure 5.8: Fe atoms channeling through a standing light wave, located at $z = 2.0$ mm. Left: steady-state model. Right: dressed atom model. Solid circles indicate positions of spontaneous decay to another dressed state. Light wave parameters: $P=1000$ mW, $\delta=250$ Mrad/s, $w_z \times w_y=1000 \times 200 \mu\text{m}^2$.

It is to be expected that a background will appear between the structures, something that is not the case with the steady-state model. The difference in structure sizes might intuitively seem surprising: enhanced diffusion of atoms by spontaneous emission from dressed state 1 to 2 leads to smaller structures. For all detunings in the range of 100 to 1000 Mrad/s and for all powers structure sizes become smaller. The effect is more pronounced for high power and low detuning, when spontaneous emission occurs more frequently and trajectories are changed more severely. Structure sizes as small as 10 nm can be reached with 1000 mW of laser power and a detuning of 100 Mrad/s, whereas structure sizes are limited to 30 nm with the steady-state model.

An explanation for this can be found by looking closer at the atomic trajectories as shown in Fig. 5.8. Most of the atoms are localized in the regions around the nodes. The amplitudes of the atomic oscillations around the nodes determines the final distribution size. Atoms oscillating with relatively larger amplitudes spend more time in regions of higher intensity, therefore having more probability of decaying into the high field seeking state. These atoms are the main contribution to the background appearing between the structures in the dressed state model. Since these atoms are smeared out over the entire standing wave, only atoms oscillating very close to the nodes will end up in the structures, resulting in narrower distributions.

Evidently, the steady-state model is not valid in the channeling regime. Since the atoms spend a long time in the relatively broad standing wave of 1 mm, they have a large probability of spontaneous emission. In the example shown in Fig. 5.8 each atom has spontaneously decayed more than 10 times on average. Stimulated diffusion then has a dramatic effect on the atomic trajectories.

5 Atomic diffraction

5.1 Introduction

This section describes the limits of laser focusing due to the wave-properties of the atomic Fe beam. The reason for these limits can be explained by a comparison with ordinary optics. Focusing of, e.g., a laser beam with a perfect lens does not result in a “perfect” image with infinite small dimensions at the focus. The size of the image is in fact limited by diffraction of the light. Focusing of a Gaussian beam results in an image at the focus with a finite size Δx_{FWHM} equal to

$$\Delta x_{FWHM} = \lambda / (2.27NA), \quad (5.29)$$

with λ the wavelength of the laser beam and NA the numerical aperture, which is defined as the ratio of the width d_{FWHM} of the initial laser beam to the focal distance f , or $NA = d_{FWHM}/f$.

Equation (5.29) also holds for laser focusing of an atomic beam. The wavelength of the beam is in this case equal to the atomic deBroglie wavelength λ_{dB} , with $\lambda_{dB} = h/mv$ the ratio of Planck’s constant h to the atomic momentum mv . The numerical aperture NA is defined in the same way as for focusing of a light beam: $NA = d/f$ with d the initial atomic beam width at the node of the standing wave and f the focal distance. However, the initial atomic beam width d which is focused depends on the saturation of the dipole potential of the standing wave. For low saturations this beam width is larger than for high saturations, as illustrated in Fig. 5.2. Typically, d is in the range of 5% to 50% of the periodicity $\lambda/2$, and can be determined from the atomic distribution at the focal plane. In first order, d is proportional to the focused fraction of atoms. For example, if 25% of the atoms end up in the peak of the distribution, then the atomic beam width d that is focused is 25% of the periodicity $\lambda/2$.

The diffraction limit is thus proportional to the focal distance f and inversely proportional to the saturation of the dipole potential. To reduce this limit, low saturation and a short focal distance are required. However, a short focal distance is established using a high laser power and low detuning, since $f \propto \delta/P$ according to Eq. (5.7). The saturation is proportional to the power and inversely proportional to the detuning squared: $s \propto P/\delta^2$. Therefore, to minimize the diffraction a high detuning can be used at a very high laser power, thus reducing both the focal distance and the saturation of the standing wave.

The following example demonstrates the order of magnitude for the diffraction limit. For a perfectly collimated monochromatic atomic beam which is focused by a low saturated standing wave ($d = 0.5\lambda/2$) at $f = 100 \mu\text{m}$ this limit is 2.5 nm. The velocity of the beam is taken to be 1400 m/s, which corresponds to a deBroglie wavelength $\lambda_{dB} = 5 \text{ pm}$.

5.2 Fundamental limits

The effect of the wave-properties of the atomic beam on laser focusing is shown in Fig. 5.9. The two plots show the atomic density of a perfectly collimated and monochromatic atomic Fe beam which is focused 50 μm behind a 10 μm standing wave located at $z = 0$. The plot on the right is obtained from calculations with the dressed atom model. The resulting width of the atomic distribution at the focal plane is 0.2 nm. The plot on the left in Fig. 5.9 shows the results of the full quantum-mechanical calculations. The diffraction pattern of the atomic wave packets

is beautifully demonstrated. The resulting width of the atomic distribution at the focal plane is 2.5 nm, an increase by one order of magnitude.

A more quantitative look is shown in Fig. 5.10. In this graph the calculated FWHM of the atomic distributions at the focal plane are shown for the two simulations as a function of the laser power and for a detuning of 1000 and 5000 Mrad/s. Calculations with classical atomic trajectories result in distributions in the range of 0.1 to 0.5 nm. The quantum mechanical calculations give distributions between 1 and 30 nm, depending on the laser power and detuning. Especially at low laser power the broadening of the distributions due to atomic diffraction is significant. At a detuning of 5000 Mrad/s structures below 10 nm can only be obtained at powers higher than 10 mW. The effect of structure broadening due to finite beam collimation and speed ratio has not been taken into account in these calculations. They only serve to illustrate the *fundamental limitations to laser focusing* due to the wave nature of the Fe atoms.

The dotted lines in Fig. 5.10 show the estimated diffraction limits according to Eq. (5.29). Agreement with the simulations is excellent.

5.3 Practical limits

The previous section showed the fundamental diffraction limits of laser focusing of Fe atoms. These were obtained by simulations of laser focusing with a perfect collimated and monochromatic beam. In this section the results with more realistic beam parameters are shown. Figure 5.11 shows similar atomic density plots as in Fig. 5.9. In this case the incident Fe beam has a finite collimation of $\varphi_{coll} = 100 \mu\text{rad}$ and a speed ratio of $S = 10$. The atomic diffraction pattern which was visible in Fig. 5.9 has disappeared since it is smeared out because of the variation in axial velocity. The two simulations show excellent agreement.

Quantitative results are shown in Fig. 5.12. It gives the FWHM of the atomic distributions at the focal plane. Both simulations give the same results within the same order of magnitude. This can be explained by the fact that the finite beam collimation is mainly responsible for an additional broadening of the structures, which is much larger than the fundamental limits as indicated in Fig. 5.10. Especially at low powers the effect of beam collimation clearly dominates. The resulting distributions are equal in size for both simulations. However, at high powers the results start to deviate. For example, at a power of 100 mW the fundamental limit mainly determines the FWHM of the distributions. Whereas calculations of atomic trajectories gives a FWHM of 1.5 and 3 nm at a detuning of 1000 and 5000 Mrad/s, respectively, the quantum mechanical calculations give a FWHM which is 2 to 3 times larger.

6 Conclusions

Numerical simulations have shown that the Fe beam properties have a significant effect on the atomic distribution at the focal plane of a standing light wave. Increasing either the beam divergence or the axial velocity spread leads to a broadening of the distributions. The effect of beam monochromaticity becomes more pronounced at a higher beam divergence. Therefore, if sub-10 nm Fe structures are to be fabricated, a supersonic Fe beam, collimated to 100 μrad or below, is required.

Simulations on focusing of Fe atoms with a standing wave in the thin lens regime show that

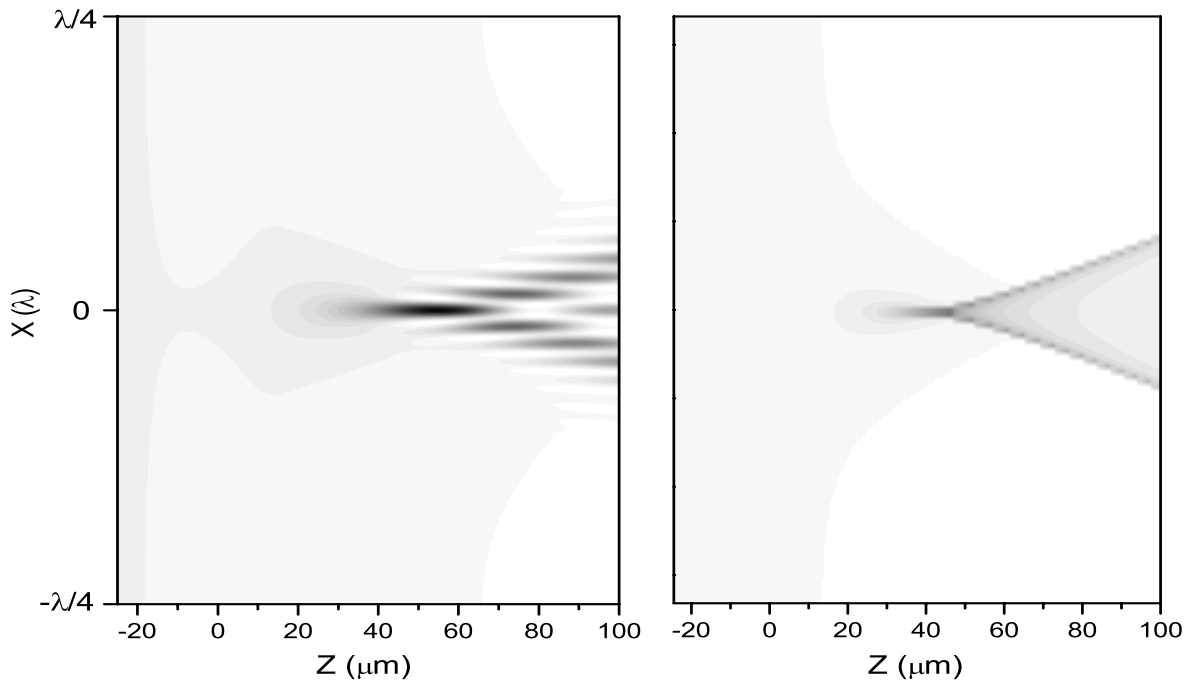


Figure 5.9: Atomic diffraction during laser focusing of a perfectly collimated and monochromatic Fe atomic beam (traveling from left to right) by a $10 \mu\text{m}$ standing wave located at $z = 0$ with $\delta = 5000 \text{ Mrad/s}$ and $P = 50 \text{ mW}$. Left: full quantum mechanical calculation. Right: dressed atom model. The probability density is shown on a grey scale, with black as a maximum density.

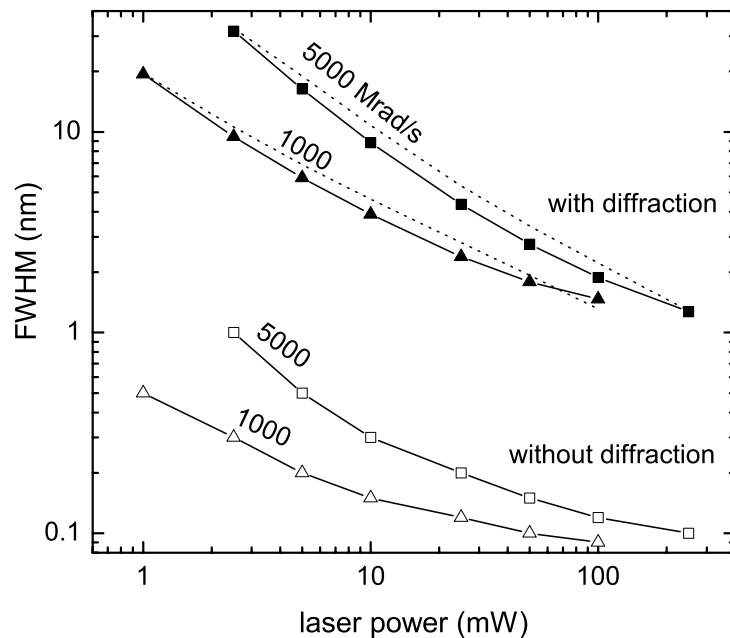


Figure 5.10: FWHM of the atomic distributions at the focal plane after laser focusing a perfectly collimated and monochromatic atomic Fe beam with a $10 \mu\text{m}$ standing wave. Closed symbols represent calculations with the full quantum mechanical model. Open symbols are results of the dressed atom model. The dotted lines are the results of Eq. (5.29). Note that due to atomic diffraction the FWHM increases by one order of magnitude.

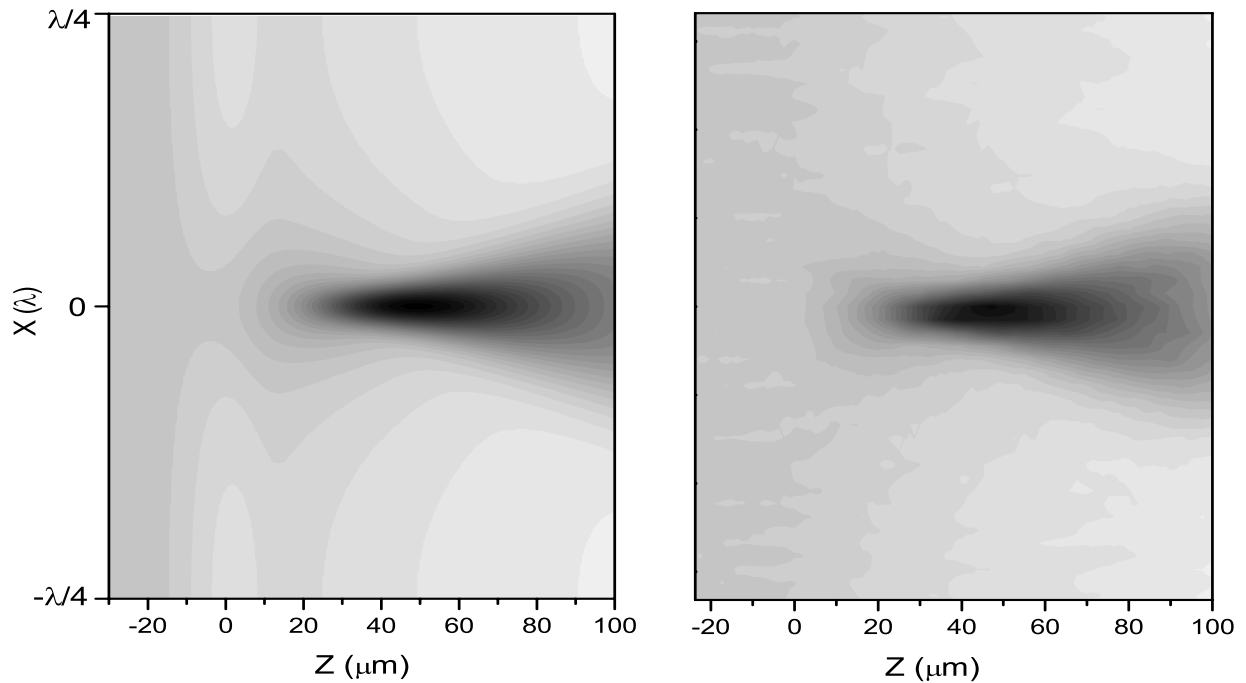


Figure 5.11: Atomic diffraction during laser focusing of an atomic Fe beam (traveling from left to right) of $\varphi_{coll} = 100 \mu\text{rad}$ and $S = 10$ by a $10 \mu\text{m}$ standing wave located at $z = 0$ with $\delta = 5000 \text{ Mrad/s}$ and $P = 50 \text{ mW}$. Left: full quantum mechanical calculation. Right: dressed atom model. The probability density is shown on a grey scale, with black as a maximum density.

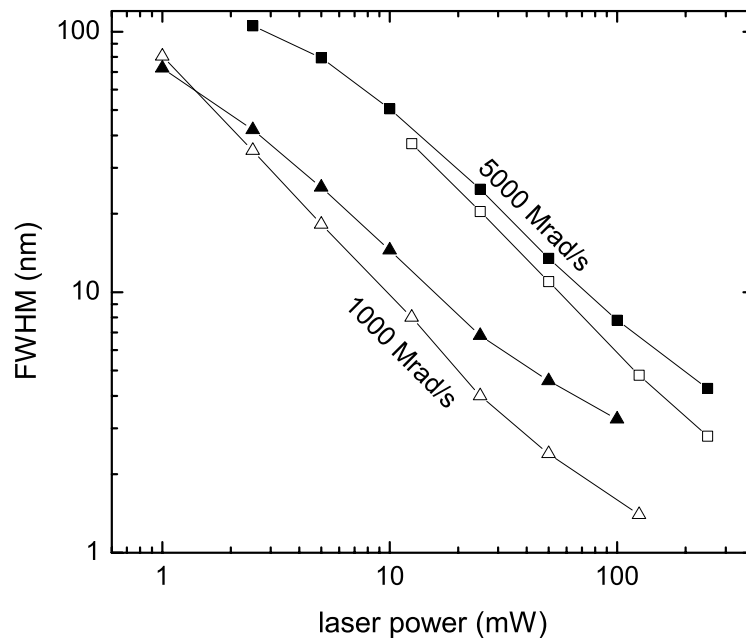


Figure 5.12: FWHM of the atomic distributions at the focal plane after laser focusing an Fe beam with $\varphi_{coll} = 100 \mu\text{rad}$ and $S = 10$ with a $10 \mu\text{m}$ standing wave. Closed symbols represent calculations with the full quantum mechanical model. Open symbols are results of the dressed atom model.

a relatively low power is needed to obtain an atomic distribution of less than 10 nm. At a laser detuning of 500 Mrad/s and 5000 Mrad/s, only 5 mW and 50 mW is required, respectively. However, at higher detuning the contrast of the distributions is higher since the dipole potential is not so much saturated. Because the area of the laser beam of the standing wave is relatively small, the laser intensity is very large, resulting in short focal distances in the range of 10 to 50 nm.

If a thick lens is used to focus the Fe atoms at the center, approximately 5 times more laser power is needed to obtain an atomic distribution of less than 10 nm. One of the reasons for this is that half the laser power is lost since the substrate will cut off half of the laser beam.

The steady-state model cannot be used for the calculations of channeling of Fe atoms through a standing wave. Adequate channeling occurs at high laser intensity and low detuning. In this regime the effect of spontaneous emission leads to a significant stimulated diffusion of atoms in the standing wave, which has a dramatic effect on the atomic distributions at the center of the standing wave. Using 500 mW of laser power at a detuning of 100 Mrad/s, the distribution has a FWHM of 10 nm, with a reasonable contrast of 6. A practical advantage of the channeling regime is that it is relatively alignment-free; no exact tuning of the focal distance by adjusting the laser power or the substrate position is necessary. Moreover, small fluctuations in the light field parameters will not significantly alter the channeling process.

The fundamental limits of laser focusing of Fe atoms due to atomic diffraction are determined with full quantum mechanical calculations. These limits are in the range of 10 to 1 nm for focusing an ideal Fe beam with a thin lens. Since the diffraction limit is inversely proportional to the numerical aperture, the saturation of the standing wave potential needs to be taken into account. The effect of diffraction on focusing of a 100 μm supersonic Fe beam is still discernable. However, sub-10 nm structures are still feasible.

References

- [1] J.J. McClelland, R.E. Scholten, E.C. Palm, and R.J. Celotta, *Science* **262**, 877 (1993)
- [2] McGowan, R.W., D. Giltner, and Siu Au Lee, *Opt. Lett.* **20**, 2535 (1995)
- [3] W.R. Anderson, C.C. Bradley, J.J. McClelland, and R.J. Celotta, *Phys. Rev. A* **59**, 2476 (1999)
- [4] S.J.H.Petra, L.Feenstra, W.Vassen and W.Hogervorst, International Quantum Electronics Conference CLEO/Europe-IQEC 2000
- [5] M. Drewsen, U. Drodofsky, C. Weber, G. Schreiber, and J.Mlynek, *J. Phys. B* **29**, 843 (1996)
- [6] B. Brezger, Th. Schulze, U. Drodofsky, J. Stuhler, S. Nowak, T. Pfau, and J. Mlynek, *J. Vac. Sci. Technol.* **B15**, 2905 (1997)
- [7] J.J. McClelland, *J. Opt. Soc. Am. B* **12**, 1761 (1995)
- [8] K.K. Berggren, M. Prentiss, G.L. Timp, and R.E. Behringer, *J. Opt. Soc. Am. B* **11**, 1166 (1994)
- [9] J. Dalibard and C. Cohen-Tannoudji, *J. Opt. Soc. Am. B* **2**, 1707 (1985)
- [10] H.J. Metcalf and P. van der Straten, *Laser Cooling and Trapping*, Springer-Verlag New York, 1999

- [11] A.E.A. Koolen, *Dissipative atom optics with cold metastable helium atoms*, Ph.D. thesis, Eindhoven University of Technology (2000)
- [12] B.R. Mollow, *Phys. Rev. A* **12**, 1919 (1975)

Chapter 6

Laser cooling of an atomic Fe beam

1 Introduction

Laser focusing of Fe atoms requires a well collimated beam. From calculations presented in Chapter 5 it turns out that an Fe beam with a divergence of $200 \mu\text{rad}$ FWHM or lower is necessary for the production of sub-10 nm structures of Fe.

Collimating the Fe beam simply by using apertures would dramatically reduce the Fe beam flux. A solution to the problem is to apply transverse laser cooling [8]. Laser cooling is a well known technique, that has successfully been applied to a large number of elements. It is also used for beam collimation in similar experiments on laser focusing [1–7].

The simplest mechanism of laser cooling is based on the Doppler effect experienced by the Fe atoms, and is commonly referred to as *Doppler cooling*. Doppler cooling of an atomic Fe beam has never been performed. In principle this process requires a closed two-level system, which means that the excited state can only decay to the initial state of the transition. However, the transition used for the cooling of the Fe atom is not perfectly closed. This is illustrated in Fig. 6.1(a). The 5F_5 excited state has probabilities of $1/243$ and $1/1420$ to spontaneously decay to metastable states that are lost for laser focusing. Figure 6.1(b) shows the percentage of Fe atoms that is still in the ground state as a function of the number of emitted photons. It can be seen that only 65, 40 and 20% of the Fe atoms remains in the initial state after 100, 200 and 400 spontaneous emissions, respectively.

The loss of Fe atoms to metastable states has two consequences for the process of laser focusing. First of all, there is a significant loss of beam flux of ground state Fe atoms so that the deposition rate of the structures is lower. Secondly, the metastable Fe atoms will contribute to a background in between the structures since these atoms are not affected by the standing light wave. Therefore the number of photons used for the laser cooling process should be as low as possible, preferably below 100. Numerical simulations have been performed in order to investigate if this requirement can be fulfilled if the resulting Fe beam divergence is still low enough, i.e., below $100 \mu\text{rad}$. Results are presented in this chapter.

It is also important to mention that the laser cooling of the Fe beam has a second purpose. The Fe atomic ground state has an angular momentum of $J = 4$, with magnetic sublevel quantum number m_J in the range from -4 to $+4$. A distribution in these sublevels is not desired for laser focusing, since the dipole force used to focus the atoms is different for each magnetic

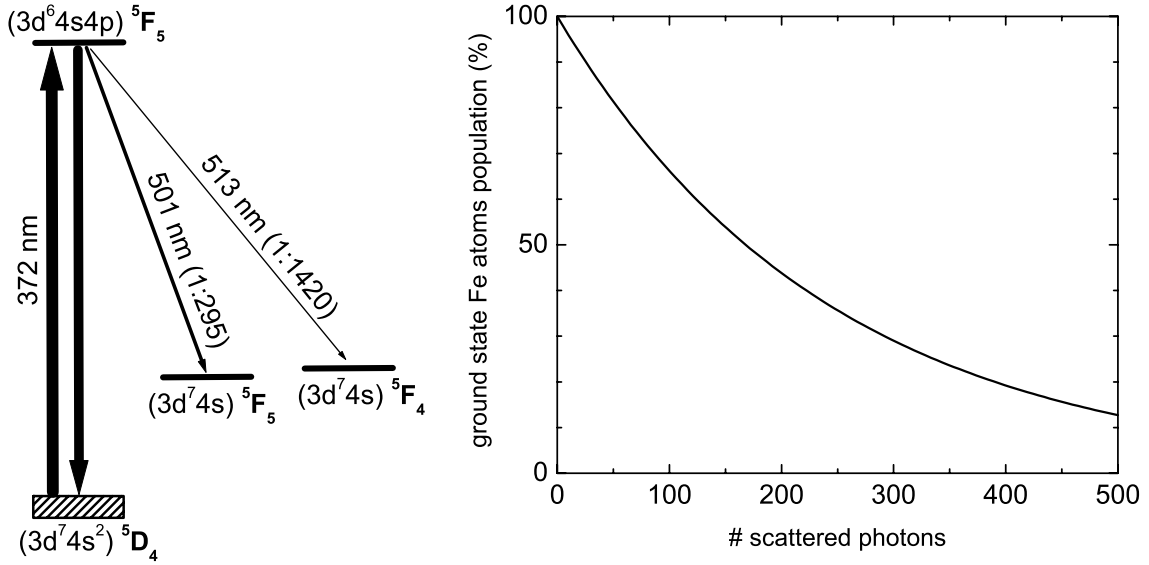


Figure 6.1: (a) Ground state and excited state levels of Fe used for laser cooling with two most dominant leaks to metastable states. (b) Ground state Fe population as a function of the number of emitted photons.

sublevel m_J . Therefore, circularly polarized light should be used for laser cooling to pump all atoms to either the $m_J = +4$ or $m_J = -4$ magnetic sublevel.

First, the theoretical aspects of the cooling process are explained. Two mechanisms are introduced, namely Doppler cooling and sub-Doppler cooling, which can be used as a second stage cooling process to reduce the beam divergence even further. Subsequently, the simulation results are presented. The chapter ends with a description of the experimental setup that has been developed to perform laser cooling on an atomic Fe beam.

2 Theoretical aspects of laser cooling

2.1 Doppler cooling

Consider a two-level atom in a resonant running laser beam. By absorbing a photon from the laser, the atom obtains the photon's momentum $\hbar k$, which is directed along the laser beam. After subsequent spontaneous emission, the atom gains an additional recoil, equal in magnitude, but in a random direction. After many cycles of absorption and spontaneous emission, the atom has gained a net momentum in the direction of the laser beam, since all the recoil momenta of the spontaneous emission add up to zero. The resulting average force, also denoted as radiation force, is given by

$$\vec{F} = \hbar \vec{k} \Gamma n_e, \quad (6.1)$$

with Γ the decay rate of the excited state and n_e the excited state population. For resonant excitation this population is given by $n_e = s_0 / (2(s_0 + 1))$, with s_0 the on-resonance saturation parameter of the laser field, defined by the ratio of the laser intensity I to the saturation intensity I_0 of the atomic transition $s_0 = I / I_0$. The radiation force saturates for $I \rightarrow \infty$, resulting in

a maximum force of $\hbar k \Gamma / 2$. For Fe this maximum force corresponds to an acceleration of $1.6 \cdot 10^5 \text{ m/s}^2$. For off-resonant excitation, in which the frequency of the light field is slightly detuned with respect to the atomic resonance frequency, the radiation force is given by

$$\vec{F} = \frac{\hbar \vec{k} \Gamma}{2} \frac{s_0}{1 + s_0 + (2\delta/\Gamma)^2}, \quad (6.2)$$

with δ the detuning of the laser from resonance.

In a coordinate frame moving along with the atom the detuning δ does not only depend on the laser detuning, but also has a contribution $-\vec{k} \cdot \vec{v}$ due to the Doppler effect. The radiation force therefore depends on the velocity component of the atom along the direction of the laser beam. The basis for Doppler cooling is formed by this velocity dependence. In the case of two counter propagating laser beams with the same detuning from resonance, an atom experiences two forces which are imbalanced if the velocity of the atom is not zero due to the different Doppler shifts. If the laser beams are red-detuned ($\delta < 0$), the atoms will absorb more photons from the laser beam directed opposite to the atomic velocity than from the other laser beam. As a result the sum of the two forces is directed opposite to atomic velocity and results in a friction-like *cooling force* which damps the atomic motion. In the limit of small saturation parameters and small atomic velocity this force is equal to

$$\vec{F} = 4\hbar k^2 v \frac{s_0 2\delta/\Gamma}{1 + (2\delta/\Gamma)^2} \equiv -\beta \cdot v, \quad (6.3)$$

with $\beta (\geq 0)$ the damping coefficient. Fig. 6.2(a) shows the velocity dependent force on an Fe atom for a light field detuning of $\delta = -\Gamma/2$ and a saturation parameter of $s_0 = 1$ of each beam. As can be seen, the force acts as a linear damping force for atoms in the velocity range of $|v| < v_c$, with v_c the so-called capture velocity which is proportional to the detuning: $v_c \sim \delta/k$. Atoms with velocities higher than the capture velocity are less efficiently cooled.

The damping force given by Eq. (6.3) is responsible for the cooling of the atoms in the direction of the laser beams. However, there is a limit to this cooling process, since the radiation force also gives rise to heating. This heating mechanism stems from the randomness of the momentum steps taken by the atom. The motion of the atom can be compared to a random walk in momentum space, caused by the randomness in direction of the spontaneously emitted photons and by the uncertainty in the number of absorbed photons from the light field. The heating corresponding to this random walk process can be expressed in terms of a momentum diffusion coefficient \mathcal{D} [9].

The temperature of the atoms is defined for each degree of freedom by $k_B T_i / 2 = m \langle v_i^2 \rangle / 2$, with k_B the Boltzmann constant and m the atomic mass. Equilibrium between heating and cooling is reached when the heating rate $\langle \dot{E}_{heat} \rangle = \mathcal{D} / m$ equals the cooling rate of the damping force $\langle \dot{E}_{cool} \rangle = \langle F v_i \rangle = \beta \langle v_i^2 \rangle$:

$$k_B T_i = \frac{\mathcal{D}}{\beta} = -\frac{\hbar k}{4} \left(\frac{\Gamma}{2\delta} + \frac{2\delta}{\Gamma} \right). \quad (6.4)$$

The minimum temperature T_D is reached for $\delta = -\Gamma/2$: $k_B T_i = \hbar \Gamma / 2$ and is called the Doppler limit. For Fe the Doppler temperature T_D is equal to $62 \mu\text{K}$, which corresponds to an rms velocity of 9.6 cm/s . Table I gives the atomic properties of the Fe atom relevant for Doppler cooling.

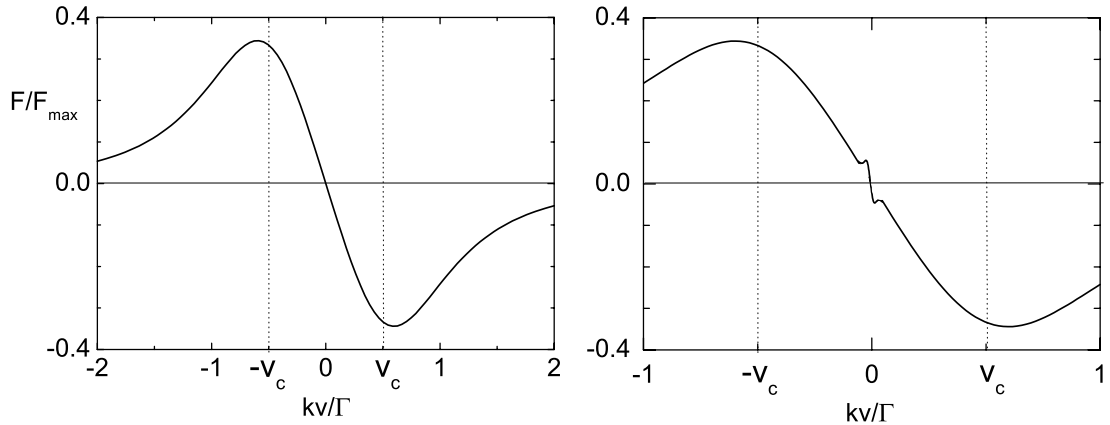


Figure 6.2: (a) Velocity dependent radiation force of two counter propagating waves with optimal Doppler cooling light field parameters ($\delta/\Gamma = -1/2$, $2s_0 = 2$). (b) Sub-Doppler velocity dependent force of two counter propagating laser beams ($\delta/\Gamma = -1/2$, $2s_0 = 2$) with $\text{lin} \perp \text{lin}$ polarization. Sub-Doppler cooling works for velocities much smaller than the capture velocity of Doppler cooling ($v \ll v_c$), where gradients in the force can become very large.

Table I: Properties of the Fe atom relevant for Doppler cooling.

atomic properties		
atomic mass number	m	56
resonant wavelength	$\lambda = 2\pi/k$	372.0 nm
excited state decay rate	Γ	16.2 Mrad/s
saturation intensity	I_0	62 W/m ²
recoil velocity	$v_{rec} = \hbar k/m$	1.9 cm/s
properties at Doppler limit		
temperature	T_D	62 μK
velocity	v_D	9.6 cm/s
beam divergence at $v_z = 1400$ m/s	φ_{coll}	69 μrad

2.2 Sub-Doppler cooling

The interaction between nearly resonant light and atoms not only drives transitions between atoms, but also shifts their energies. These shifts are essentially caused by the AC Stark effect from the electric field of the light [9]. In the low intensity limit of two laser beams with combined saturation parameter $2s_0$, the light shift ΔE_g of the ground magnetic substates is given by [9]

$$\Delta E_g = \hbar\delta \frac{s_0 C_{eg}^2}{1 + (2\delta/\Gamma)^2}, \quad (6.5)$$

where C_{eg} is the Clebsch-Gordan coefficient that takes into account explicitly the angular momentum dependent part of the atom–field coupling. Since C_{eg} thus depends on the magnetic quantum numbers and on the polarization of the field, the light shifts are different for different magnetic sublevels. For example, for a $J = 1/2 \rightarrow 3/2$ transition with σ^+ light, the light shift for the magnetic substate $m_g = +1/2$ is three times larger than that of $m_g = -1/2$ substate. If σ^- light is used, this ratio is reversed.

In a standing wave consisting of two counter-propagating waves with orthogonal linear polarizations (lin \perp lin), the polarization contains gradients: it changes in position along the wave vector. This effect is illustrated in Fig. 6.3(a). In this configuration the polarization changes from σ^+ to linear to σ^- along the direction of the standing wave. Where the light field is purely σ^+ , optical pumping drives the ground state population to the $m_g = +1/2$ sublevel, because absorptions always produce $\Delta m = +1$ transitions and subsequent spontaneous emissions produce $\Delta m = 0, \pm 1$. For σ^- -light the population will be pumped toward the $m_g = -1/2$ sublevel. Thus in traveling through half a wavelength, the atoms try to adjust their population completely from $m_g = -1/2$ to $m_g = +1/2$ and back again.

Optical pumping in this case increases the population in the state with the larger light shift. This is generally true for any transition from J_g to $J_e = J_g + 1$ [10]. For a $J = 4 \rightarrow 5$ transition, like the Fe transition used for cooling, the potentials of the magnetic sublevels are more complicated. Fig. 6.3(c) shows these potentials. The mechanism of sub-Doppler cooling can best be explained by the simpler case of a $J = 1/2 \rightarrow 3/2$ case, as shown in Fig. 6.4, but the principle does not change for the $J = 4 \rightarrow 5$ transition.

Atoms starting at $z = -\lambda/2$ in the $m_g = +1/2$ sublevel must climb the potential hill as they approach the $z = -\lambda/4$ point where the light becomes σ^- polarized, and they are optically pumped to the $m_g = -1/2$ sublevel. Then they must climb another hill. Each optical pumping event results in the emission of light at a higher frequency than that of the absorbed light, thus dissipating energy into the radiation field. This process repeats until the atomic kinetic energy is too small to climb the next hill.

Fig. 6.2(b) shows an example of the total velocity dependent force on an atom in a standing wave with a lin \perp lin polarization gradient. This force is similar to the damping force for Doppler cooling, as shown in Fig. 6.2(a). However, for small velocities where the sub-Doppler cooling process is effective, the force shows a very strong gradient which results in a strong damping of the atomic motion. The damping coefficient (equal to the gradient of the force) is approximately $2|\delta|/\Gamma$ times larger than the maximum damping coefficient for Doppler cooling. The heating coefficient is, however, of the same order of magnitude for both processes. This means that with sub-Doppler cooling, temperatures lower by a factor of $2|\delta|/\Gamma$ can be reached than with Doppler cooling. Since the damping coefficient is also roughly independent

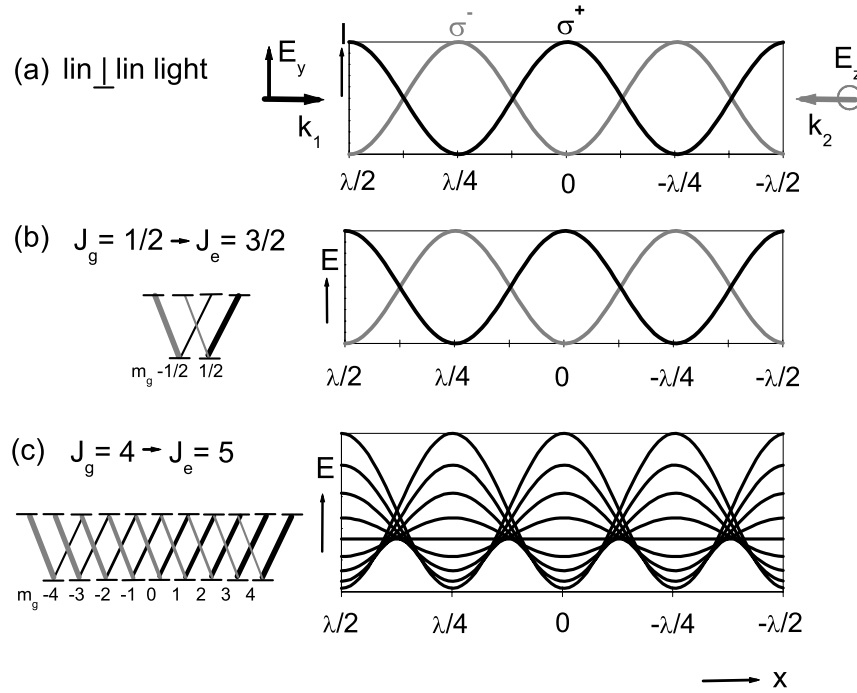


Figure 6.3: Energy shifts of magnetic sublevels in a lin \perp lin standing wave configuration: (a) polarization gradients in a lin \perp lin standing wave, (b) energy shift for a $J = 1/2 \rightarrow 3/2$ atomic transition, (c) energy shift for a $J = 4 \rightarrow 5$ atomic transition.

of the laser intensity, the sub-Doppler temperature limit decreases for lower intensity and higher detuning.

However, there is one important disadvantage if sub-Doppler cooling is used, even if it reduces the Fe beam divergence. The process of sub-Doppler cooling is based on different light shifts of the atomic magnetic sublevels. Therefore, it is not possible to pump all atoms to the $m_J = +4$ or $m_J = -4$ sublevel, which is desirable for laser focusing. After sub-Doppler cooling the Fe atoms will be distributed among all magnetic sublevels.

3 Simulations

3.1 Doppler cooling

Simulation program

Doppler cooling simulations of the Fe atomic beam have been performed with classical Monte Carlo calculations. In each simulation, 5000 trajectories of Fe atoms are calculated. Figure 6.5 shows schematically the geometry that has been used for the simulations. At the Fe source nozzle ($z = 0$) the atoms have an initial distribution along the x direction $P^0(x)$ and an initial transverse velocity distribution $P^0(v_x)$, with $P^0(x)$ a uniform distribution with a full width of $2\Delta x = 500\mu\text{m}$, with Δx equal to the virtual source radius of the supersonic expansion, and $P^0(v_x)$ a uniform distribution of transverse velocities in the range of -6 to 6 m/s. The velocity

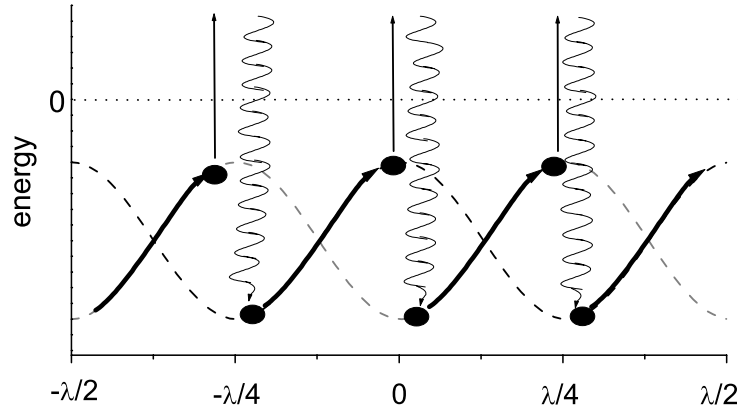


Figure 6.4: Principle of lin \perp lin sub-Doppler cooling for a $J = 1/2 \rightarrow 3/2$ atomic transition. The arrows show the path followed by atoms being cooled in this configuration.

Table II: Input parameters of the Monte Carlo calculations for the simulation of Doppler cooling of an Fe beam.

# Fe atoms	5000	interval #1	$L = 10$ cm
axial velocity v_z	(1400 ± 140) m/s		no light field
initial x distribution $P^0(x)$	$1, x < 250 \mu\text{m}$	interval #2	$L = 10$ cm
	$0, x > 250 \mu\text{m}$		light field on
initial v_x distribution $P^0(v_x)$	$1, v_x < 6$ m/s		intensity s_0
	$0, v_x > 6$ m/s		detuning δ

range of captured atoms for laser cooling, with is on the order of $|v_x| < \delta/k$ is well within the range of the velocity distribution $P^0(v_x)$. For each initial value of x , the initial velocity is taken randomly from the distribution $P^0(v_x)$.

The atoms move freely in straight trajectories during the first 10 cm, after which they enter the region of the light field. In this 10 cm long region the atoms are Doppler cooled with circularly polarized light. At $z = 20$ cm the distribution $P(x)$ gives the Doppler cooled beam width and $P(v_x)$ gives the beam divergence φ_{coll} . From now on the beam divergence will be expressed in terms of φ_{coll} which is defined as the HWHM velocity of the Gaussian fit of $P(v_x)$:

$$P(v_x) \propto \exp\left[-v_x^2/(2dv_x^2)\right], \quad (6.6)$$

$$\varphi_{coll} \equiv dv_x/v_z\sqrt{2 \ln 2}. \quad (6.7)$$

Each of the 5000 atomic trajectories starts with an initial position and velocity of the atom taken from $P^0(x)$ and $P^0(v_x)$. Each calculated trajectory results in a final position and transverse velocity of the atom. The final distributions $P(x)$ and $P(v_x)$ are obtained by taking a histogram of x and v_x , respectively, of all 5000 trajectories. Table 3.1 gives the input parameters of the program.

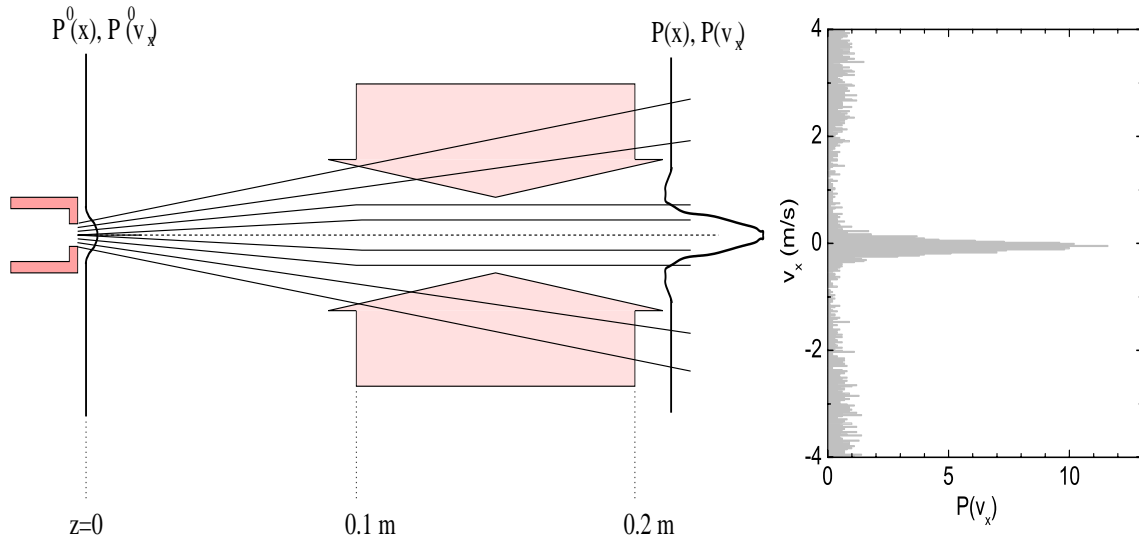


Figure 6.5: Left: geometry of the Doppler simulation of an Fe beam. Right: example of a calculated velocity distribution after Doppler cooling for $s_0 = 0.5$ and $\delta/\Gamma = -1$.

Results

Figure 6.6 shows the results of the calculations on Doppler cooling. The beam divergence φ_{coll} is given in the upper graph for various saturation parameters s_0 and laser detunings δ (s_0 is the saturation parameter of a single running wave, $2 \cdot s_0$ of both counter propagating beams). A saturation parameter $s_0 = 1$ corresponds to a laser power of 31 mW. For the two lowest detunings $\delta/\Gamma = -0.5$ and -1.0 the beam divergence φ_{coll} is independent of the saturation parameter s_0 . In this region the cooling limit has been reached. Theoretically these limits are 68 and 76 μrad for detunings of -0.5 and -1.0 , respectively. These values are in agreement with the calculations. For a higher detuning it is clear that the beam divergence decreases for increasing laser intensity. In this region the cooling limit has not been reached since the number of scattered photons from the light field is too small. A beam divergence of 100 μrad or less can be reached for laser detunings of -0.5 or -1.0 , or a laser detuning of -1.5 at saturation parameter of $2s_0 = 4$.

The middle graph shows the number of photons that has been absorbed and emitted from both laser beams. Clearly, more photons are absorbed at lower detunings, since the laser frequency is getting closer to the atomic resonance frequency. Obviously, by increasing the laser intensity more photons are absorbed by the Fe atoms. If a maximum number of 100 photons should be scattered, the laser detuning should not be smaller than -1.5 for a saturation parameter of $2s_0 > 1$, or not smaller than -1.0 for $2s_0 = 1$.

The lower graph of Fig. 6.6 shows the beam width d_{FWHM} of the Doppler cooled Fe beam. It is clear that the beam width increases at higher detunings. This is because the beam width is determined by the initial beam width (equal to twice the virtual source radius) and the maximum transverse velocity v_c at which Fe atoms can still be captured by the laser beam. The capture velocity v_c scales simply with the laser detuning according to $v_c \approx \delta/k$, with k the wave vector

of the laser field. It can also be seen that the beam width does not depend on the saturation parameter s_0 , which is to be expected if the Doppler limit has been reached. If this is not the case, the Fe beam width d_{FWHM} increases with increasing s_0 . Typical beam widths of the Doppler cooled Fe beam are 300 to 700 μm . This is convenient for laser focusing, since these beam sizes are larger than a typical length over which laser focusing occurs. This length scale is mainly determined by the size of the mechanical masks that are used upstream of the focusing wave ($250 \times 250 \mu\text{m}^2$). This means that the alignment of the mask/focusing wave assembly with the collimated Fe beam is relatively easy.

In conclusion, a compromise between keeping the number of scattered photons small and achieving good beam collimation has to be made when choosing the laser detuning and intensity.

3.2 Sub-Doppler cooling

Simulation program

A full Quantum Monte Carlo (QMC) numerical simulation program is used to calculate the process of one-dimensional sub-Doppler cooling of an Fe beam. Compared to Doppler cooling calculations, the calculation for sub-Doppler cooling is much more involved, mainly because the atoms are represented by full quantum-mechanical wave packets. Basically, the QMC calculations are based on Mollow's treatment of resonant light scattering [11, 12]. They are able to describe sub-Doppler as well as Doppler cooling. This treatment is briefly described by Hoogerland *et. al.* [13] and more extensively in [14].

Without further approximations, the calculation time required for sub-Doppler cooling is on the order of 25 hours on a PII/350, depending on the initial transverse velocity range of the atomic beam. To reduce the calculation time, the following assumptions are made:

- the contribution of sub-Doppler cooling can be ignored in the first half of the interaction region
- Doppler cooling cools the atoms to a beam divergence of $\phi_{coll} = 200 \mu\text{rad}$ in the first half of the interaction region

Sub-Doppler cooling only works for atoms that already have a very low transverse velocity, and is therefore very ineffective in the early cooling process. Therefore the QMC calculations start at the second half of the interaction region, which is 100 mm long in total.

The second assumption might seem rather rigorous, since the beam divergence depends on the light field parameters. However, by assuming a relatively low initial beam divergence for sub-Doppler cooling, the transverse velocity range can be significantly reduced. The final velocity distribution is therefore a bimodal Gaussian distribution with widths corresponding to the Doppler and sub-Doppler temperatures. The Doppler temperature is, however, not a reliable result, because of the second assumption. A much more reliable Doppler temperature can be obtained from the Doppler cooling simulations described before. The QMC simulations merely serve to investigate the contribution of sub-Doppler cooling to the final beam divergence.

Results

Figure 6.7 shows the results of calculations of sub-Doppler cooling of an Fe beam. The upper graph shows the beam divergence ϕ_{coll} , which is the width of the narrow part of the bimodal

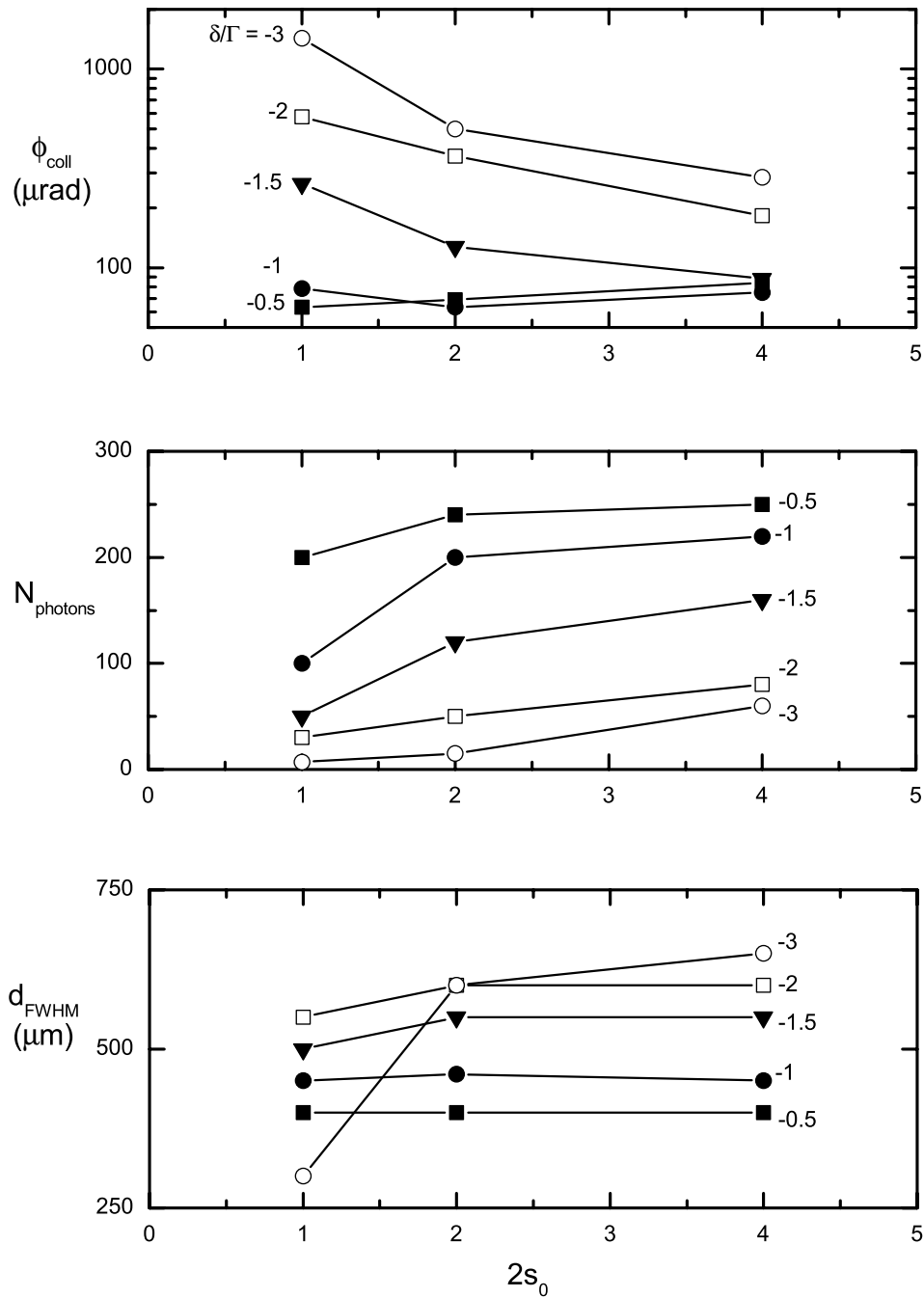


Figure 6.6: Results of Fe Doppler cooling simulations. The three graphs show the Fe beam divergence (top), average number of scattered photons (center) and Doppler cooled Fe beam width (bottom). These quantities are calculated for various laser detunings and saturation parameters.

distribution. With sub-Doppler cooling a beam divergence in the range of 15 to 40 μrad can be achieved, which is an order of magnitude less than a beam divergence obtained with Doppler cooling (see Fig. 6.6). It can also be seen that the Fe beam divergence decreases if the saturation parameter becomes lower and if the detuning becomes larger. This is to be expected theoretically.

The middle graph as shown in Fig. 6.7 gives the population of the sub-Doppler cooled Fe atoms. This population is defined as the fraction of Fe atoms within the sub-Doppler cooled range given in the upper graph. Typical sub-Doppler cooled populations are in the order of 1 to 50%, depending on the laser detuning and saturation parameter. The sub-Doppler cooled population increases for higher saturation parameters and lower detunings.

The lower graph of Fig. 6.7 shows the average number of photons scattered over the 5 cm interval of sub-Doppler cooling. As also shown in Fig. 6.6, the number of absorbed and emitted photons increases for smaller detuning and larger saturation parameter. If the number of scattered photons has to be kept below 50, the saturation parameter $2s_0$ should be kept below 0.5, 1 and 4 for detunings of -0.5 , -1 and -1.5 , respectively. For higher detunings the number of scattered photons is always below 50 in the range $0 < 2s_0 < 10$.

To obtain a large fraction of sub-Doppler cooled Fe atoms and a small number of scattered photons, large detunings should be used at large saturation parameters. E.g., a detuning of -2.0 at $2s_0 = 4$ gives a 45% sub-Doppler cooled population within 30 μrad with approximately 50 photons scattered. A higher detuning of -3.0 at $2s_0 = 6$ gives a 47% population within 30 μrad with 47 photons scattered.

3.3 Doppler and sub-Doppler cooling

Optimal Doppler cooling to achieve a beam divergence below 100 μrad requires small detunings. To keep the number of absorbed and emitted photons low, the saturation parameter of the light field should be low, in the range of $2s_0=1$ to 2. Sub-Doppler cooling, however, works best in a different parameter range. Higher detunings of -2.0 to -4.0 at higher saturation parameters give optimal results. A beam divergence down to 25 μrad at a reasonable population of around 40% can then be achieved.

From an experimental point of view it would be convenient to have the same light field parameters for both Doppler and sub-Doppler cooling. Since these processes have optimal performance for different light field parameters, a compromise needs to be found. A reasonable solution would be to have a detuning of -1.5 at $2s_0 = 2$, resulting in a Doppler cooled beam of 120 μrad and a 25% sub-Doppler cooled population of 25 μrad . Table III gives the optimal light field parameters for (sub)-Doppler cooling and this compromise. Note that in this case linear polarized light is used for Doppler cooling as well, since this process is not significantly dependent on the polarization of the light.

All in all, however, sub-Doppler cooling does not appear to be able to significantly reduce the overall collimation of the beam. Combined with the disadvantage of the resulting distribution over the atomic substates, this option will not likely be pursued for the deposition experiment.

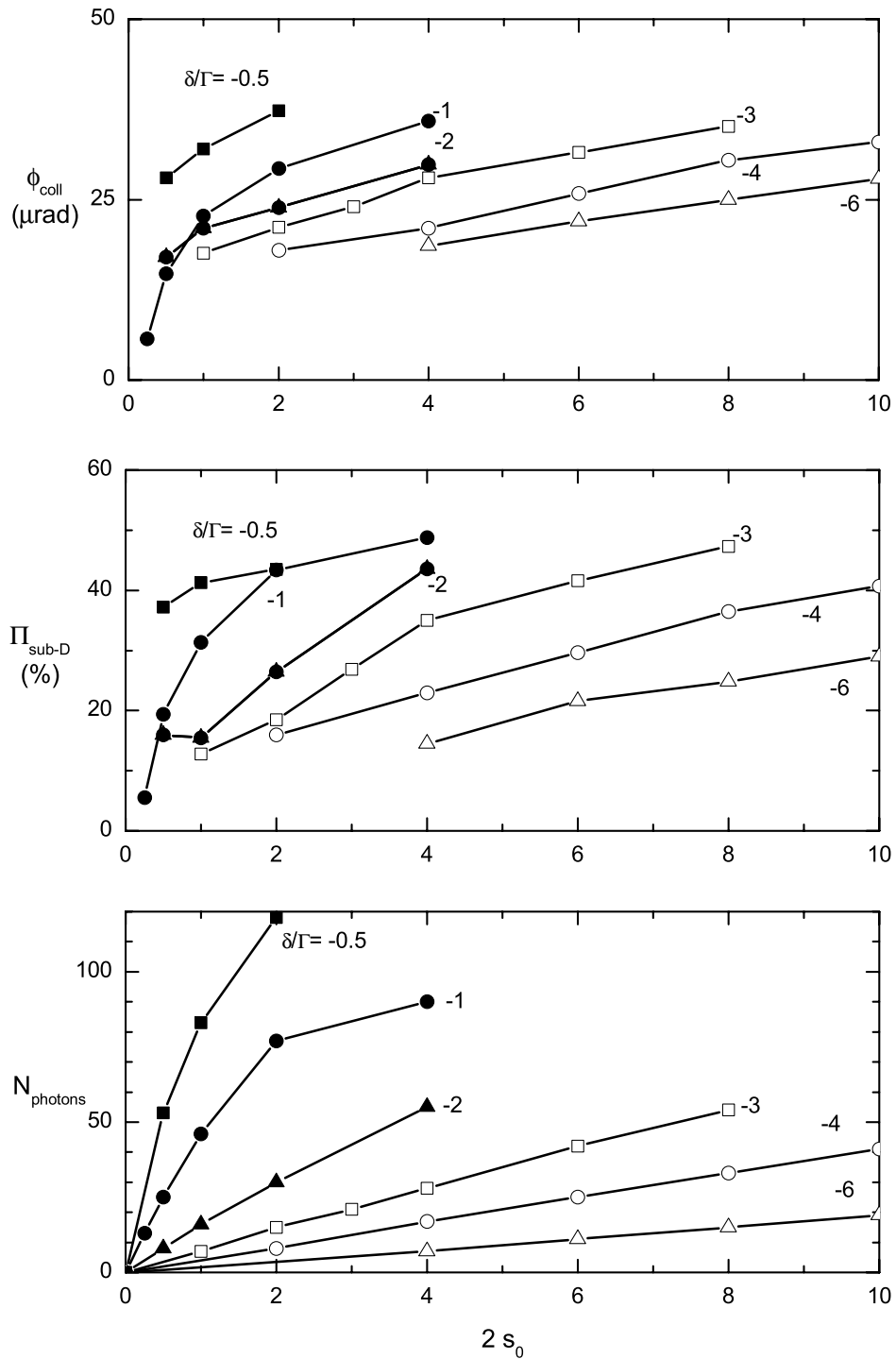


Figure 6.7: Results of Fe sub-Doppler cooling simulations. The three graphs show the Fe beam divergence (top), sub-Doppler cooled population (center) and average number of scattered photons (bottom). These quantities are calculated for various laser detunings and saturation parameters.

Table III: Results of Doppler and sub-Doppler laser cooling simulations for three different parameter sets, optimized for Doppler cooling, sub-Doppler cooling and for the combination.

	Doppler cooling	sub-Doppler cooling	combination
$2s_0$	1	6	2
δ/Γ	-1	-3	-1.5
φ_{coll} Doppler	85 μrad	200 μrad	120 μrad
φ_{coll} sub-Doppler	22 μrad	33 μrad	25 μrad
Π_{sub-D}	13%	47%	25%
$N_{photons}$	100	95	110

4 Measurements of laser cooling of Fe

4.1 Experimental setup

An experimental setup has been developed to investigate 1D laser cooling of the Fe beam. The setup is schematically shown in Fig. 6.8. It basically consists of two parts. The first part is the vacuum setup in which the supersonic Fe beam is generated. The second part is the UV laser system that is able to generate up to 300 mW of UV light at a wavelength of 372.0 nm and locked to the Fe resonance frequency.

Fe beam machine

The upper part of Fig. 6.8 shows the Fe beam machine. The vacuum setup consists of 4 stages, as denoted by encircled numbers in the figure. The supersonic Fe beam source which is described in detail in chapter 3 is mounted in the first stage. The large argon gas load is pumped by a 50 l/s roots pump (Edwards RD100) operating at a pressure of typically 10^{-1} mbar. An Fe beam is extracted by a skimmer into the next vacuum chamber (stage 2), in which the Fe beam is laser cooled. The laser beams have an area of $100 \times 5 \text{ mm}^2$, with a length of 100 mm in the beam direction. The laser beam enters and leaves the vacuum chamber through two-sided AR coated quartz windows (Eksma). The beam is reflected by a $100 \times 10 \text{ mm}^2$ HR-coated mirror (Eksma) mounted outside the vacuum. This mirror is not usable for sub-Doppler cooling, in which the reflected beam should have perpendicular linear polarization. In this case an additional $\lambda/4$ wave plate should be used.

The vacuum chamber of stage 2 is pumped with a 350 l/s Edwards EXTM350 turbo pump, resulting in an argon pressure in the range of 10^{-5} mbar. The deposition rate of the Fe beam can be measured by a McVac MCM-160 thickness monitor which is located 20 mm after the cooling region.

The vacuum chamber of stage 3 is also pumped with a 350 l/s Edwards EXTM350 turbo pump. Two movable slits of 200 μm width separated by 940 mm, are inserted to scan the Fe beam. This way the Fe beam collimation after laser cooling can be determined. A mechanical beam chopper rotating at a frequency of 100 Hz modulates the Fe and Ar beam signal. The chopping blade has two wide and two narrow slits. Two wide slits of 50 degree angle each transmit a quasi-continuous beam, whereas the two narrow slits of 1 mm width transmit a small burst to determine the beam velocity and speed ratio by a time-of-flight measurement (see Chapter

3).

The Fe and Ar beam signals can be measured by a quadrupole mass spectrometer. A small fraction of the Fe and Ar atoms (on the order of 10^{-7}) are first ionized by a Riber QM cross beam ionizer. The ions are extracted into the EAI Quad-200 quadrupole unit for mass selection. The 20 stage Cu-Be electron multiplier (Hamamatsu R595) gives an amplified pulse signal for each detected ion. A typical pulse height at 2.0 kV applied to the electron multiplier is 5 mV when the output is terminated with 50 Ω . An EG&G PAR 1182 pulse discriminator is used to convert the 5 mV pulses to TTL pulses, that are used for pulse counting with the computer system. A typical count rate for Fe and Ar beam signals would be on the order of 1 kHz and 1 MHz at beam intensities of $I_{Fe} = 10^{16}$ and $I_{Ar} = 10^{19} \text{ s}^{-1} \text{ sr}^{-1}$, respectively. Riber QMM-17 electronics are used for the ionizer, quadrupole unit and electron multiplier.

The mass spectrometer is located in a UHV vacuum chamber, pumped by two 20 l/s ion-getter pumps and a Ti-sublimation pump. Background pressures are in the range of $5 \cdot 10^{-10}$ to $2 \cdot 10^{-10}$ mbar.

UV laser system

In the lower half of Fig. 6.8 the UV laser system is shown. A detailed description is given in Chapter 4. A Coherent Innova 200 Ar ion pump laser with a maximum output of 20 W pumps a Coherent 899 Titanium Sapphire (Ti:S) ring laser. The maximum output of the Ti:S laser is 2 W at a wavelength of 744 nm, which is twice the UV wavelength of the Fe resonance transition for laser cooling and focusing.

The Ti:S beam enters the second harmonic generation (SHG) cavity in which frequency doubling of the 744 nm beam occurs. The resulting 372 nm beam leaves the cavity and is split in two. Most of the power is used for laser cooling, a relatively weak beam on the order of 10 to 20 mW is used for spectroscopy. Polarization spectroscopy is used to obtain a narrow Doppler-free feedback signal to correct the output wavelength of the Ti:S laser. The spectroscopy beam is sent through a hollow cathode discharge lamp (HCL), in which Fe atoms are sputtered off the cathode into the discharge.

A telescope (Lens Optics) is used to increase the initial UV laser beam size of 1 mm ($1/e^2$ beam radius) to a $100 \times 5 \text{ mm}^2$ beam suitable for laser cooling. The length of the laser cooling region is 100 mm along the Fe beam direction. The telescope consists of 3 curved mirrors, each HR coated for the used UV wavelength. The first two mirrors on which the beam is reflected are cylindrically curved. The first mirror expands the beam in the horizontal direction, the second mirror in the vertical direction. The last mirror is spherically curved to obtain a parallel beam of $100 \times 5 \text{ mm}^2$. A final HR coated mirror (Eksma) is used to reflect the beam 90° and to couple it into the vacuum chamber for laser cooling. The laser power required to obtain a $100 \times 5 \text{ mm}^2$ beam for laser cooling with a saturation parameter of $s_0 = 1$ is 31 mW.

4.2 First experiments on laser cooling of Fe

The setup that has been described in the previous section is in principle sufficient for performing laser cooling of an atomic Fe beam and to measure the resulting Fe beam collimation. The beam collimation can be determined using a combination of the mass spectrometer to measure the Fe beam intensity and the two movable slits. Fe beam profiles can be measured this way and the

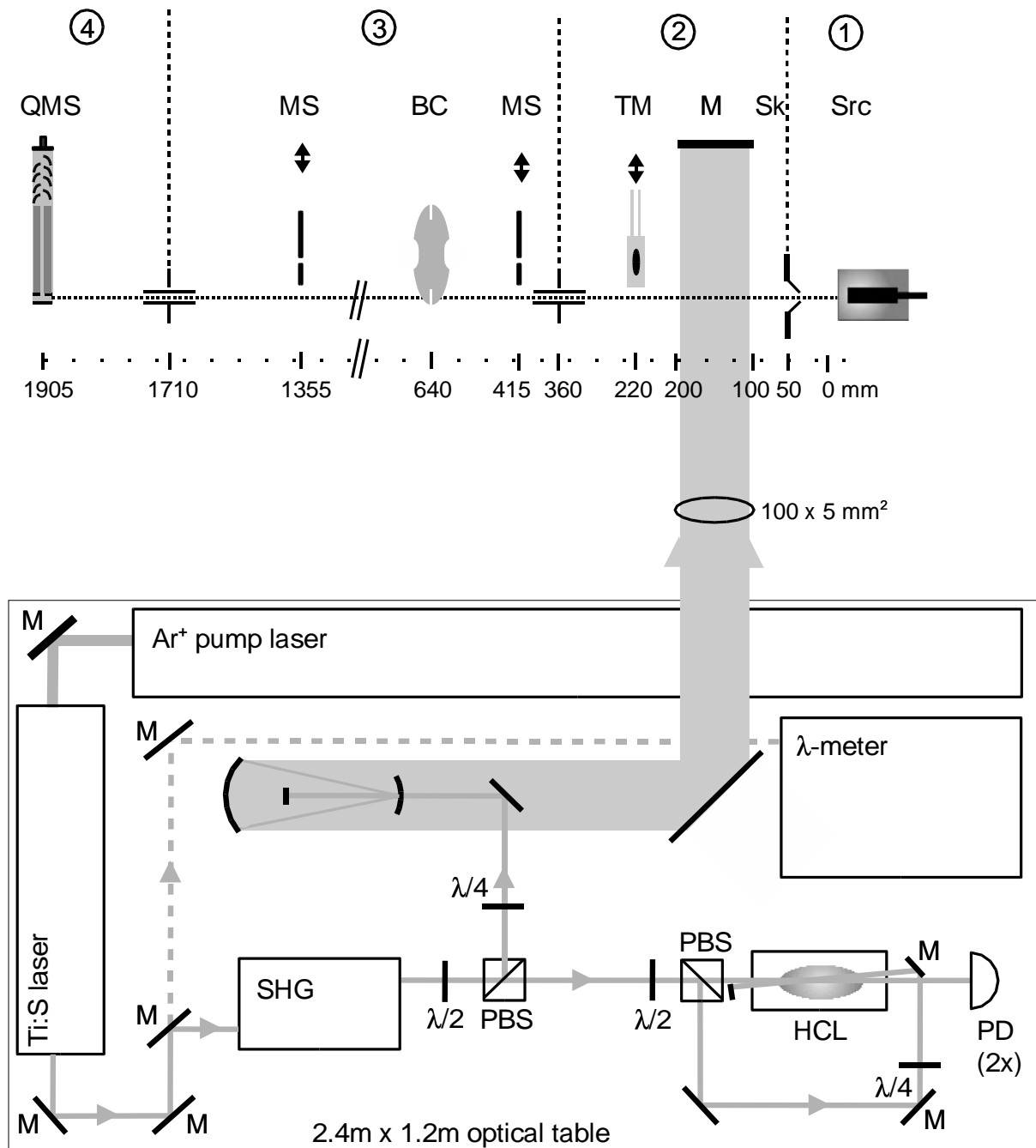


Figure 6.8: Experimental setup for laser cooling of Fe, consisting of the Fe beam machine and UV laser system. Src: supersonic Fe beam source, Sk: skimmer, M: mirror, TM: thickness monitor, MS: movable 200 μm slit, BC: beam chopper, QMS: quadrupole mass spectrometer. SHG: second harmonic generation, PBS: polarizing beam splitter cube, $\lambda/2$: half wave plate, $\lambda/4$: quarter wave plate, HCL: hollow cathode lamp, PD: photo diode.

resulting beam collimation follows from the width of the beam profile.

Much effort has been put into the development of the mass spectrometer and the UHV vacuum chamber in which this detector is located. The UHV chamber needs regular ‘cleaning’ by baking out at a temperature of 200 °C approximately once every year. Many problems associated with vacuum contamination, deterioration effects on the ionizer and electron multiplier of the detector, and detection efficiency have occurred. The effective time that the detector is fully operational has been relatively short during the three years of installation.

The mass spectrometer is a very important tool of the setup. This device will remain necessary as a permanent diagnostic tool for proper alignment of the Fe beam source, for aligning of the cooling lasers and probably for the alignment of the mechanical beam mask with the standing wave. For the latter application the sensitivity of the mass spectrometer needs to be boosted by one or preferably two orders of magnitude. This can be done by designing a new beam ionizer with an ionizing efficiency in the range of 10^{-5} , or by implementing an in-line mass spectrometer, that in general has a much higher detection efficiency. However, when such a tool is installed, optical alignment of the Fe beam line is not possible any more.

Preliminary attempts at laser cooling have already been made, however, without successful measurements. The attempts had to be cancelled because of a broken filament of the mass spectrometer ionizer. The filament has been replaced and the vacuum chamber has been baked at 200°C for two days in order to obtain a sufficient low pressure on the order of 10^{-10} Torr. The attempts are currently continued.

5 Future prospects

We are currently at the verge of having the first laser cooled atomic Fe beam. This work will from now on be carried out by two Ph.D. students. The team is completed with an undergraduate student, who is involved in the development of the final interaction chamber for laser focusing and deposition. The design of the substrate mount, which has to be very precise and stable in view of the small structure sizes and long deposition times, is critical. A vacuum of better than 10^{-9} Torr is required for clean deposition of Fe. Sample cleaning and gold passivation systems as well as a sophisticated sample transfer system, are also required. Implementation of the equipment is to be expected within a few months. In the meanwhile, Doppler cooling of the Fe beam is likely to be reached. From then, first attempts at laser focusing of the Doppler cooled Fe beam can be made.

6 Conclusions

Numerical simulations have been performed to investigate if a sufficiently small Fe beam divergence can be obtained with laser cooling. Using an interaction length of 10 cm, the Fe beam can be Doppler cooled to 85 μ rad. In this case the light field has a saturation parameter of $2s_0 = 1$ (corresponding to 15 mW of total laser power) with a detuning $\delta = -\Gamma$. The number of absorbed photons is 100, which means that 65% of the Fe atoms leave the cooling region in the ground state and can further be used for laser focusing. All atoms are pumped to the $m_J = \pm 4$ magnetic sublevel if circularly polarized light is used for Doppler cooling.

Sub-Doppler cooling of the Fe beam can also be performed by changing the polarization to a $\text{lin} \perp \text{lin}$ configuration. This way 47% of the Doppler cooled atoms can be cooled further, resulting in a beam divergence of $33 \mu\text{rad}$. In this case more power is required ($2s_0 = 6$) and a larger detuning ($\delta = -3\Gamma$). The remaining Doppler cooled atoms will have a significantly higher beam divergence of $200 \mu\text{rad}$. Again 65% of the atoms leave the cooling region in the ground state.

The best compromise using a single laser beam would be to use a light field with $2s_0 = 2$ and $\delta = -1.5\Gamma$. This results in beam divergence of $120 \mu\text{rad}$ attributed to Doppler cooling and $25 \mu\text{rad}$ due to sub-Doppler cooling, with a sub-Doppler cooled fraction of 25%. However, using any sub-Doppler cooling would result in the inability to pump the Fe atoms in a single magnetic sublevel. Given this disadvantage, it is highly questionable that the actual quality of the laser focused structures can be improved by adding sub-Doppler cooling.

Doppler cooling with circularly polarized light can be used to achieve a beam divergence of $100 \mu\text{rad}$ HWHM with a modest number of photons, suitable for our requirements.

Experimental results on laser cooling are to be expected soon, since the Fe beam setup and UV laser system are currently fully operational.

References

- [1] B. Brezger, Th. Schulze, U. Drodofsky, J. Stuhler, S. Nowak, T. Pfau, and J. Mlynek, *J. Vac. Sci. Technol.* **B15**, 2905 (1997)
- [2] P. Engels, S. Salewski, H. Levsen, K. Sengstock, and W. Ertmer, *Appl. Phys. B* **69**, 407 (1999)
- [3] G. Timp, R.E. Behringer, D.M. Tennant, and J.E. Cunningham, *Phys. Rev. Lett.* **69**, 1636 (1992)
- [4] F. Lison, H.J. Adams, P. Schuh, D. Haubrich, and D. Meschede, *Appl. Phys. B* **65**, 419 (1997)
- [5] J.J. McClelland, R.E. Scholten, E.C. Palm, and R.J. Celotta, *Science* **262**, 877 (1993)
- [6] M. Drewsen, U. Drodofsky, C. Weber, G. Schreiber, and J.Mlynek, *J. Phys. B* **29**, 843 (1996)
- [7] McGowan, R.W., D. Giltner, and Siu Au Lee, *Opt. Lett.* **20**, 2535 (1995)
- [8] M.D. Hoogerland, J.P.J. Driessen, E.J.D. Vredenburg, H.J.L. Megens, M.P. Schuwer, H.C.W. Beijerinck, and K.A.H van Leeuwen, *Appl. Phys. B* **62**, 323 (1996)
- [9] H.J. Metcalf and P. van der Straten, *Laser Cooling and Trapping*, Springer-Verlag New York, 1999
- [10] G. Nienhuis, P. van der Straten, and S-Q. Shang, *Phys. Rev. A* **44**, 462 (1991)
- [11] R. Blatt, W. Ertmer, P. Zoller, and J.L. Hall, *Phys. Rev. A* **34**, 3022 (1986)
- [12] B.R. Mollow, *Phys. Rev. A* **12**, 1919 (1975)
- [13] M.D. Hoogerland, H.F.P. de Bie, H.C.W. Beijerinck, K.A.H. van Leeuwen, P. van der Straten, E.J.D. Vredenburg, and H.J. Metcalf, *Phys. Rev. Lett.* **72**, 3332 (1994)
- [14] M.D. Hoogerland, *Laser manipulation of metastable neon atoms*, Ph.D. thesis, Eindhoven University of Technology (1993)

Summary

Lithography based on laser focusing of a beam of neutral iron atoms shows great promise for creating nanomagnetic structures. Laser focusing is a relatively new area, where successful experiments have been performed with, e.g., chromium atoms. Iron is perhaps one of the most difficult elements for this kind of experiment. Nevertheless, it is the ferromagnetic element most suitable for laser focusing.

The production of well isolated sub-10 nm structures of iron requires two improvements to conventional laser focusing: chromatic aberration is reduced by using a supersonic beam of Fe atoms, whereas spherical aberration is reduced by implementing an additional mechanical grating placed just upstream of the standing light wave.

In this thesis a description of the nanostructure project, preliminary results, and future plans are presented. The road to the fabrication of Fe nanostructures is full of challenges, and some of them have already been met.

One of the most pronounced results is the development of a supersonic Fe beam source. Since these kind of beam sources are commercially not available, considerable effort has been put into the development of such a tool. The resulting source, as shown in Chapter 3, has demonstrated excellent performance. An Fe beam intensity in the range of 10^{15} to 10^{16} atoms/s/sr can be produced, which gives an ultimate deposition rate of the Fe structures in the range of 10 nm/h. Furthermore, the axial beam temperature is exceptionally low for atomic metal beams. The beam speed ratio, defined as the ratio of the mean axial velocity to the velocity spread, has been measured to be 11 for the Fe beam. As a result, chromatic aberration of the standing light wave (nanolenses) that focus the atoms to nanostructures, which up till now has been one of the limiting factors for the size of the structures in similar experiments, will not play a significant role anymore.

Another result is the development of a UV laser system for laser manipulation of the atomic Fe beam, as described in Chapter 4. The requirements are a relatively high UV laser power of 500 mW at 372 nm, and a frequency stabilizing within $3 \cdot 10^{-9}$ and locked to the Fe resonance frequency. These requirements have been met. Using cavity-enhanced second harmonic generation of a laser beam of 2 W at 744 nm a power of more than 500 mW has been obtained at 372 nm. Polarization spectroscopy applied to a hollow Fe cathode discharge has been used to obtain an error signal with a width of 40 MHz. Using this signal to lock the laser, a frequency stabilizing of better than 1 MHz results on the fundamental frequency, or 2 MHz on the second harmonic beam at 372 nm.

In similar experiments performed so far the standing light wave is used as a thick lens. However, calculations presented in Chapter 5 show that using the standing wave in the thin lens regime, the focused structures are smaller by a factor of 3 at similar light field parameters. Channeling of atoms in a standing wave to produce small structures has also been investigated, since channeling is much more tolerant for errors in substrate placement and laser instability. However, this process requires a relatively high laser power of up to 1000 mW, which is not available. The resulting structure widths are then in the range of 10 to 30 nm, albeit with excellent contrast. Different models have been used for the calculations, and their validity has

been checked. As a result, a thorough understanding of the process of laser focusing has been achieved.

The next step that has to be taken experimentally, is laser cooling of the Fe beam. A well collimated beam of less than $200 \mu\text{rad}$ angular divergence is necessary in order to obtain sub-10 nm structures. Since the Fe beam is already “collimated axially” by using the supersonic Fe beam source, the transverse collimation is the main limiting factor to the focused Fe structure width. Numerical simulations presented in Chapter 6 have shown that a collimation of $100 \mu\text{rad}$ can be achieved using an acceptable number of scattered photons. We are now at the verge of having the first laser cooled atomic Fe beam. Experimental results on laser cooling are to be expected soon.

It is clear that several challenges are still present on the road to the fabrication of Fe nanostructures. However, the most important steps have already been taken, i.e., the development of a supersonic Fe beam source and UV laser system.

Samenvatting

Lithografie door middel van laserfocuseren van een atomaire ijzerbundel is een goede kandidaat voor de productie van nanomagnetische structuren. Laserfocuseren is een nieuwe techniek die volop in ontwikkeling is en die succesvol is toegepast met o.a. chroom atomen. IJzer is een van de moeilijkere elementen voor een soortgelijk experiment, maar is het enige ferromagnetische element dat geschikt is.

Om goed geïsoleerde ijzerstructuren te maken met een afmeting kleiner dan 10 nm, is het noodzakelijk om twee verbeteringen aan te brengen aan de conventionele manier van laserfocuseren. Chromatische aberraties worden geëlimineerd door een supersone ijzerbundel te gebruiken, terwijl sferische aberraties worden onderdrukt door een extra mechanisch masker in de ijzerbundel te plaatsen, vlak voor de staande lichtgolf.

Dit proefschrift omvat een beschrijving van het nanostructurenproject, alsmede de eerste resultaten die zijn geboekt en een vooruitblik naar het uiteindelijke doel. De eerste belangrijke uitdagingen op weg naar de productie van nanomagnetische structuren zijn reeds overwonnen.

Een van de belangrijkste behaalde resultaten is het vervaardigen van een bron die een supersone ijzerbundel genereert. Een dergelijke bron is commercieel niet verkrijgbaar, en dus is er veel energie gestoken in het ontwerp en de ontwikkeling hiervan. Het resultaat, zoals beschreven in hoofdstuk 3, is een bron die goed functioneert. Een ijzerbundel met een intensiteit in de orde van 10^{15} tot 10^{16} atomen/s/sr wordt gegenereerd, hetgeen neerkomt op een depositiesnelheid van de ijzerstructuren van 10 nm per uur. De axiale ijzerbundeltemperatuur is zeer laag: de verhouding van de gemiddelde bundelsnelheid tot de snelheidsspreiding is gemeten en is gelijk aan 11. Dit betekent dat chromatische aberraties niet meer zullen optreden in het uiteindelijke experiment. In soortgelijke experimenten hebben juist deze aberraties een limiet gevormd voor de structuurgrootte.

Het tweede belangrijke resultaat is beschreven in hoofdstuk 4. Het betreft de ontwikkeling van een UV lasersysteem, dat noodzakelijk is voor de manipulatie van de ijzerbundel. De eisen zijn een hoog laservermogen in het UV gebied: 500 mW bij een golflengte van 372 nm. De frequentiestabiliteit moet beter zijn dan $3 \cdot 10^{-9}$ en de laser moet zijn gekoppeld aan de resonantiefrequentie van de atomaire overgang van ijzer. Aan deze eisen wordt voldaan door UV licht te genereren via frequentieverdubbeling in een trilholte en door een holle ijzerkathode ontlading te gebruiken als referentie voor de atomaire overgang. Het errorsignaal dat wordt verkregen met behulp van polarisatie spectroscopie is 40 MHz breed. Dit is meer dan voldoende om de laser te stabiliseren binnen 1 MHz van de fundamentele frequentie en 2 MHz van de UV frequentie.

De staande lichtgolf die de atomen focuseert wordt in de meeste experimenten toegepast als een dikke lens. Berekeningen uit hoofdstuk 5 tonen aan dat de structuren een factor drie kleiner worden door de staande lichtgolf als dunne lens te gebruiken. Het is ook mogelijk de ijzeratomen te laten kanaliseren door de staande lichtgolf. Deze methode heeft praktische voordelen, omdat onnauwkeurigheden in de uitlijning van het substraat en instabiliteiten van de laser weinig effect hebben op dit proces. De nadelen zijn dat er 1000 mW aan UV vermogen nodig is en dat de kleinste structuurgrootte die kan worden bereikt tussen 10 en 30 nm ligt, echter met een uitstekend contrast. Verschillende fysische modellen zijn gebruikt voor deze

berekeningen en hun geldigheid is onderzocht. Uiteindelijk is er een goed inzicht verkregen in het laserfocuseringsproces.

De volgende experimentele stap is het transversaal laserkoelen van de ijzerbundel. Een goed gecollimeerde bundel met een divergentie van maximaal $200 \mu\text{rad}$ is noodzakelijk om structuren te fabriceren met een afmeting kleiner dan 10 nm . Aangezien de ijzerbundel reeds supersoon is, is de collimatie de uiteindelijk bepalende factor voor de structuurgrootte. Numerieke simulaties uit hoofdstuk 6 tonen aan dat een divergentie van $100 \mu\text{rad}$ kan worden behaald met een bescheiden aantal verstrooide fotonen.

We staan nu op het punt de eerste lasergekoelde ijzerbundel te realiseren. Experimentele resultaten kunnen op korte termijn worden verwacht.

Het is duidelijk dat er nog enkele uitdagingen liggen op weg naar de fabricatie van de nanostructuren. De belangrijkste stappen zijn echter al gezet, namelijk de realisatie van de supersone ijzerbundel en het UV lasersysteem.

Dankwoord

Hier wil ik enkele mensen in het bijzonder bedanken voor hun bijdrage aan het tot stand komen van mijn proefschrift en voor de plezierige tijd die ik met hen heb gehad. Mijn promotoren Ton van Leeuwen en Herman Beijerinck ben ik veel dank verschuldigd voor hun inzet en enthousiasme voor mijn promotie. Ik heb kunnen profiteren van de enorme kennis van Ton en van de heldere visie van Herman, vooral op momenten dat bepaalde problemen onoplosbaar leken. Ook heb ik genoten van de samenwerking met Peter van der Straten gedurende het laatste jaar. Het feit dat hij vaak in het lab was te vinden maakt hem in mijn ogen tot de ideale begeleider.

Onze technische staf, Louis van Moll, Jolanda van de Ven en Rien de Koning (van de Barbecue) wil ik bedanken voor de talloze keren dat ze de opstelling hebben verbeterd. Ik heb veel geleerd van Louis' markante adviezen ("vast=dol en een kwartslag terug" is er één van) en technisch inzicht. Het vervaardigen van de ijzerbron is een knap staaltje van ambacht op hoog technisch niveau. Voor dat laatste ben ik ook de keramiekafdeling veel dank verschuldigd, alsmede de werkplaats, waar ze inmiddels goed weten hoe een verstopte nozzle of skimmer er uit ziet.

Ik kon altijd aankloppen bij mijn collega's Edgar Vredenburg en Simon Kuppens en heb geprofiteerd van hun rijke wetenschappelijke ervaring. Vele malen hebben ze meegewerkt aan het oplossen van complexe problemen, waarvoor ik hun zeer dankbaar ben.

Het was een genoegen om het laatste anderhalf jaar in het lab samen te werken met mijn collega's Bart Smeets en Edwin te Slighte. Bart, bedankt voor het prachtige werk dat je hebt verricht aan het lasersysteem. Je moet wel weer op kamers gaan, vind ik. Edwin, goed dat je die arbeidstijdverkortung op donderdagmiddag hebt ingevoerd! Ook de studenten Richard v.d. Stam, Harm Wieldraaijer en Ron Bessems ben ik veel dank verschuldigd voor hun bijdrage aan het onderzoek.

Het zal moeilijk worden afscheid te nemen van alle collega's in de groep. Ik heb een leuke tijd gehad met Veronique Mogendorff (welke nevenactiviteit heb je niet gedaan?), Eric van Kempen, Alquin Stevens, Kenian Domen, Maarten Jansen, Bert Claessens en Wilbert Mestrom. Bedankt voor het reanimeren van mijn PC, Wilbert, twee weken voor de deadline van de drukker...

Onze secretaresses Rina Boom en Marianne van den Elshout wil ik hartelijk bedanken voor hun hulp bij alle administratieve klusjes.

Ook in de eerste jaren van mijn promotie heb ik hartelijk kunnen lachen met mijn oud-collega's. Ik mis het AOI-overleg met de Dikke, de Kale, de Dunne en Esther (Roel Knops, Armand Koolen, Sjef Tempelaars en Patrick Sebel), waarin we hebben gefilosofeerd over nutteloze zaken tot in de diepe uren. Met Roel kon je zonder probleem anderhalve fles whiskey en twee liter wijn nuttigen na een Thaise maaltijd. Ook het in elkaar zetten van de beroemde promotiefilms zal ik nooit vergeten.

Naast bovengenoemde mensen ben ik ook veel dank verschuldigd aan vrienden en familie. Ik heb me altijd thuis gevoeld bij genootschap Nwyvre, een bonte verzameling van fysici die het blond-schuimend bier niet schuwen. Igor wil ik speciaal bedanken voor alle steun die ik van hem heb gekregen, ook in de moeilijke tijden, en Cathy voor de lol die we hebben tijdens onze Salsa-pogingen.

Schoolstraat 13 is een begrip geworden in mijn sociale leven. De swingende party's, de voetbalwedstrijden op TV vanaf de bank of tribune, en ook de knipbeurten staan voor altijd in mijn geheugen gegrift. DJ-Pils en Louis, ik kan jullie niet genoeg bedanken voor jullie vriendschap en voor het feit dat jullie het bovengenoemde allemaal mogelijk hebben gemaakt.

De jaarlijkse skivakantie in januari is altijd een periode geweest waar ik heerlijk naar toe heb kunnen leven en waarna ik weer gemotiveerd aan de slag kon. Ik wil alle Skiberen hartelijk bedanken voor de leuke sportieve weken en voor de gezelligheid, ook wanneer de liften gesloten waren.

Mijn squashmaatjes ben ik veel dank verschuldigd voor de plezierige tijden op de squashbanen. De maandag- en woensdagavond heb ik altijd vrijgehouden om heerlijk tegen een balletje aan te meppen, vooral tijdens trainingen van Sjef "de stoel" van der Heijden. Ray, bedankt voor de leuke weddenschappen die we op de baan hebben uitgevochten!

Astrid ("het wordt weer eens tijd om naar de film te gaan") van den Hoek wil ik speciaal bedanken voor het ontwerpen van de mooie kافت van dit proefschrift en bovendien voor de gezellige Plaza-avonden.

Tenslotte wil ik de mensen die zeer dicht bij me staan, mijn ouders en mijn lieve zus Yvonne, bedanken voor hun onvoorwaardelijke liefde en steun. Het laatste plekje is gereserveerd voor Arina, mijn dappere vriendin, die me heeft laten zien wat geluk is in het leven....

Curriculum Vitae

- 30 oktober 1972 Geboren te Baarlo
- 1985-1991 Gymnasium β ,
St. Thomas College te Venlo
- 1991-1997 Studie Technische Natuurkunde,
Technische Universiteit Eindhoven,
doctoraal examen juni 1997
- 1997-2002 Onderzoeker-In-Opleiding bij Stichting FOM,
werkgroep AQ-E-a,
Experimentele Atoomfysica en Quantumelektronica,
Faculteit Technische Natuurkunde,
Technische Universiteit Eindhoven